# DAMAGES IN TRANSPARENT MATERIALS BY ULTRASHORT LASER PULSE

by

Weibo Cheng

Copyright © Weibo Cheng 2021

A Dissertation Submitted to the Faculty of the

JAMES C. WYANT COLLEGE OF OPTICAL SCIENCES

In Partial Fulfillment of the Requirements

For the Degree of

DOCTOR OF PHILOSOPHY

In the Graduate College

THE UNIVERSITY OF ARIZONA

2021

THE UNIVERSITY OF ARIZONA
GRADUATE COLLEGE

As members of the Dissertation Committee, we certify that we have read the dissertation prepared by **Weibo Cheng**, titled ***Damages in Transparent Materials by Ultrashort Laser Pulse*** and recommend that it be accepted as fulfilling the dissertation requirement for the Degree of Doctor of Philosophy.

Rongguang Liang — Date: 05/13/2021
*Professor Rongguang Liang*

Date: 5/13/21
*Professor Robert A. Norwood*

Shibin Jiang — Date: May 13, 2021
*Professor Shibin Jiang*

Final approval and acceptance of this dissertation is contingent upon the candidate's submission of the final copies of the dissertation to the Graduate College.

I hereby certify that I have read this dissertation prepared under my direction and recommend that it be accepted as fulfilling the dissertation requirement.

Rongguang Liang — Date: 05/13/2021
*Professor Rongguang Liang*
Dissertation Committee Chair
*Wyant College of Optical Sciences*

# ACKNOWLEDGEMENTS

I would like to express my gratitude to my committee chair Dr. Rongguang Liang for providing guidance and strong support. I would like to thank Dr. Robert Norwood for his guidance not only in course work but also in many aspects of my PhD journey. My gratitude extends to Dr. Shibin Jiang for his invaluable advice.

I gained practical skills and knowledge working in Dr. Pavel Polynkin's lab for that I am extremely grateful. The weekly seminar in Dr. Jerome Moloney's forum helped me gained insight into cutting edge research and gave me exposure to the beauty of mathematics.

Working in the lab is one of the most important parts of graduate student life. I would like to thank Dr. Maik Sheller, Dr. Ali Azarm, Dr. Norman Born, and Dr. Ariunbold Gombojav for all the discussions and chats as my lab mate. I spend a good amount of time in Dr. Tom Milster's lab operating the SEM machine looking at tiny features. Thank you Dr. Milster for your support and thank you Victor Densmore III, Lee Johnson for all the help.

The college of optical sciences has designed great courses that built my optics foundation. I would like to express my gratitude to Dr. Masud Mansuripur for his extremely insightful introduction to electromagnetic waves and Dr. Scott Tyo for his enthusiastic and fun course on linear systems. I truly enjoyed it.

I want to express my thanks to Dr. John Koshel and Dr. Brian Anderson for extremely helpful advice and strong support for navigating me through some of the most challenging times. I also want to thank the wonderful academic program staff Ruth Corcoran, Jini Kandyil, and Mark Rodriguez for all the help.

OSC is truly an amazing place where I met countless friends whom I establish long term friendship with. I would like to express my thanks to Caleb Baker, Paris Panagiotopoulos for making my Friday movie night so much fun. Life without friends is boring and it is especially true for a PhD student. I am really grateful for meeting and getting to know so many friends, Dima Reshidko, Raj Katham, Trent Mankowski, Jeff Brown, Alex Laurain, Chris Moller, Andrey Alenin, Guillaume Butel, Dmitriy Churin, Shaun Pacheco, Ashley Valdez, Dulce Maria, Craig Ament, Greg Cohoon, Vicky Chan, Zhongkun Xiang, Yilong Zhen, Yuhao Wang, Xuefei Wu, Ming Zhao, Han Zhang, Xinda Hu, Yi Qin, Huang Run, Hekun Huang, Weichuan Gao, Jilin Yang etc.. thank you guys! I can't imagine how I would have survived without you.

This magic place brought me not only friends but also my best friend who would become my wife later and my daughter's mother now. Thank you Aria for sticking with me, you won't regret it.

Last but not the least, I want to thank my family and friends in China for all the help, support, and understanding throughout the years. My parents, Yunlin Wu and Siqing Cheng, encouraged me to pursue my dream and gave me the freedom to

choose my path, thank you so much and I love you guys.

# DEDICATION

*Dedicated to my mom and dad.*

# TABLE OF CONTENTS

LIST OF FIGURES . . . . . . . . . 9

ABSTRACT . . . . . . . . . 14

CHAPTER 1 Introduction . . . . . . . . . 16

CHAPTER 2 Generation of ultrashort pulses . . . . . . . . . 21
2.1 Picosecond pulse generation . . . . . . . . . 21
2.2 Femtosecond pulse generation . . . . . . . . . 23

CHAPTER 3 Ultrashort pulse phenomenon in transparent materials . . . . . 26
3.1 Diffraction . . . . . . . . . 27
3.2 Dispersion . . . . . . . . . 28
3.3 Self focusing . . . . . . . . . 28
3.4 Self phase modulation . . . . . . . . . 30
3.5 Photon ionization . . . . . . . . . 30
3.6 Avalanche ionization . . . . . . . . . 34
3.7 Plasma generation . . . . . . . . . 34
3.8 Plasma absorption and defocusing . . . . . . . . . 34
3.9 Conclusions . . . . . . . . . 35

CHAPTER 4 Bulk modification by ultrashort pulse . . . . . . . . . 36
4.1 Borosilicate glass . . . . . . . . . 38
4.2 Fused silica . . . . . . . . . 40
4.3 Sapphire . . . . . . . . . 41
4.4 Conclusions . . . . . . . . . 43

CHAPTER 5 Model of ultrashort pulse propagation and electron dynamics . 45
5.1 Model pulse propagation . . . . . . . . . 45
5.2 Model electron generation . . . . . . . . . 50
5.3 Extended Crank-Nicolson scheme . . . . . . . . . 51
5.4 Implementing Crank-Nicolson scheme . . . . . . . . . 52

CHAPTER 6 Simulation results of ultrashort pulse propagation . . . . . . . 57
6.1 Borosilicate glass . . . . . . . . . 57
6.1.1 Pulse behavior . . . . . . . . . 59
6.1.2 Electron dynamics . . . . . . . . . 68

TABLE OF CONTENTS – *Continued*

6.1.3 Matching modification track with electron contour . . . . . . . 73
6.1.4 Role of MPI and avalanche ionization . . . . . . . . . . . . . . 76
6.2 Fused silica . . . . . . . . . . . . . . . . . . . . . . . . . . . . 77
6.2.1 Pulse behavior . . . . . . . . . . . . . . . . . . . . . . . . . . 78
6.2.2 Electron dynamics . . . . . . . . . . . . . . . . . . . . . . . . 84
6.2.3 Matching modification track with electron contour . . . . . . . 88
6.2.4 Role of MPI and avalanche ionization . . . . . . . . . . . . . . 90
6.3 Fused silica interacting with femtosecond pulse . . . . . . . . . . . . . 91
6.3.1 Pulse behavior . . . . . . . . . . . . . . . . . . . . . . . . . . 92
6.3.2 Electron dynamics . . . . . . . . . . . . . . . . . . . . . . . . 96
6.3.3 Role of MPI and avalanche ionization . . . . . . . . . . . . . . 98
6.4 Conclusions . . . . . . . . . . . . . . . . . . . . . . . . . . . . 100

CHAPTER 7 Applications of ultrashort lasers . . . . . . . . . . . . . . . . . . 101
7.1 Laser welding . . . . . . . . . . . . . . . . . . . . . . . . . . . 101
7.2 Waveguide writting . . . . . . . . . . . . . . . . . . . . . . . . 103
7.3 Glass cutting . . . . . . . . . . . . . . . . . . . . . . . . . . . 103

CHAPTER 8 Conclusions and outlook . . . . . . . . . . . . . . . . . . . . . . 105

APPENDIX A Pulse propagation code . . . . . . . . . . . . . . . . . . . . . 108

APPENDIX B Pulse intensity lookup table . . . . . . . . . . . . . . . . . . . 131

REFERENCES . . . . . . . . . . . . . . . . . . . . . . . . . . . . . . . . 132

# LIST OF FIGURES

1.1 High level timescale of events during ultrashort pulse laser material interaction. . . . . . . . . . . . . . . . . . . . . . . . . . . . . 17

2.1 Schematic of a chirped pulse amplification laser system. . . . . . . . . 24

3.1 Self focusing of a beam by Kerr lens effect. . . . . . . . . . . . . . . . 29

3.2 Schematic diagram of tunneling and multiphoton ionization. . . . . . 31

3.3 Photo ionization rate as a function of laser intensity. . . . . . . . . . 33

4.1 Schematic of the experimental setup. . . . . . . . . . . . . . . . . . . . 37

4.2 Modification created inside borosilicate glass. . . . . . . . . . . . . . . 39

4.3 Modification created inside fused silica glass. . . . . . . . . . . . . . . 41

4.4 Modification created inside sapphire. . . . . . . . . . . . . . . . . . . . 43

6.1 The evolution of pulse intensity profile at different propagation distance z in borosilicate glass with input pulse energy $E_{in} = 1\,\mu J$ . . . . 58

6.2 The spatial distribution of intensity along propagation axis z in borosilicate glass with pulse energy of $E_{in} = 1\,\mu J$. . . . . . . . . . . . 59

6.3 The on axis temporal distribution of intensity along propagation axis z in borosilicate glass with pulse energy of $E_{in} = 1\,\mu J$ . . . . . . . . . 60

6.4 The evolution of pulse intensity profile at different propagation distance z in borosilicate glass with input pulse energy $E_{in} = 3\,\mu J$. . . . 62

6.5 The spatial distribution of intensity along propagation axis z in borosilicate glass with pulse energy of $E_{in} = 3\,\mu J$ . . . . . . . . . . . 63

6.6 The on axis temporal distribution of intensity along propagation axis z in borosilicate glass with pulse energy of $E_{in} = 3\,\mu J$ . . . . . . . . . 64

6.7 The evolution of pulse intensity profile at different propagation distance z in borosilicate glass with input pulse energy $E_{in} = 5\,\mu J$. . . . 65

6.8 The spatial distribution of intensity along propagation axis z in borosilicate glass with pulse energy of $E_{in} = 5\,\mu J$ . . . . . . . . . . . 66

6.9 The on axis temporal distribution of intensity along propagation axis z in borosilicate glass with pulse energy of $E_{in} = 5\,\mu J$ . . . . . . . . . 67

6.10 The evolution of electron density at different propagation distance z in borosilicate glass with input pulse energy $E_{in} = 1\,\mu J$. . . . . . . . . 68

6.11 The on axis evolution of electron density at different propagation distance z in borosilicate glass with pulse energy $E_{in} = 1\,\mu J$. . . . . . 69

6.12 The evolution of electron density at different propagation distance z in borosilicate glass with input pulse energy $E_{in} = 3\,\mu J$ . . . . . . . . 70

6.13 The on axis evolution of electron density at different propagation distance z in borosilicate glass with input pulse energy $E_{in} = 3\,\mu J$ . . 71

6.14 The evolution of electron density at different propagation distance z in borosilicate glass with input pulse energy $E_{in} = 5\,\mu J$ . . . . . . . . 72

6.15 The on axis evolution of electron density at different propagation distance z in borosilicate glass with input pulse energy $E_{in} = 5\,\mu J$ . . 73

6.16 Simulation results of beam propagation and electron density in borosilicate glass. . . . . . . . . . . . . . . . . . . . . . . . . . . . 75

6.17 The role of MPI and avalanche ionization in borosilicate glass. . . . . 76

6.18 The evolution of pulse intensity profile at different propagation distance z in fused silica with input pulse energy $E_{in} = 1.5\,\mu J$. . . . . . . 78

6.19 The spatial distribution of intensity along propagation axis z in fused silica with pulse energy of $E_{in} = 1.5\,\mu J$. . . . . . . . . . . . . . . . . . . 79

6.20 The on axis temporal distribution of intensity along propagation axis z in fused silica with pulse energy of $E_{in} = 1.5\,\mu J$. . . . . . . . . . . . 80

6.21 The evolution of pulse intensity profile at different propagation distance z in fused silica with input pulse energy $E_{in} = 3\,\mu J$. . . . . . . . 81

6.22 The spatial distribution of intensity along propagation axis z in fused silica with pulse energy of $E_{in} = 3\,\mu J$. . . . . . . . . . . . . . . . . . . . 82

6.23 The on axis temporal distribution of intensity along propagation axis z in fused silica with pulse energy of $E_{in} = 3\,\mu J$. . . . . . . . . . . . . 83

6.24 The evolution of electron density at different propagation distance z in fused silica with input pulse energy $E_{in} = 1.5\,\mu J$. . . . . . . . . . . 84

6.25 The on axis evolution of electron density at different propagation distance z in fused silica with input pulse energy $E_{in} = 1.5\,\mu J$. . . . . 85

6.26 The evolution of electron density at different propagation distance z in fused silica with input pulse energy $E_{in} = 3\,\mu J$. . . . . . . . . . . . 86

6.27 The on axis evolution of electron density at different propagation distance z in fused silica with input pulse energy $E_{in} = 3\,\mu J$. . . . . . 87

6.28 Simulation results of beam propagation and electron density in fused silica. . . . . . . . . . . . . . . . . . . . . . . . . . . . . . . . . . . . . 89

6.29 The role of MPI and avalanche ionization in fused silica. . . . . . . . 91

6.30 The evolution of pulse intensity profile at different propagation distance z in fused silica with input pulse energy $E_{in} = 1\,\mu J$ and pulse duration 500 fs. . . . . . . . . . . . . . . . . . . . . . . . . . . . . 93

6.31 The spatial distribution of intensity along propagation axis z in fused silica with pulse energy of $E_{in} = 1\,\mu J$ and pulse duration 500 fs. . . . 94

6.32 The on axis temporal distribution of intensity along propagation axis z in fused silica with pulse energy of $E_{in} = 1\,\mu J$ and pulse duration 500 fs. . . . . . . . . . . . . . . . . . . . . . . . . . . . . . . . . 95
6.33 The evolution of electron density at different propagation distance z in fused silica with input pulse energy $E_{in} = 1\,\mu J$ and pulse duration 500 fs. . . . . . . . . . . . . . . . . . . . . . . . . . . . . . . . . 96
6.34 The on axis evolution of electron density at different propagation distance z in fused silica with input pulse energy $E_{in} = 1\,\mu J$ and pulse duration 500 fs. . . . . . . . . . . . . . . . . . . . . . . . . . 97
6.35 The role of MPI and avalanche ionization in fused silica under femtosecond pulse irradiation. . . . . . . . . . . . . . . . . . . . . . . . . 99

# ABSTRACT

Ultrashort lasers that generate laser pulses down to picosecond and femtosecond range have advanced over the past decade from delicate lab systems to robust industry machines. The availability of stable ultrashort laser systems opens up a wide range of exciting applications from transparent material processing such as waveguide fabrication to bio applications such as cell ablation. The fundamental aspects of ultrashort pulse material interaction are still remaining an active research topic. Here, we focus on the investigation of how ultrashort pulses, particularly picosecond laser pulses, interact with the bulk of transparent materials such as borosilicate glass, fused silica and sapphire. We investigate damage inside the bulk of borosilicate glass, fused silica, and sapphire by a single shot of IR picosecond laser pulse experimentally. In our experiments, extended bulk damage tracks with an aspect ratio of about 1:10 are generated. The damage morphology in each of the material is found to be different. We also numerically model pulse propagation and electron dynamics in borosilicate glass and fused silica in both picosecond and femtosecond regimes. The shape and size of the damage sites are shown to correspond to an electron cloud with density of about $10^{20}\,\mathrm{cm}^{-3}$. The underlying mechanism of electron generation by multiphoton ionization and avalanche ionization is numerically

investigated. The multiphoton ionization rate and avalanche ionization rate are determined by fitting experimental results. The relative role of multiphoton ionization and avalanche ionization are numerically studied and the percentage of electron contribution from each ionization channels are investigated.

# CHAPTER 1

## Introduction

Laser, the short name for light amplification by stimulated emission of radiation, was invented in the 1960s. Right after laser's invention, people started using it for material modifications. Further developments of laser systems generated more powerful lasers with high quality beam that made controllable material processing possible. And laser started becoming a unique versatile tool that could process materials in a contactless fashion.

In the 1990s, two inventions of mode locking mechanisms completely revolutionized the laser industry: semiconductor saturable absorber mirrors mode locking[1] and Kerr lens mode locking[2]. These two new mode locking mechanisms make stable ultrashort picosecond and femtosecond pulses possible. With the broad gain bandwidth of Ti:sapphire crystal, pulses of a few optical cycles are generated[3]. Together with chirped pulse amplification[4], ultrashort pulses with intensity of more than $10^{13}$ W/cm$^2$ are commercially available. These inventions opened up new chapters of light-matter interactions that are not possible before.

Ultrafast lasers are ubiquitous in a wide range of applications in modern industry. Here we focus on the fundamental mechanisms of ultrashort pulse interaction

with transparent materials such as glass and its applications to micro-welding[5], waveguide writing[6, 7], and glass cutting[8].

The mechanisms of bulk material modification by ultrashort laser pulses are still an active research topic[9, 10, 11, 12, 13, 14, 15]. The general physical picture of internal transparent material modification can be described as the following processes. When a high intensity laser pulse focuses inside a bulk material, electrons are excited from valence band to conduction band through multiphoton ionization and subsequent avalanche ionization at the focal volume. The excited electrons form a plasma cloud and absorb part of the pulse energy, which eventually transfers to the lattice through electron phonon interaction and heat up the bulk of the material. A general timescales of the event is shown in Figure 1.1

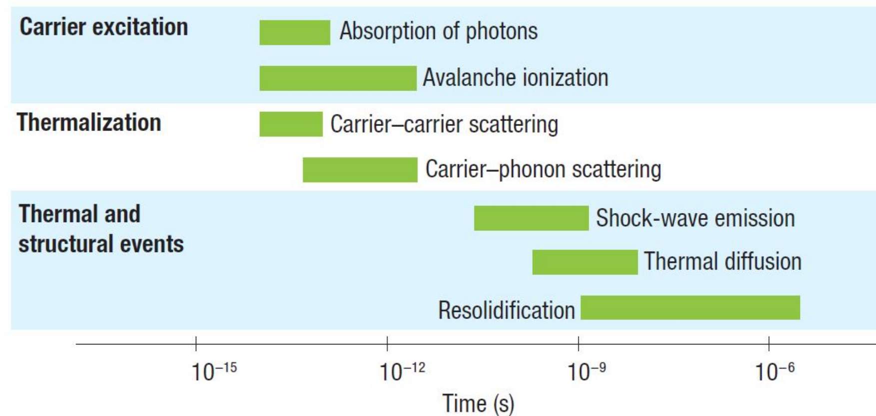


Figure 1.1: High level timescale of events during ultrashort pulse laser material interaction. Reprinted with permission from reference[16].

The laser pulse duration plays a big role in material modification. Intense pulses

excite electrons from valence band to conduction band, the excited electrons distribute energies among themselves via carrier-carrier scattering and this process typically happens on a time scale of 10 - 100 fs or so. The energy absorbed by the electrons transfer to lattice via a slower process called carrier-phonon scattering that happens on a time scale of 10 ps or so.

For pulse durations that are longer than the carrier-phonon scattering time, a good amount of energy is transferred to the lattice during the laser pulse and the excited lattice phonons transfer energy further to the surroundings of the focal volume via thermal diffusion. If the temperature in the affected zone becomes high enough, material will melt, or even crack due to high tension gradient, and leave a permanent damage mark. Damage threshold of this thermal driven long pulse ablation follows a square root of the pulse duration rule[17].

However, for pulse duration of 10 ps or less, the damage mechanism is different and the square root rule is violated[17]. In this regime, the energy deposition and energy relaxation via carrier-phonon interaction is decoupled, thus the thermal impact to the adjacent area is minimized result an minimum heat affected zone with much less collateral damages[18]. This gives ultrashort pulses the unique advantage of generating more precise features with less heat impact to the material.

When the material is exposed to multiple pulses with pulse to pulse interval less than the thermal diffusion time of the material, the heat will accumulate at the

focal region and the temperature at the focal region will increase to a few thousands degrees [19, 20]. The internal modification of glass by multiple ultrashort laser pulses with high repetition rate has been demonstrated experimentally[21, 22, 23, 24, 25, 26] and the shape of the modified structure has been studied numerically[22, 11]. However, the fundamental picture of how electrons are generated during the very first pulse of the entire pulse train that leads to material modification is still not very clear. The initial electrons are crucial to the plasma generation and energy relaxation not only within the first pulse but also to the subsequent pulses in a multiple pulse scenario.

We specifically aim to understand laser modification in the bulk of transparent materials such as borosilicate glass, fused silica and sapphire by using a single shot of ultrashort laser pulse to probe the initial picture. The material used in our study is of strategic importance and it is widely used in modern industry. The pulse duration we choose in our experimental study is a widely available picosecond pulse with duration of 10 ps. Later, we expand the investigation from 10 ps down to 500 fs in our numerical investigation.

In chapter 2, we briefly mention the key enablers in generating ultrashort pulses of practical use.

In chapter 3, we discuss the typical phenomenon of propagating ultrashort pulses in transparent materials including diffraction, dispersion, self focusing, self phase

modulation, photon ionization, avalanche ionization, plasma defocusing, and plasma absorption.

In chapter 4, we present experimental results of bulk material modification in borosilicate glass, fused silica, and sapphire. Laser modification tracks with high aspect ratio are generated by a single shot of picosecond laser pulse. We found the characteristics of the laser-modified region are vastly different for the materials we investigated.

In chapter 5, we present a model for pulse propagation and electron generation in transparent materials. We also present an algorithm to implement the model in Matlab.

In chapter 6, we present simulation results of pulse propagation and electron generation in borosilicate glass, and fused silica. We also expand our model to femtosecond pulse durations and compare pulse propagation and electron behaviors.

In chapter 7, we discuss ultrashort pulse applications in laser welding, waveguide writing and glass cutting.

In chapter 8, we conclude the thesis and provide outlook for future research.

# CHAPTER 2

# Generation of ultrashort pulses

In 1960, the first laser was demonstrated by Theodore Maiman[27, 28, 29], which marked a new age of light generation. Unprecedented applications have been enabled ever since.

It is very hard to cover all the details of the remarkable history of laser developments in this thesis. However, two inventions in generating ultrashort laser pulses deserve our attentions here. One is the invention of passive mode locking by SEmiconductor Saturable Absorber Mirror(SESAM)[30], which pushed the pulse width down to picosecond range. The other is the discovery of Kerr lens mode locking, which further pushed down the pulse width to femtosecond range[31, 32].

## 2.1 Picosecond pulse generation

Mode locking is the technique of inducing a fixed phase relation between the longitudinal modes of the laser cavity. The in-phase longitudinal modes constructively interfere with each other and generate a train of short pulses. There are two types of mode locking schemes: active mode locking and passive mode locking.

In active mode locking, there is typically an electro-optical modulator involved to modulate the intracavity loss. The pulse duration is limited by the modulating signal. In passive mode locking, there is no external signal used. Instead, the pulse itself triggers the intracavity loss and gain modulation. Thus, much shorter pulse duration can be generated[30].

SESAMs are a breakthrough mechanism for passive mode locking material that open up stable picosecond or even shorter pulse generation with long term stability. SESAMs have the properties of low loss at high pulse intensity and high loss at low intensity, which enables passive mode locking. There are a few key parameters that govern how short of a pulse a SESAM can support, including its wavelength range of absorption, its dynamic response time of recovery, and its saturation intensity.

With the SESAM mode locked seed generator and a master oscillator power amplifier, the output pulse energy can reach a few hundred µJ with pulse duration of $< 10\,\mathrm{ps}$, repetition rate up to MHz while maintaining good beam quality with $M^2 < 1.3$[33]. The high pulse energy is extremely important to enable practical industrial applications such as cutting, drilling and welding in a cost effective way.

A typical scheme of generating high power picosecond laser pulse can be found in reference[34]. The low energy pulse coming out of the seed oscillator goes through 4 stages of amplification and reach a few hundred µJ pulse energy at the output[34].

## 2.2 Femtosecond pulse generation

To further reduce the pulse width, faster passive mode locking mechanisms that can support larger bandwidth need to be introduced. In 1990, two groups accidentally generated 190 fs and 60 fs laser pulses from a Ti:sapphire laser that either had a slow dye saturalble absorber with slow recovery time which would not support femtosecond pulse or had no visible saturable absorber at all[31, 2]. The mode locking mechanism was soon explained by Kerr lens effect. Kerr lens mode locking is obtained via a Kerr lens in intracavity material where refractive index depends on pulse intensity $\delta n = n_2 I(r,t)$, where $n_2$ is the nonlinear index and $I(r,t)$ is the pulse intensity. With an additional hard aperture in the cavity, only high intensity pulses will self-focus sharply enough to avoid diffractive losses at the aperture and see round-trip amplification. The Kerr lens mode locking mechanism is inherently broadband and spontaneous. Thus, pulses down to a few femtosecond can be generated.

Femtosecond pulses can have very high peak power and under such high peak power, laser rod material can be damaged which prevents the pulses to get amplified further. A typical femtosecond oscillator generates nanojoule level pulse energies. To further amplify femtosecond pulses, a chirped pulse amplification scheme was invented, which won the 2018 Nobel prize[35]. It involves stretching the seed pulse

in time by a few orders of magnitude, and then amplifying the stretched pulse without reaching the threshold for material damage or non-linearity as the peak power is now low. Then the amplified pulse is compressed to the original pulse duration[36]. The pulse stretcher and compressors can be achieved using dispersive components such as gratings. A typical scheme of ultrashort pulse amplification is shown in Figure 2.1

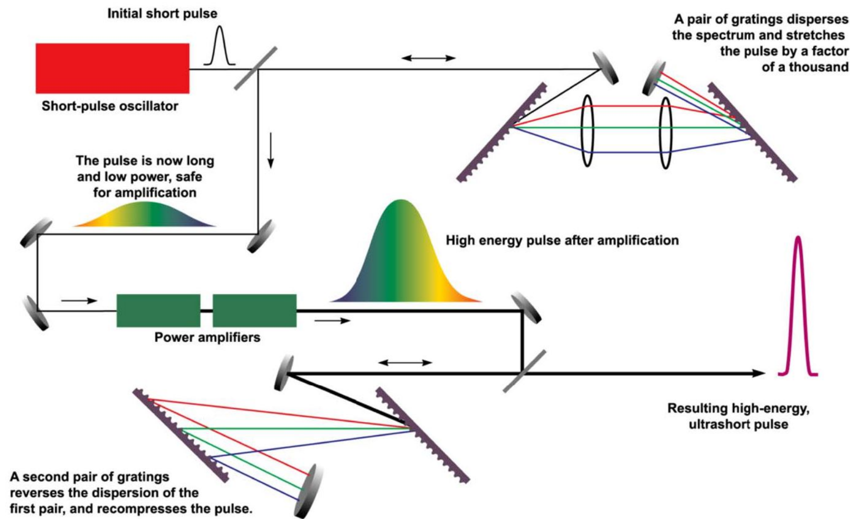


Figure 2.1: Schematic of a chirped pulse amplification laser system. Adapted from reference[36]. Reprinted with permission from Lawrence Livermore National Laboratory.

Kerr lens mode locking and chirped pulse amplification enable unprecedented femtosecond laser pulse energy and peak power, which opens door to a new regime of material interaction and precision material processing[16].

In the next chapter, we will discuss common nonlinear phenomenon generated

by ultrashort pulses in transparent materials.

# CHAPTER 3

## Ultrashort pulse phenomenon in transparent materials

Electromagnetic waves propagate following the four Maxwell equations[37],

$$\nabla \times \mathbf{E} = -\frac{\partial \mathbf{B}}{\partial t} \tag{3.1}$$

$$\nabla \times \mathbf{B} = \mu_0(\mathbf{J} + \frac{\partial \mathbf{D}}{\partial t}) \tag{3.2}$$

$$\nabla \cdot \mathbf{E} = \frac{\rho}{\varepsilon_0} \tag{3.3}$$

$$\nabla \cdot \mathbf{B} = 0 \tag{3.4}$$

where $\mathbf{E}$ and $\mathbf{B}$ are the electric and magnetic fields, $\mathbf{D}$ is the electric displacement field, $\mathbf{J}$ is the free charge current density, $\rho$ is the free charge density, $\mu_0$ is the free space permeability, and $\varepsilon_0$ is the free space permittivity.

By applying a curl operation on both side of equation 3.1 and inserting equation 3.2 into the right hand side, we obtain the wave equation that defines the propagation of laser pulse in a transparent material, equation 3.5.

$$\nabla^2 \mathbf{E} - \nabla(\nabla \cdot \mathbf{E}) = \mu_0(\frac{\partial \mathbf{J}}{\partial t} + \frac{\partial^2 \mathbf{D}}{\partial t^2}) \tag{3.5}$$

In isotropic and homogeneous media, the displacement relation is expressed by

$$\mathbf{D} = \varepsilon_0 \mathbf{E} + \mathbf{P} \tag{3.6}$$

The response of the medium can be described by a linear part of $\mathbf{P}^{(1)}$ in the weak field regime and a nonlinear part $\mathbf{P}^{(NL)}$ in the strong field regime. In the weak field regime, the first-order polarization is a linear function of the electric field,

$$\begin{aligned}\mathbf{P} &= \mathbf{P}^{(1)} + \mathbf{P}^{(NL)} \\ &= \varepsilon_0\chi^{(1)}\mathbf{E} + \varepsilon_0\chi^{(2)}\mathbf{E}\mathbf{E} + \varepsilon_0\chi^{(3)}\mathbf{E}\mathbf{E}\mathbf{E} + \cdots\end{aligned} \tag{3.7}$$

Equation 3.5, 3.6, and 3.7 are the starting point of describing laser pulse propagation in transparent medium and its associated linear and nonlinear phenomenon.

## 3.1 Diffraction

Diffraction is the most common effect when propagating a laser beam; it will always occur no matter in vacuum or in transparent medium. The mathematical description of diffraction is in the first term on the left hand side of equation 3.5. For a Gaussian beam, the severity of diffraction effects are expressed using the Rayleigh Length, which is the propagation distance at which the beam width increases by a factor of $\sqrt{2}$ is[38],

$$z_R = \frac{\pi n_0 w_0^2}{\lambda_0} \tag{3.8}$$

where $w_0$ is the beam waist, $\lambda_0$ is the laser wavelength, and $n_0$ is the refractive index of the medium.

### 3.2 Dispersion

Ultrashort pulses have wide spectrum. Typically for a pulse duration of 100 fs, the pulse bandwidth will be greater than 10 nm. When pulses that carry many frequency components propagate in transparent materials such as glass, different frequencies will travel at a slightly different speed. In the normal dispersion region, red frequencies travel faster than blue frequencies. This leads to the initial overlapped frequency components becoming spread over time and space with red frequencies in the leading part of the pulse and blue frequencies in the trailing part of the pulse. This effect is the so called group velocity dispersion and can be characterized by the dispersive length[38],

$$L_{GVD} = \frac{t_p^2}{2k''} \tag{3.9}$$

where $t_p$ is the pulse duration, $k'' = \partial^2 k/\partial\omega^2|_{\omega_0}$ is the coefficient of the second order Taylor expansion of $k(\omega) = n(\omega)\omega/c$ around the central frequency $\omega_0$.

### 3.3 Self focusing

The refractive index of a material depends on the incident pulse intensity distribution in the nonlinear regime. The intensity dependent index can be expressed by[39],

$$n = n_0 + n_2 I(r,t) \tag{3.10}$$

The nonlinear Kerr index $n_2$ is related to the third order susceptibility $\chi^{(3)}$ by[39],

$$n_2 = \frac{3\chi^{(3)}}{4\varepsilon_0 c n_0^2} \tag{3.11}$$

The nonlinear coefficient $n_2$ is typically positive, which leads to higher refractive index in the presence of intense pulse. For a Gaussian beam, the on axis intensity is the highest and the index profile in the transverse plane follows the intensity distribution of the beam similar to the effect of a positive focusing lens. This self focusing effect can lead to beam collapse in the absence of other saturating effect, as shown in Figure 3.1.

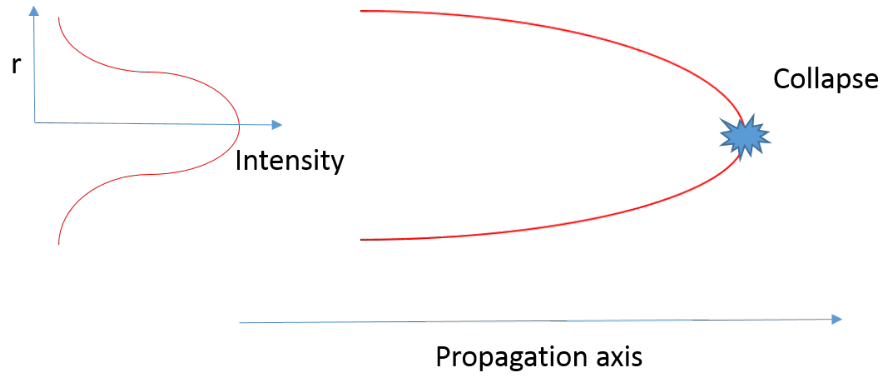


Figure 3.1: Self focusing of a beam by Kerr lens effect, when self focusing is stronger than diffraction and in the absence of other nonlinear effect the beam will collapse.

The strength of the self-focusing effect is characterized by a critical power $P_{cr}$ above which the beam will collapse[40]. The self-focusing critical power is given by[40],

$$P_{cr} = \frac{3.77\lambda_0^2}{8\pi n_0 n_2} \tag{3.12}$$

For $\lambda_0 = 1064\,\mathrm{nm}$ the critical power for self-focusing in glass is about 3.5 MW.

## 3.4 Self phase modulation

The self phase modulation effect is the appearance of new frequencies due to the temporal variation of the intensity dependent index $n = n_0 + n_2 I(r,t)$. A simple relation of frequency and phase can be expressed as,

$$\omega(t) = -\frac{\partial \phi}{\partial t} = \omega_0 - \frac{n_2 \omega_0}{c} z \frac{\partial I(r,t)}{\partial t} \tag{3.13}$$

The frequency depends on the slop of the pulse $\partial I/\partial t$; the leading pulse edge generates longer wavelengths and the trailing edge of the pulse generates shorter wavelengths. This effect is a major contributor in continuum generation that covers wavelengths from visible to infrared spectrum.

## 3.5 Photon ionization

When an ultrashort pulse hits a transparent material, the pulse can experience the above-mentioned effects such as self focusing and self phase modulation. In the mean time, the medium itself will be ionized by the pulse and the plasma generated in the process will in return have an effect on the pulse itself. There are two major channels for electrons to jump from valence band to conduction band when excited by an ultrashort pulse, multiphoton ionization and tunneling ionization.

For an extremely strong laser field, the process falls into the tunneling ionization regime. In this process, the laser field is so strong that it bends the Coulomb well that confines a valence band electron and the electron tunnels through the barrier and becomes free, as shown in Figure 3.2(b).

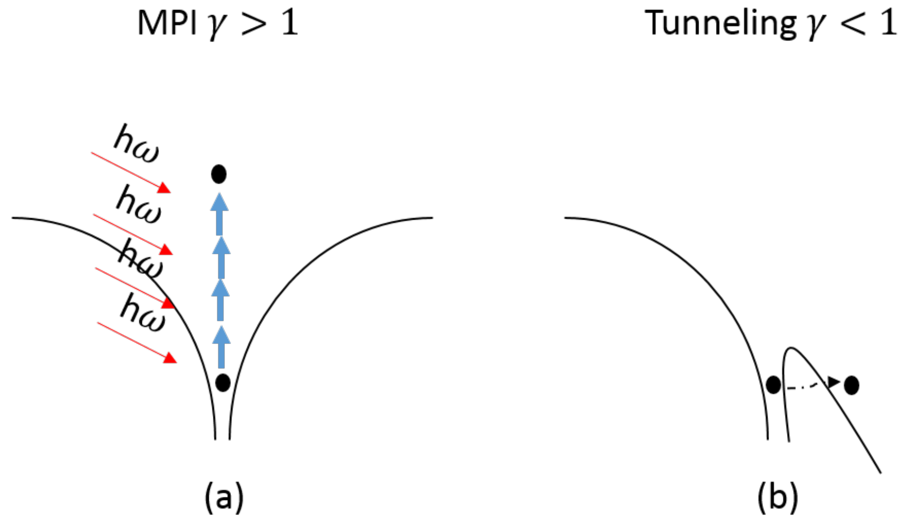


Figure 3.2: Schematic diagram of multiphoton ionization(a) and tunneling ionizaton(b) for different values of the Keldysh parameter $\gamma$.

For strong fields which are not quite strong enough to cause tunneling ionization, the process falls into the multiphoton ionization regime. The multiphoton ionization process supplies multiple photons simultaneously to promote a valance band electron to the conduction band, as shown in Figure 3.2(a).

Keldysh theory describes both phenomenon in the same framework[41]. The relative role of multiphoton ionization and tunneling ionization can be characterized

by the Keldysh parameter,

$$\gamma = \frac{\omega_0 \sqrt{mU_i}}{e\mathcal{E}} \tag{3.14}$$

where $\omega_0$ is the laser frequency, m is the reduced electron mass, e is the electron charge, $U_i$ is the band gap of the material, $\mathcal{E}$ is the electrical field envelope that relates to the laser intensity by

$$I = \frac{1}{2}\varepsilon_0 c n_0 \mathcal{E}^2. \tag{3.15}$$

When $\gamma < 1$, the photon ionization is dominated by the tunneling process. When $\gamma > 1$, the photon ionization is dominated by the multiphoton ionization process. When $\gamma \sim 1$, both tunneling and multiphoton ionization will play a role[9].

In Figure 3.3, we plot the photon ionization rate vs the laser intensity for wavelength of 1064 nm and band gap of 3.7 ev in borosilicate glass follow the Keldysh formula[41],

$$W_{PI}(|\mathcal{E}|) = \frac{2\omega_0}{9\pi}(\frac{\omega_0 m}{\hbar\sqrt{\Gamma}})^{3/2} Q(\gamma, x) exp(-\alpha\lceil x+1 \rceil) \tag{3.16}$$

$$\Gamma = \gamma^2/(1+\gamma^2) \tag{3.17}$$

$$\Xi = 1 - \Gamma \tag{3.18}$$

$$Q(\gamma, x) = \sqrt{\frac{\pi}{2K(\Xi)}} \times \Sigma_{n=0}^{\infty} exp(-n\alpha)\Phi[\sqrt{\beta(n+2v)}] \tag{3.19}$$

$$\alpha = \pi\frac{K(\Gamma) - E(\Gamma))}{E(\Xi)} \tag{3.20}$$

$$\beta = \frac{\pi^2}{4K(\Xi)E(\Xi)} \tag{3.21}$$

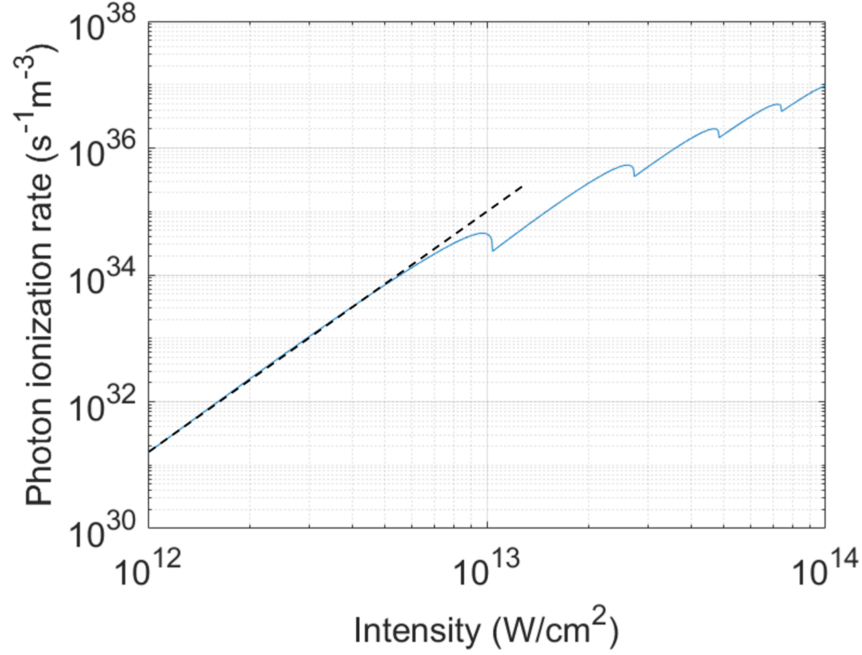


Figure 3.3: Photo ionization rate as a function of laser intensity at a wavelength of 1064 nm in borosilicate glass with bandgap of 3.7 eV. The solid line is based on the full expression of equation 3.16. The dashed line is an MPI approximation.

.

$$x = \frac{2U_i}{\pi\hbar\omega_0\sqrt{\Gamma}}E(\Xi) \tag{3.22}$$

$$v = \lceil x + 1 \rceil - x \tag{3.23}$$

where $\lceil \cdots \rceil$ denotes the integer part, $K$ and $E$ are the elliptical integral of the first and second kind, $\Phi$ is the Dawson function $\Phi(z) = \int_0^z exp(y^2 - z^2)dy$.

At an intensity level of $10^{13}$ W/cm$^2$ or less, the photon ionization rate can be approximated well by the multiphoton ionization rate $W_{PI} = \sigma_K I^K \rho_{at}$ as shown in the dashed line in Figure 3.3.

### 3.6 Avalanche ionization

The electrons in the conduction band excited by the photon ionization process will further accumulate energy in the laser field and become even more energetic. This electron can then collide with another valance band electron and transfer part of the energy to it. The result is two conduction band electrons after collision. And these ionized electrons can further impact more valence band electrons in the wake of the laser field and become an avalanche process.

### 3.7 Plasma generation

The evolution of electron density $\rho$ describing photon ionization and avalanche ionization can be written as[9],

$$\frac{\partial \rho}{\partial t} = W_{PI} + \eta \rho \left|\mathcal{E}\right|^2 - \frac{\rho}{\tau_r} \tag{3.24}$$

where $W_{PI}$ is the photon ionization rate, $\eta = \sigma/U_i$ is the avalanche ionization coefficient, $\sigma$ is the cross section for inverse Bremsstrahlung process[42] following the Drude model, and $\tau_r$ is the electron recombination time.

### 3.8 Plasma absorption and defocusing

When the medium is ionized by intense pulses, the plasma will absorb part of the pulse energy and defocus the beam to stop the beam from collapsing to singularity.

The evolution of plasma current density follows the Drude model[43],

$$\frac{\partial \mathbf{J}}{\partial t} + \frac{\mathbf{J}}{\tau_c} = \frac{q_e^2}{m_e}\rho \mathbf{E} \tag{3.25}$$

where $\tau_c$ is the electron collision time. Solving equation 3.25 in the Fourier domain we can get,

$$\frac{\omega}{c}\frac{\mathbf{J}}{\varepsilon_0 c} = k(\omega)\sigma(\omega)\rho \mathbf{E} \tag{3.26}$$

$$\sigma(\omega) = \frac{\omega_0}{n(\omega) c \rho_c} \frac{\omega_0 \tau_c (1 + i\omega\tau_c)}{(1 + \omega^2 \tau_c^2)} \tag{3.27}$$

where $\rho_c = \varepsilon_0 m_e \omega_0^2 / q_e^2$ is the critical plasma density above which the plasma becomes opaque to the laser beam. The real part of $\sigma(\omega)$ is equal to the cross section for inverse Bremsstrahlung. The real part of the current in equation 3.26 accounts for plasma absorption and the imaginary part accounts for plasma defocusing[44].

## 3.9 Conclusions

In conclusion, we discussed some common effects including diffraction, dispersion, self focusing, self phase modulation, photon ionization, avalanche ionization, plasma generation, plasma absorption and plasma defocusing in ultrashort pulse interaction with transparent materials.

In Chapter 5, we will couple all the phenomenon discussed above into a pulse propagation model to have a full picture of ultrashort pulse propagation in transparent materials.

# CHAPTER 4

## Bulk modification by ultrashort pulse

In this chapter, we present experimental results of ultrashort pulse material modification in three types of important materials: borosilicate glass, fused silica, and sapphire. To understand the fundamental picture of material interaction and the morphology of the laser modified region, we focus on studying a single shot of picosecond laser pulse in the bulk of the materials.

The experimental setup used in our study is shown in Figure 4.1. The laser source is a commercially available Nd:YAG system from Lumentum. It delivers 10 ps pulses at a center wavelength of 1064 nm with a repetition rate up to 8.2 MHz. The output beam intensity has a close to perfect Gaussian distribution. The maximum available pulse energy from the system is about 400 μJ, which is more than enough for the pulse energy needs in our experiments. The pulse energy is attenuated by a half-wave plate and two prism wedges combination. The first prism wedge is positioned close to the Brewster's angle of the incoming laser beam. This attenuation scheme combined with the analog laser power control enables us to continuously adjust the pulse energy down to sub-microjoule level while maintaining relatively pure polarization state of the attenuated laser beam. A similar method has been used

in previous study[45]. An infinity-corrected microscope objective with numerical aperture of NA=0.25 is used to focus the beam into the bulk of borosilicate glass plate. The spot size in our experiments is about 5 µm.

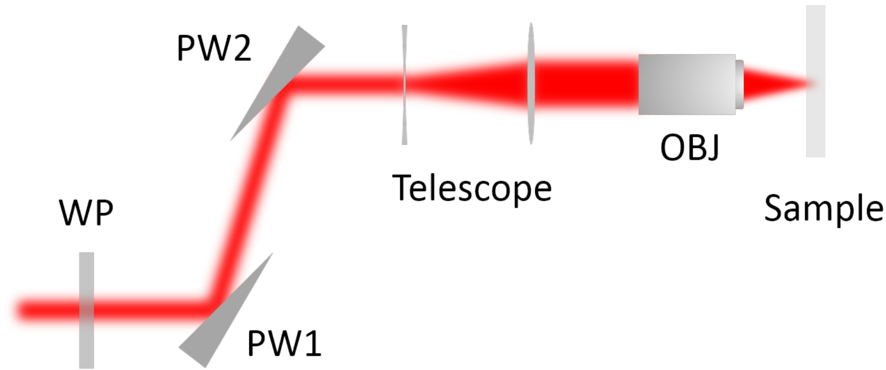


Figure 4.1: Schematic of the experimental setup, WP: $\lambda/2$ plate; PW1, PW2: prism wedge; Telescope: telescope beam expander, OBJ: microscope objective

The glass plate is mounted on a linear motorized stage. To ensure single shot exposure, the laser system is operated at a repetition rate of 2 kHz while the stage is translated at a speed of 200 mm/s. The combined effect is a pulse to pulse distance of about 100 µm, which is about 20 times larger than the spot size. The sample and linear motorized stage are mounted on a precision Z-positioning stage that can be accurately adjusted to tune the focal position. A careful adjustment procedure has been implemented to make sure the beam is focused about 100 µm underneath the borosilicate glass surface. The pulse energy is carefully measured at the output of the objective with a precision power meter. To visualize the modified region, we use a high magnification optical microscope with backside illumination to observe the

laser modified region from the side edge of the glass plate.

## 4.1 Borosilicate glass

Borosilicate glass is one of the most popular glasses used in applications from containers to wind shield. It has stable chemical and physical properties, and most importantly it is available at very cheap price. It is in every aspect of modern life, thus, it is critical to understand ultrashort pulse interaction with it and its modification morphology.

The borosilicate glass plate used in our experiments has thickness of about 1 mm. The experimental results of ultrashort pulse modification inside borosilicate glass are shown in Figure 4.2. For all the cases, we found no surface damage on the glass plate. At around pulse energy of about 1 µJ, we start observing bulk modification inside the borosilicate glass plate. The length of the modification site increases as we increase the pulse energy from 1 µJ to 5 µJ. The starting point of the modification shifts towards the incoming laser beam as the increased nonlinear effects cause the beam to generate plasma sooner. This phenomenon is also observed in other studies[21, 22, 11].

At pulse energy of 5 µJ, the modification track reaches to a length of about 38 µm, which is about 1.4 times of the Rayleigh length under our focusing geometry. The modification track has an inner width to length aspect ratio of about 1:10 at

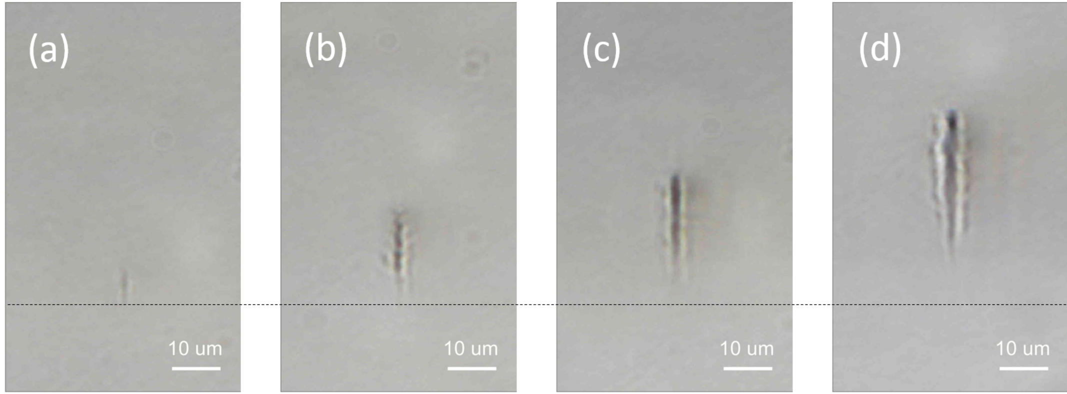


Figure 4.2: Modification created inside borosilicate glass using single shot of picosecond laser pulse. The focal position is marked by the dashed line. The laser beam is propagating from top to bottom. The pulse energy is chosen to produce from just visible laser modification to obvious modification tracks inside the glass plate. For the cases shown here, the pulse energy are (a) 1 µJ, (b) 2 µJ, (c) 3 µJ, (d) 5 µJ.

this energy level. The morphology of the modification track appears to have distinct inner and outer features where the inner modification zone appears to be darker with a hollow like shape. Similar morphology has been observed using tightly focused Gaussian beams in fused silica and sapphire[15, 46].

Compared to multiple pulse irradiation, we do not observe a thermal impacted zone outside of the modification track that extends to 50 µm or more[21]. And this can be understood as no significant heat accumulation in the single shot scenario. However, the features of the modification track are more rich in the single pulse case as shown in Figure 4.2 as it is revealing nonlinear phenomenon such as self focusing.

## 4.2 Fused silica

Fused silica is another important material that has wide applications in modern optics. It acts as the basic building block for lots of applications such as lasers, microscopes, fibers etc.. Because of its strategic importance, it has been actively studied in the optics community and ultrashort pulse interaction with fused silica is an active research topic.

The fused silica glass plate used in our experiments has a thickness of about 3 mm. And we use the same setup as mentioned in section 4.1 to generate single shot modification in the bulk of fused silica glass.

The experimental results of ultrashort pulse modification inside fused silica glass are shown in Figure 4.3. For all the cases, we found no surface damage on the glass plate. At around pulse energy of about 1.5 µJ, we start observing bulk modification inside the fused silica glass plate. The length of the modification track increases as we increase the pulse energy from 1.5 µJ to 3 µJ. And the starting point of the modification track shifts towards the incoming laser beam as nonlinear effect drives the plasma generation towards the incoming beam when we increase the pulse energy. This is similar to what we observed in the borosilicate glass case.

The morphology of the modified region in fused silica glass is different from borosilicate glass as shown in Figure 4.3. At pulse energy of 3 µJ, the modification

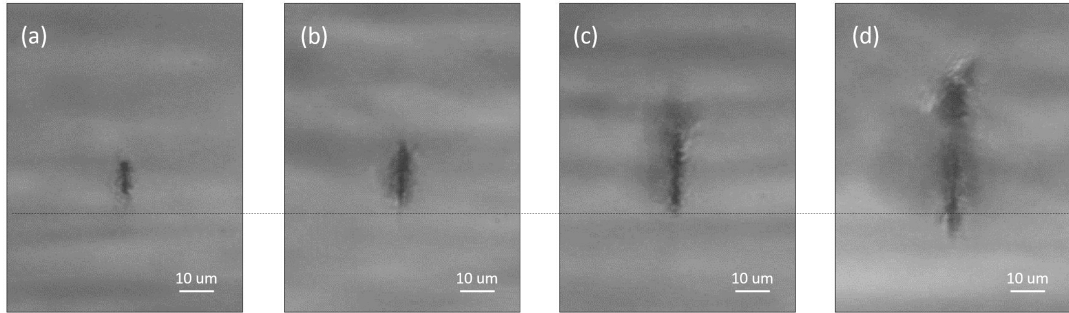


Figure 4.3: Modification created inside fused silica glass using single shot of picosecond laser pulse. The focal position is marked by the dashed line. The laser beam is propagating from top to bottom. The pulse energy is chosen to produce from just visible laser modification to obvious modification tracks inside the glass plate. For the cases shown here, the pulse energy are (a) 1.5 µJ, (b) 2 µJ, (c) 2.5 µJ, (d) 3 µJ.

track reach to a length of about 44 µm. In the fused silica glass, there is no hollow type inner core structure presenting. Instead, the center appears to be dark and at around 3 µJ there appears to be cracks generated as shown in Figure 4.3(d).

## 4.3 Sapphire

Sapphire is the second hardest material on earth next to diamond. It is widely used in ultrafast lasers as a gain medium. And recently has been used to generate super high pressure microexplosions in a lab scale setup[46]. Here we study how a common industrial ultrashort pulse laser interacts with sapphire to understand the basic modification morphology.

The sapphire plate used in our experiment is a C-plane cut sapphire with thick-

ness of about 0.5 mm. And we use the same setup as mentioned in section 4.1 to generate single shot laser modification in the bulk of sapphire.

The experimental results of laser modification inside sapphire are shown in Figure 4.4. For all the cases, we found no surface damage on the laser entrance surface. At a pulse energy of about 1 µJ, we start observing bulk modification inside the sapphire plate. The length of the modification track increases as we increase the pulse energy from 1 µJ to 3 µJ. And the starting point of the modification track shifts towards the incoming laser beam as nonlinear effect drives the plasma generation towards the incoming beam when we increase the pulse energy. This is similar to what we observed in the borosilicate glass and fused silica cases.

The morphology of the laser modified region in sapphire is different from both borosilicate glass and fused silica as shown in Figure 4.4. At a pulse energy of 1 µJ, we start observing beaded structures that spread along the beam propagation axis. When we increase the pulse energy, the beaded structure become more obvious with darker core and spread further along the propagation axis. At pulse energy of 2.5 µJ, the beaded structure extended to a length of more than 30 µm. The beads appear in the front portion, and become obvious with hollow type structures. The beaded structure then disappears towards the tail of the modified region as shown in Figure 4.4(d), indicating the pulse energy dissipated before reaching the geometrical focus.

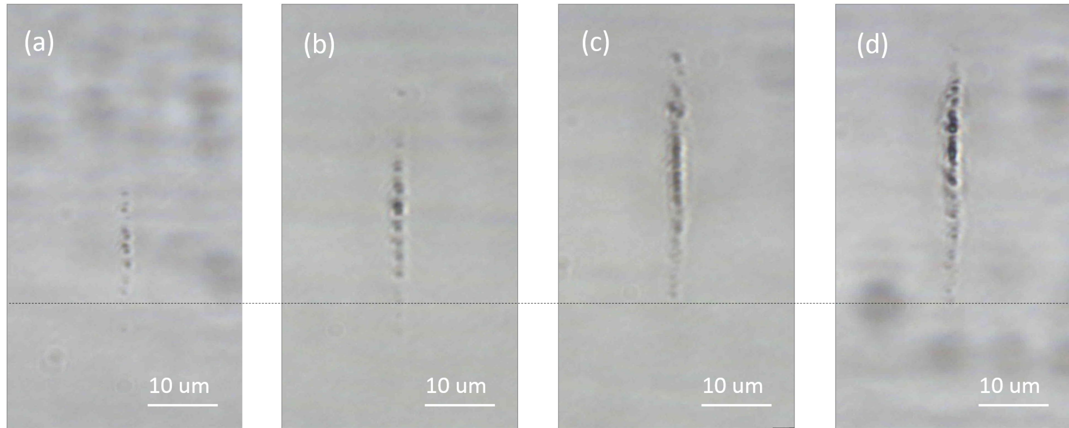


Figure 4.4: Modification created inside sapphire plate using single shot of picosecond laser pulse. The focal position is marked by the dashed line. The laser beam is propagating from top to bottom. The pulse energy is chosen to produce from just visible laser modification to obvious modification tracks inside the sapphire plate. For the cases shown here, the pulse energy are (a) 1 µJ, (b) 1.5 µJ, (c) 2 µJ, (d) 2.5 µJ.

## 4.4 Conclusions

In conclusion, we demonstrated single shot ultrashort pulse modification in transparent materials such as borosilicate glass, fused silica, and sapphire. In our study, we used an industrially available and widely used picosecond laser source operating at 1064 nm wavelength with pulse duration of 10 ps. We observed focus shift towards the incoming laser beam for all the materials driven by nonlinear effects such as self focusing and self phase modulation. The morphology of the laser modified regions are significantly different from borosilcate glass to fused silica to sapphire.

The features of a single-shot-pulse modified region also show different characteristics compared with multiple pulse irradiation. In the following chapters, we will present a pulse propagation model and study the pulse behavior numerically.

# CHAPTER 5

## Model of ultrashort pulse propagation and electron dynamics

In this chapter, we put together the phenomenon discussed in chapter 3 into a complete model that describes pulse propagation in transparent material. We briefly introduce the extended Crank-Nicolson scheme that has been used for solving nonlinear differential equations, particularly in the format of nonlinear pulse propagation and finally we present an algorithm to implement the Crank-Nicolson scheme in Matlab.

### 5.1 Model pulse propagation

Insert the electric field displacement 3.6 into the wave equation 3.5 we get,

$$\nabla^2\mathbf{E} - \nabla(\nabla\cdot\mathbf{E}) - \frac{1}{c^2}\frac{\partial^2}{\partial t^2}\int_{-\infty}^{t}\varepsilon(t-t')\mathbf{E}(r,t',z)dt' = \mu_0\left(\frac{\partial\mathbf{J}}{\partial t} + \frac{\partial^2\mathbf{P}}{\partial t^2}\right) \tag{5.1}$$

where $\mathbf{E}$, $\mathbf{J}$, and $\mathbf{P}$ depend on space-time domain $(r,t,z)$.

The frequency domain representation of equation 5.1 can be expressed more concisely as,

$$\nabla^2\hat{\mathbf{E}} - \nabla(\nabla\cdot\hat{\mathbf{E}}) + \frac{\omega^2 n(\omega)^2}{c^2}\hat{\mathbf{E}} = \mu_0(-i\omega\hat{\mathbf{J}} - \omega^2\hat{\mathbf{P}}) \tag{5.2}$$

where $\hat{\mathbf{E}}$, $\hat{\mathbf{J}}$, and $\hat{\mathbf{P}}$ depend on space-frequency domain $(r,\omega,z)$.

To simplify the vectoral wave equation 5.2, we assume the electric field is linearly polarized and the polarization direction is perpendicular to the propagation direction defined by the wave vector $\mathbf{k}$. The medium response terms $\mathbf{J}$ and $\mathbf{P}$ are also transverse. This assumption is valid for laser beam propagation that is not too strongly focused[44]. Under this assumption the second term $\nabla \cdot \hat{\mathbf{E}}$ on the left hand side can be neglected. Rewriting equation 5.2 in a scalar form by projecting the field to the polarization direction, we get[44],

$$(\partial_z^2 + \nabla_\perp^2)\hat{E} + k(\omega)^2\hat{E} = \mu_0(-i\omega\hat{J} - \omega^2\hat{P}) \tag{5.3}$$

where $k(\omega) = n(\omega)\omega/c$.

Change the lab frame to the pulse local frame to follow the pulse in its motion by introducing,

$$z \to z, \quad \tau \to t - z/v_g \tag{5.4}$$

$$\partial_z = \partial_z - (1/v_g)\partial_\tau, \quad \partial_t = \partial_\tau \tag{5.5}$$

where $v_g = \partial\omega/\partial k|_{\omega_0}$ is the group velocity of the pulse.

Inserting $\partial_z \to \partial_z + i(\omega/v_g)$ into equation 5.3, we get,

$$\partial_z^2\hat{E} + 2i\frac{\omega}{v_g}\partial_z\hat{E} = -\nabla_\perp^2\hat{E} - [k(\omega)^2 - \frac{\omega^2}{v_g^2}]\hat{E} - \frac{\omega^2}{c^2}\frac{\hat{P}}{\varepsilon_0} - i\frac{\omega}{c}\frac{\hat{J}}{\varepsilon_0 c} \tag{5.6}$$

The pulse propagation model, the electrical field is typically described by a field

envelope function with a carrier wave of frequency $\omega_0$,

$$E(r,t,z) = \mathcal{E}(r,t,z)exp(ik_0 z - i\omega_0 t) \tag{5.7}$$

In the local pulse frame, using the relation in equation 5.4, we get,

$$E(r,\tau,z) = \mathcal{E}(r,\tau,z)exp(i(k_0 - \omega_0/v_g)z - i\omega_0\tau) \tag{5.8}$$

So the derivative in local pulse frame reads,

$$\partial_z E = exp(i(k_0 - \omega_0/v_g)z - i\omega_0\tau)[\partial_z + i(k_0 - \omega_0/v_g)]\mathcal{E} \tag{5.9}$$

$$\partial_z^2 E = exp(i(k_0 - \omega_0/v_g)z - i\omega_0\tau)[\partial_z + i(k_0 - \omega_0/v_g)]^2\mathcal{E} \tag{5.10}$$

Rewriting equation 5.6 with the help of envelop decomposition relation 5.9 and 5.10, we get,

$$\partial_z^2\hat{\mathcal{E}} + 2i\kappa(\omega)\partial_z\hat{\mathcal{E}} = -\nabla_\perp^2\hat{\mathcal{E}} - [k(\omega)^2 - \kappa(\omega)^2]\hat{\mathcal{E}} - \frac{\omega^2}{c^2}\frac{\hat{P}}{\varepsilon_0} - i\frac{\omega}{c}\frac{\hat{J}}{\varepsilon_0 c} \tag{5.11}$$

where $\kappa(\omega) = k_0 + (\omega - \omega_0)/v_g$

Under the slow variation approximation, the field amplitude and phase are evolving sufficiently slow along the propagation direction[44], which suggests,

$$|\partial_z^2\hat{\mathcal{E}}| << |2i\kappa(\omega)\partial_z\hat{\mathcal{E}}| \tag{5.12}$$

Neglecting the first term in equation 5.11, we get[44],

$$\partial_z\hat{\mathcal{E}} = \frac{i}{2\kappa(\omega)}\nabla_\perp^2\hat{\mathcal{E}} + i\frac{k(\omega)^2 - \kappa(\omega)^2}{2\kappa(\omega)}\hat{\mathcal{E}} + \frac{i}{2\kappa(\omega)}\frac{\omega^2}{c^2}\frac{\hat{P}}{\varepsilon_0} - \frac{1}{2\kappa(\omega)}\frac{\omega}{c}\frac{\hat{J}}{\varepsilon_0 c} \tag{5.13}$$

For a narrow spectrum pulse, we may only consider the second order dispersion, and neglect higher order dispersive terms[44],

$$\frac{k(\omega)^2 - \kappa(\omega)^2}{2\kappa(\omega)} = (k(\omega) - \kappa(\omega)) + \frac{(k(\omega) - \kappa(\omega))^2}{2\kappa(\omega)} \approx k''/2(\omega - \omega_0)^2 \tag{5.14}$$

Under the narrow spectrum approximation, $\kappa(\omega) \approx k_0$ and $\omega \approx \omega_0$.

The pulse propagation equation in the form of an envelope function with slowly varying envelope approximation, and narrow spectrum approximation can then be expressed as,

$$\partial_z \hat{\mathcal{E}} = \frac{i}{2k_0}\nabla_\perp^2 \hat{\mathcal{E}} + i\frac{k''(\omega - \omega_0)^2}{2}\hat{\mathcal{E}} + \frac{i}{2k_0}\frac{\omega_0^2}{c^2}\frac{\hat{P}}{\varepsilon_0} - \frac{1}{2k_0}\frac{\omega_0}{c}\frac{\hat{J}}{\varepsilon_0 c} \tag{5.15}$$

where $k'' = \partial^2 k/\partial\omega^2|_{\omega_0}$.

In space time domain, the pulse propagation equation 5.15 can be expressed as,

$$\partial_z \mathcal{E} = \frac{i}{2k_0}\nabla_\perp^2 \mathcal{E} - i\frac{k''}{2}\frac{\partial^2 \mathcal{E}}{\partial\tau^2} + \frac{i}{2k_0}\frac{\omega_0^2}{c^2}\frac{P}{\varepsilon_0} - \frac{1}{2k_0}\frac{\omega_0}{c}\frac{J}{\varepsilon_0 c} \tag{5.16}$$

Incorporating the phenomena we talked about in chapter 3 such as self focusing, photon ionization, avalanche ionization, plasma absorption, and plasma defocusing into the third and fourth term on the right hand side of equation 5.16, we get the evolution of the field envelope of an ultrashort pulse in transparent materials[9],

$$\frac{\partial \mathcal{E}}{\partial z} = \frac{i}{2k}\nabla_\perp^2 \mathcal{E} - i\frac{k''}{2}\frac{\partial^2 \mathcal{E}}{\partial\tau^2} + ik_0 n_2 |\mathcal{E}|^2 \mathcal{E} - \frac{\sigma}{2}(1 + i\omega_0\tau_c)\rho\mathcal{E} - \frac{1}{2}\frac{W_{PI}U_i}{|\mathcal{E}|^2}\mathcal{E} \tag{5.17}$$

The first term in the right hand side of equation 5.17 describes diffraction in the transverse plane. The second term accounts for group velocity dispersion. The third

term accounts for Kerr self-focusing with critical power $P_{cr} = \lambda^2/2\pi n_0 n_2 = 3.5\,\mathrm{MW}$, where $n_2 = 3.45 \times 10^{-16}\,\mathrm{cm}^2/\mathrm{W}$[11] is the nonlinear part of the refractive index. The fourth term accounts for plasma absorption and plasma defocusing; the cross section for inverse Bremsstrahlung follows the Drude model[9] and the cross section $\sigma = k\omega_0\tau_c/n_0^2\rho_c(1 + \omega_0^2\tau_c^2) = 9.7 \times 10^{-19}\,\mathrm{cm}^2$, where $\tau_c = 2.33 \times 10^{-14}\,\mathrm{s}$ denotes electron collision time and $\rho_c = 10^{21}\,\mathrm{cm}^{-3}$ is the critical plasma density at which level the plasma becomes opaque[9]. The fifth term describes the photon ionization of the media by the laser pulse, where $U_i = 3.7\,\mathrm{eV}$ is the band gap of borosilicate glass.

This model has been widely applied for propagating intense pulses in fused silica[9], air[47], and liquids[48].

We model the linearly polarized beam by the electric field envelope $\mathcal{E}$ of the electric field $E$ in cylindrical symmetry coordinates around the propagation axis z. The electric field envelope $\mathcal{E}$ at the starting position can be expressed by,

$$\mathcal{E}(r,t,0) = \mathcal{E}_0 exp(-r^2/w_0^2 - t^2/t_p^2 - ikr^2/2f) \tag{5.18}$$

where $\mathcal{E}_0$ is the amplitude of the initial field, $w_0 = w_f(1 + d^2/z_f^2)^{1/2}$ is the beam radius at the start position of the simulation, $w_f = 2.5\,\mu\mathrm{m}$ is the beam waist, d is the distance between the focus and the start position, $z_f = \pi w_f^2 n_0/\lambda_0 = 27.7\,\mu\mathrm{m}$ is the Rayleigh length, $t_p = 10\,\mathrm{ps}$ is the FWHM pulse duration, $k = n_0\omega_0/c$, $n_0 = 1.5$

for borosilicate glass, $\omega_0$ is the frequency of the carrier wave, $f = d + z_f^2/d$ is the curvature of the beam at the starting position.

In the borosilicate case, the maximum intensity used is $I = 2.54 \times 10^{12}\,\mathrm{W/cm^2}$, which corresponds to the Keldysh parameter $\gamma = \omega_0\sqrt{0.64 m_e U_i}/e\mathcal{E} = 2$[41]. When $\gamma > 1$, the multiphoton ionization process will be dominating, while $\gamma < 1$ the tunneling ionization process will be dominant. Thus, we approximate the photon ionization rate to the multiphoton ionization rate $W_{PI} = \sigma_4 I^4 \rho_{at}$, where $\sigma_4$ is the cross section for a four photon process to promote an electron from valence band to conduction band at 1064 nm in borosilicate glass.

## 5.2 Model electron generation

The electron excitation by the laser pulse from valence band to conduction band can be described through a rate equation discussed in chapter 3 equation 3.24 [9],

$$\frac{\partial \rho}{\partial t} = W_{PI} + \eta\rho\,|\mathcal{E}|^2 - \frac{\rho}{\tau_r} \tag{5.19}$$

The first term on the right hand side describes the electron promotion through multiphoton ionization and the second term describes electron generation through avalanche ionization, where $W_{PI} = \sigma_4 I^4 \rho_{at}$, $\eta = \sigma/U_i$ and $\rho_{at} = 2.1 \times 10^{22}\,\mathrm{cm^{-3}}$ is the background atom density. The third term represents electron recombination with a characteristics time $\tau_r = 150\,\mathrm{fs}$ in glass[49].

## 5.3 Extended Crank-Nicolson scheme

In this section, we briefly describe the numerical implementation of the pulse propagation model using the extended Crank-Nicolson scheme[50]. The pulse propagation model presented in equation 5.17 can be simplified by two major portions, the linear diffraction part and the nonlinear part, expressed as,

$$\frac{\partial \mathcal{E}}{\partial z} = \frac{i}{2k_0}\Delta_\perp \mathcal{E} + N(\mathcal{E}) \tag{5.20}$$

where $\Delta_\perp = \nabla_\perp^2$.

Under the extended Crank-Nicolson scheme, equation 5.20 can be discretized as[44],

$$E_j^{n+1} - E_j^n = i\delta(\Delta_j E_j^{n+1} + \Delta_j E_j^n) + (\frac{3}{2}N_j^n - \frac{1}{2}N_j^{n-1}) \tag{5.21}$$

where the coefficients 3/2 and $-1/2$ in the nonlinear terms are there to ensure second order accuracy, $\delta = \Delta z/4k_0(\Delta r)^2$, and $\Delta_j$ is the discretized diffraction operator,

$$\Delta_j E_j^n = E_{j-1}^n - 2E_j^n + E_{j+1}^n + \frac{v}{2j}(E_{j+1}^n - E_{j-1}^n) \tag{5.22}$$

where $v = 0$ is for planar geometry and $v = 1$ is for cylindrical geometry.

Rearranging equation 5.21 by organizing $E_j^{n+1}$ to the left hand side and $E_j^n$ to the right hand side of the equation, we get,

$$(1 - i\delta\Delta_j)E_j^{n+1} = (1 + i\delta\Delta_j)E_j^n + (\frac{3}{2}N_j^n - \frac{1}{2}N_j^{n-1}) \tag{5.23}$$

Defining $L_{-} = 1 - i\delta\Delta_j$ and $L_{+} = 1 + i\delta\Delta_j$, we get $E_j^{n+1}$,

$$E_j^{n+1} = (L_{-})^{-1}(L_{+}E_j^n + \frac{3}{2}N_j^n - \frac{1}{2}N_j^{n-1}) \tag{5.24}$$

Equation 5.24 represents propagating the field by one step, repeatedly applying it to the entire domain generates pulse propagation from the initial position to the ending position. The overall stability of the scheme depends on the nonlinear term, so a control of the z step $\Delta z$ is required, $\Delta z \leq k_0(\Delta r)^2$ is often found to be sufficient[44].

## 5.4 Implementing Crank-Nicolson scheme

Grouping the nonlinear terms and rewriting the pulse propagation equation 5.17 in the frequency domain, we get,

$$\frac{\partial\hat{\mathcal{E}}}{\partial z} = \frac{i}{2K(\Omega)}\triangle_{\perp}\hat{\mathcal{E}} + iD(\omega)\hat{\mathcal{E}} + \frac{i}{2K(\Omega)}\frac{\omega^2\hat{P}}{c^2\varepsilon_0} - \frac{1}{2K(\Omega)}\frac{\omega}{c}\frac{\hat{J}}{\varepsilon_0 c} \tag{5.25}$$

where $\hat{\mathcal{E}} = \hat{\mathcal{E}}(r, \Omega, z)$, $\Omega = \omega - \omega_0$, $K(\Omega) = K(\Omega, k_{\perp} = 0)$. The first term on the right hand side denotes diffraction, the second term denotes dispersion, the third and fourth terms denote nonlinear phenomenon such as self-focusing, plasma absorption, plasma defocusing, and photon ionization.

The self focusing term is expressed as,

$$\frac{\hat{P}}{\varepsilon_0} = 2n_0 n_2 I\hat{\mathcal{E}} \tag{5.26}$$

The plasma absorption and defocusing term is expressed as,

$$\frac{\omega}{c}\frac{\hat{J}}{\varepsilon_0 c} = k\sigma(\omega)\rho\hat{\mathcal{E}} \tag{5.27}$$

where $\sigma(\omega)$ can be found by equation 3.27. The real part of the current density in equation 5.27 accounts for plasma absorption and the imaginary part accounts for plasma defocusing.

The photon ionization term is expressed as,

$$\frac{\hat{J}}{\varepsilon_0 c} = n_0 \frac{W_{PI}(I)U_i}{I}\hat{\mathcal{E}} \tag{5.28}$$

The photon ionization rate can be found by equation 3.16. For multiphoton ionization $W_{PI}(I) = \sigma_K I^K \rho_{at}$, and $\sigma_k$ is the cross section for multiphoton ionization.

Following the same format as presented in equation 5.21, the pulse propagation equation 5.25 can be discretized by[44],

$$\hat{E}^{n+1}_{j,l} - \hat{E}^{n}_{j,l} = i\delta(\triangle_j \hat{E}^{n+1}_{j,l} + \triangle_j \hat{E}^{n}_{j,l}) + id_l(\hat{E}^{n+1}_{j,l} + \hat{E}^{n}_{j,l}) + \frac{3}{2}\hat{N}^{n}_{j,l} - \frac{1}{2}\hat{N}^{n-1}_{j,l} \tag{5.29}$$

where

$$\delta_l = \delta\frac{k_0}{K_l} = \frac{\Delta z}{4(\Delta r)^2 K_l} \tag{5.30}$$

$$d_l = \frac{\Delta z D_l}{2} \tag{5.31}$$

$$\hat{N}^{n}_{j,l} = \frac{i\Delta z}{2K_l}\frac{\omega_l^2}{\varepsilon_0 c^2}\hat{P}^{n}_{j,l} - \frac{\Delta z}{2K_l}\frac{\omega_l}{\varepsilon_0 c^2}J^{n}_{j,l} \tag{5.32}$$

Finally, the propagation of the field by one step can then be expressed as,

$$\hat{E}^{n+1}_{j,l} = L^{-1}_{-,l}[L_{+,l}\hat{E}^{n}_{j,l} + (3\hat{N}^{n}_{j,l} - \hat{N}^{n-1}_{j,l})/2] \tag{5.33}$$

where $L_{-,l} = 1 - id_l - i\delta_l\Delta_j$, $L_{+,l} = 1 + id_l + i\delta_l\Delta_j$

The above described pulse propagation model together with the electron rate equation can then be simulated in program languages such as Matlab. Here we list a high level description of the algorithm for simulating ultrashort pulse propagation in transparent material[44].

Step 1, define laser parameters, material constants(dispersion relation, nonlinearity)

Step 2, define simulation domain

- $r - grid$: $r_j = j\Delta r$, for $j = 0, \cdots, N_r + 1$
- $t - grid$: $t_l = t_{min} + l\Delta t$, for $l = 0, \cdots, N_t + 1$
- $\omega - grid$: $\omega_l = \omega_0 + l\Delta\omega$, for $l = 0, \cdots, N_\omega/2 - 1$, $\omega_l = \omega_0 - \pi/\Delta t + l\Delta\omega$, for $l = N_\omega/2, \cdots, N_\omega - 1$, with $\Delta\omega = 2\pi/(N_\omega\Delta t)$ and $N_\omega = N_t$
- calculate and store $K_l$, $D_l$, $d_l$, $\delta_l$, $p_l = \frac{i\Delta z}{2K_l}\frac{\omega_l^2}{\varepsilon_0 c^2}$, $u_l = -\frac{\Delta z}{2K_l}\frac{\omega_l}{\varepsilon_0 c^2}$

Step 3, define initial field, $E^0_{j,l} = \mathcal{E}(r_j, t_l, z = 0)$ follow equation 5.18, and transfer the field to spectrum domain by FFT: $\hat{E}^0_{j,l} = FFT(E^0_{j,l})$

Step 4, propagate the initial field and perform diagnostics each step and each M steps,

loop $k = 1, \cdots, K_{max}$

loop $m = 1, \cdots, M$

- $n = (k-1)M + m$
- calculate quantities for electron density $\rho_{j,l}^{n-1} = \rho(r_j, t_l, z_{n-1})$ by solving equation 5.19 for $j = 1, \cdots, N_r$
- calculate and store $P_{j,l}^{n-1}$, $J_{j,l}^{n-1}$ for $j = 1, \cdots, N_r$, $l = 0, \cdots, N_\omega - 1$
- perform FFT on $P_{j,l}^{n-1}$, $J_{j,l}^{n-1}$, and $E_{j,l}^{n-1}$, $\hat{P}_{j,l}^{n-1} = FFT(P_{j,l}^{n-1})$, $\hat{J}_{j,l}^{n-1} = FFT(J_{j,l}^{n-1})$, and $\hat{E}_{j,l}^{n-1} = FFT(E_{j,l}^{n-1})$
- calculate and store $\hat{N}_{j,l}^{n-1} = p_l \hat{P}_{j,l}^{n-1} + u_l \hat{J}_{j,l}^{n-1}$
- loop on frequency $l = 0, \cdots, N_\omega - 1$
  - calculate $L_{+,l}, L_{-,l}$
  - calculate $L_{-,l}^{-1}$
  - calculate $V_{j,l}^{n-1} = L_{+,l} \hat{E}_{j,l}^{n-1}$
  - calculate $S_{j,l}^{n-1} = V_{j,l}^{n-1} + (3\hat{N}_{j,l}^{n-1} - \hat{N}_{j,l}^{n-2})/2$
  - calculate $\hat{E}_{j,l}^{n} = L_{-,l}^{-1} S_{j,l}^{n-1}$
- end loop on frequency
- inverse Fourier transform $\hat{E}_{j,l}^{n}$ to $E_{j,l}^{n}$, for $j = 1, \cdots, N_r$

    - store $E^n_{j,l}$
    - perform fast diagnostics every step

  end inner loop

  perform slow diagnostics every m steps

end outer loop

The code implementation in Matlab is attached in Appendix A.

# CHAPTER 6

## Simulation results of ultrashort pulse propagation

In this chapter, the results of modeling ultrashort pulses propagating in transparent materials such as borosilicate glass and fused silica are presented. The laser parameters, focusing geometries and material properties are based on the experiments presented in chapter 4. We show the pulse behaviors and electron dynamics at different energy levels for both borosilicate glass and fused silica. We find that the electron density contour at $\rho = 10^{20}\,\mathrm{cm}^{-3}$ match the center of the modification track in the experiments very well. The relative role of electron contribution from multiphoton ionization and avalanche ionization are also presented for both glasses. Last but not the least, we extend our numerical study from picosecond pulse to femtosecond pulse, and the pulse behavior and the electron dynamics are investigated.

### 6.1 Borosilicate glass

Borosilicate glass is one of the most popular materials used in day-to-day containers, display glasses, windows, wind shields, optical devices and much more. It has stable chemical properties, relatively high physical strength, vast availability at relatively

low price, which makes borosilicate glass very attractive. Thus, it is crucial to understand how ultrashort pulse interact with it.

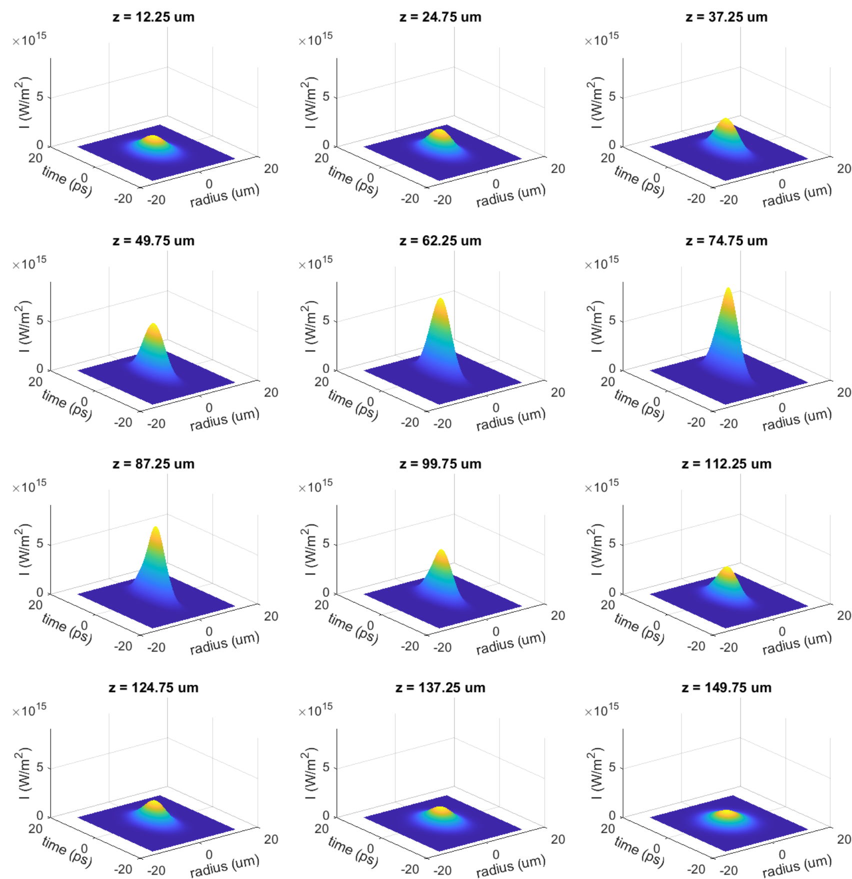


Figure 6.1: The evolution of pulse intensity profile at different propagation distance z in borosilicate glass with input pulse energy $E_{in} = 1\,\mu\mathrm{J}$

### 6.1.1 Pulse behavior

In this section we present the pulse propagation behavior in the bulk of borosilicate glass for different input pulse energies.

At input pulse energy of $E_{in} = 1\,\mu\text{J}$, the pulse intensity evolution at different propagation distance z are shown in Figure 6.1. At this energy level, the pulse propagates smoothly in the bulk of borosilicate glass and the peak of intensity is reached around the geometrical focus at $z = 75\,\mu\text{m}$.

To visualize the spatial focusing of the pulse, we plot the spatial distribution of maximum intensity along the propagation axis z, as shown in Figure 6.2.

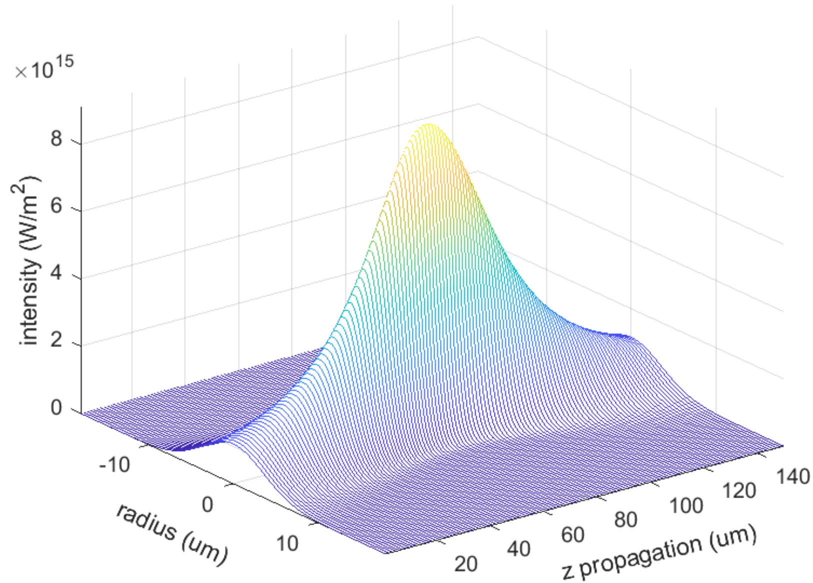


Figure 6.2: The spatial distribution of intensity along propagation axis z in borosilicate glass with pulse energy of $E_{in} = 1\,\mu\text{J}$.

The peak intensity is reached at around the geometrical focus. The radial profile of the beam maintains its Gaussian distribution while propagating which indicates a minimum level of nonlinearity.

To follow the temporal change of the pulse, we plot the on axis intensity distribution along the propagation axis z, as shown in Figure 6.3. At around the focus, the pulse shape deviates slightly from the Gaussian shape.

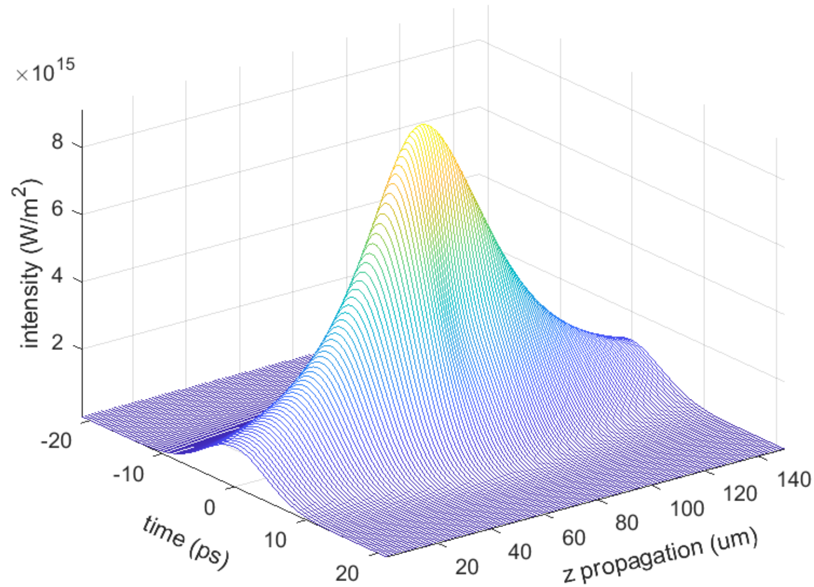


Figure 6.3: The on axis temporal distribution of intensity along propagation axis z in borosilicate glass with pulse energy of $E_{in} = 1\,\mu\text{J}$

Further increasing the input pulse energy will generate more obvious nonlinear effects. At input pulse energy of $E_{in} = 3\,\mu\text{J}$, the pulse intensity evolution at different propagation distance z are shown in Figure 6.4. At this energy level, the pulse starts

breaking in both time and space domain at around $z = 50\,\mu m$ due to the nonlinear phenomenon. And the sub peaks merged together again at around $z = 125$,μm. As a result, the intensity distribution at the exit surface deviates from the original Gaussian distribution. The nonlinear effects that the pulse experienced while propagating through the material completely changed the intensity distribution of the pulse in both time and space domain.

To visualize the spatial and temporal behavior of the pulse, we plot the spatial and temporal pulse evolution along the propagation axis z in Figure 6.5 and Figure 6.6.

In Figure 6.5, the pulse breaks up in space domain around $z = 50\,\mu m$ ahead of the geometrical focus driven by nonlinear effect such as self focusing. In Figure 6.6, the pulse evolution in time domain is also quite different than the previous case. At around $z = 50\,\mu m$, the temporal profile of the pulse is also distorted and split into two peaks with the stronger peak towards the early portion of the pulse due to effects such as self phase modulation.

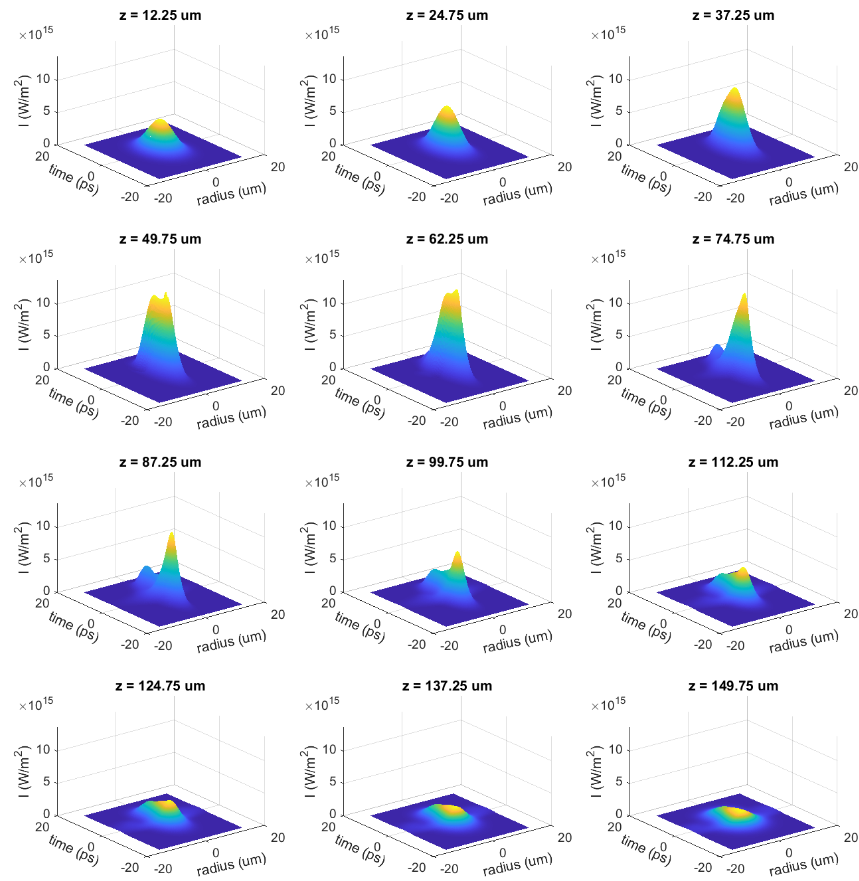


Figure 6.4: The evolution of pulse intensity profile at different propagation distance z in borosilicate glass with input pulse energy $E_{in} = 3\,\mu\text{J}$.

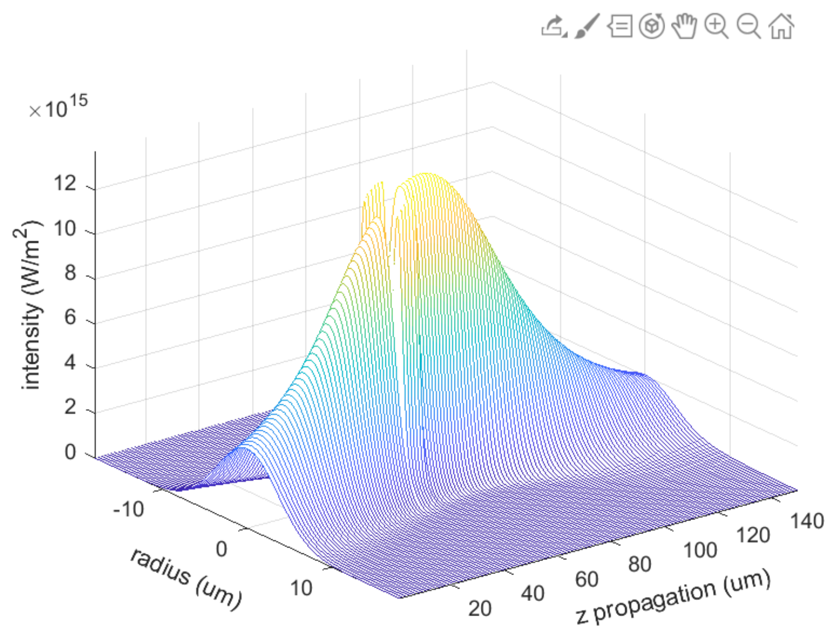


Figure 6.5: The spatial distribution of intensity along propagation axis z in borosilicate glass with pulse energy of $E_{in} = 3\,\mu\mathrm{J}$

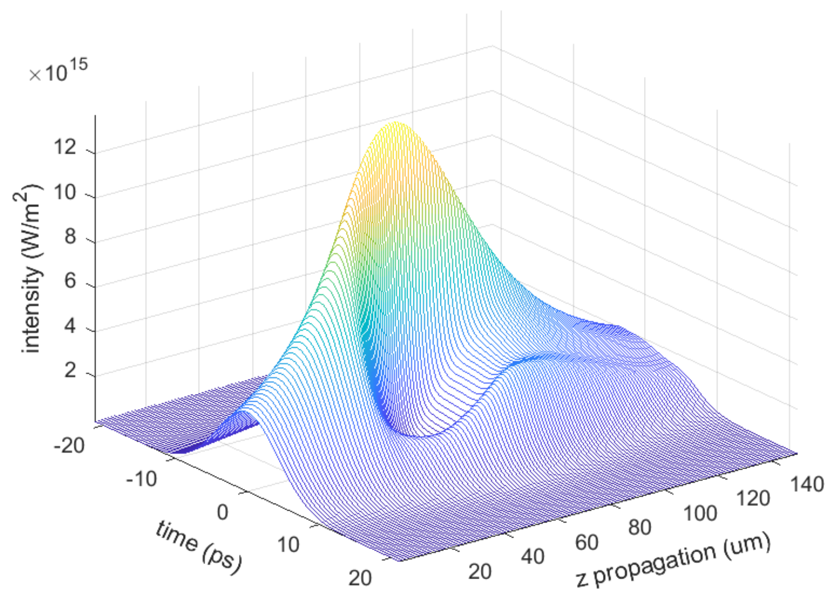


Figure 6.6: The on axis temporal distribution of intensity along propagation axis z in borosilicate glass with pulse energy of $E_{in} = 3\,\mu\text{J}$

Further increasing the pulse energy leads to even more pronounced nonlinear effects. At input pulse energy of $E_{in} = 5\,\mu\text{J}$, the pulse intensity evolution at different propagation distance z are shown in Figure 6.7. At this energy level, the pulse breaks up even earlier at around $z = 37\,\mu\text{m}$ driven by self focusing. At around $z = 150\,\mu\text{m}$, the pulse intensity is redistributed to two peaks in the time domain.

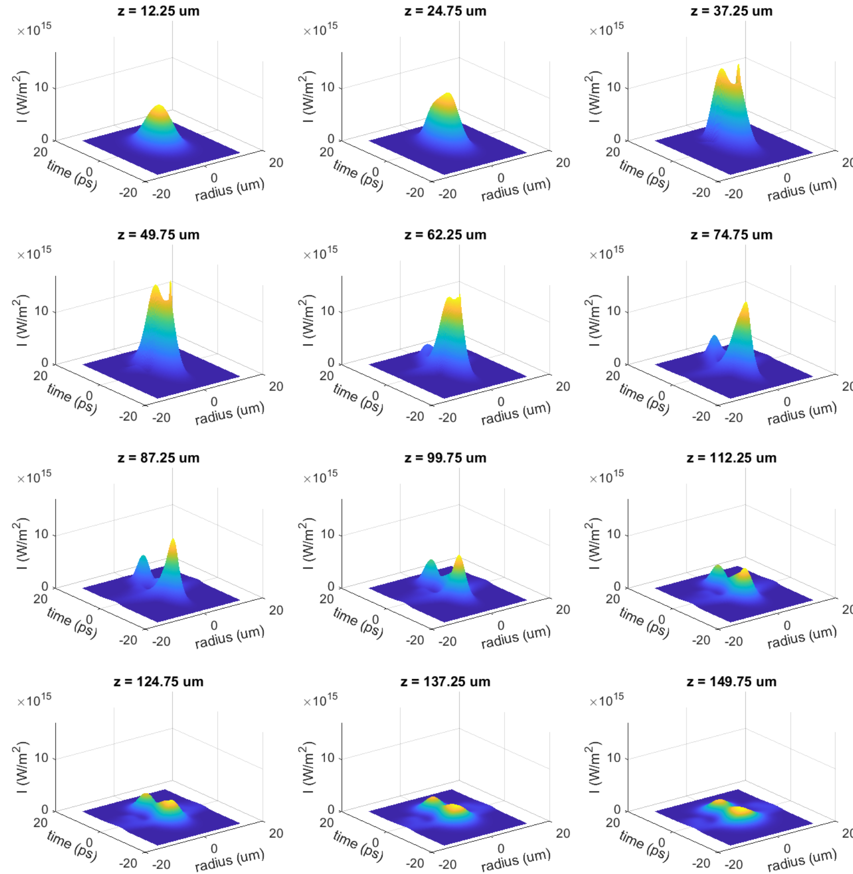


Figure 6.7: The evolution of pulse intensity profile at different propagation distance z in borosilicate glass with input pulse energy $E_{in} = 5\,\mu\text{J}$.

The spatial and temporal pulse split is even more pronounced as shown in Figure 6.8 and Figure 6.9.

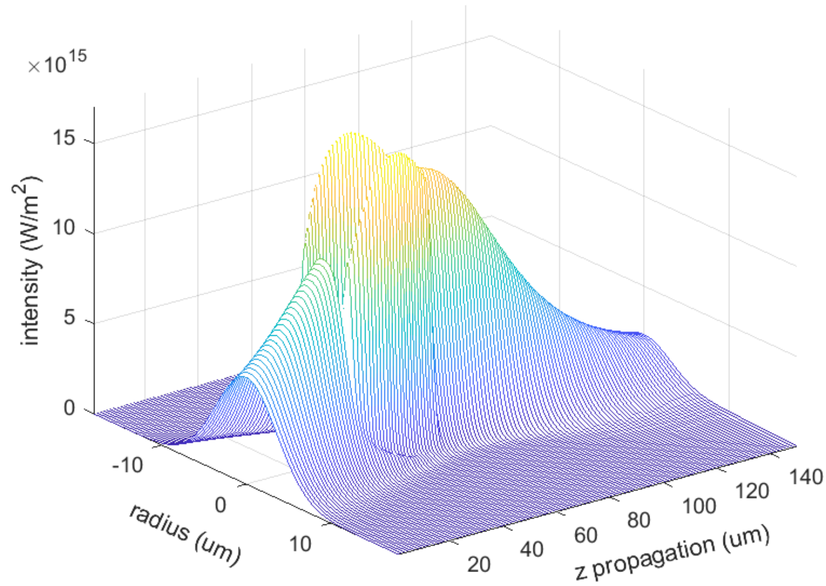


Figure 6.8: The spatial distribution of intensity along propagation axis z in borosilicate glass with pulse energy of $E_{in} = 5\,\mu J$

In Figure 6.8 and Figure 6.9, the pulse break starts at around $z = 37\,\mu m$ both spatially and temporally, and it extends to more than $z = 80\,\mu m$ spatially and $z = 150\,\mu m$ temporally. The nonlinear phenomenon completely changed the original intensity distribution of the pulse at this energy level.

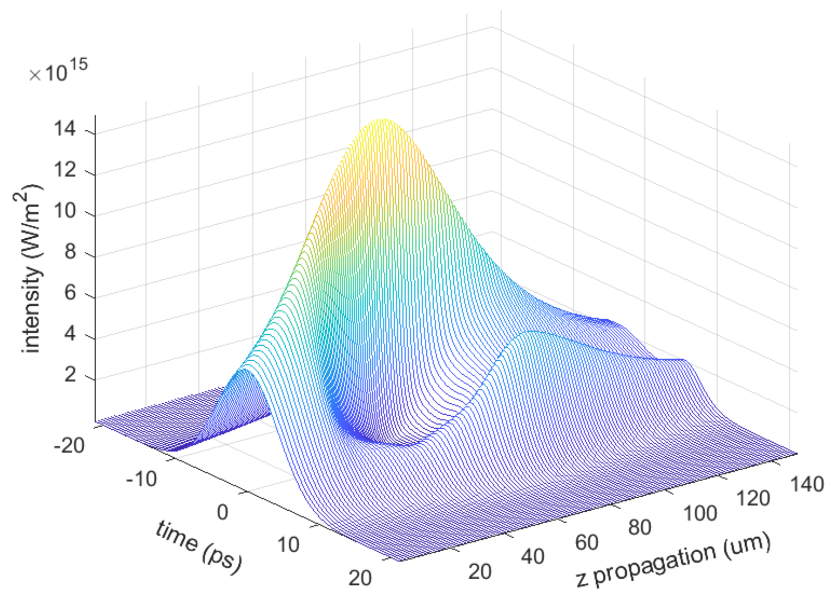


Figure 6.9: The on axis temporal distribution of intensity along propagation axis z in borosilicate glass with pulse energy of $E_{in} = 5\,\mu\mathrm{J}$

### 6.1.2 Electron dynamics

In this section, we present the electron dynamics excited by the ultrashort pulse at different input pulse energies.

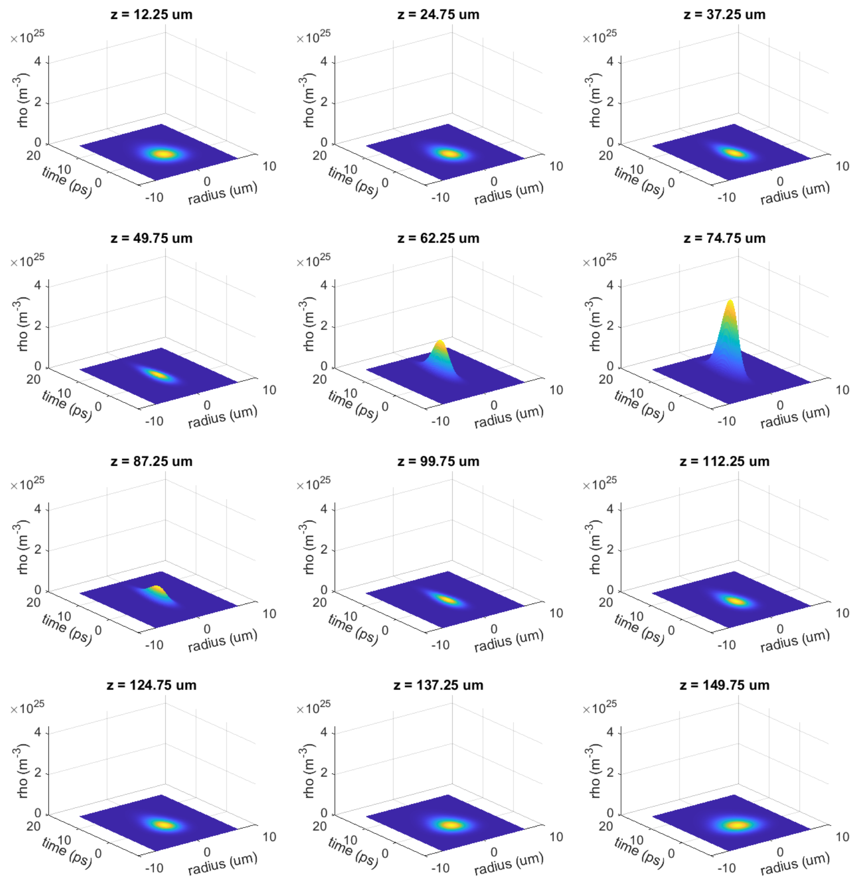


Figure 6.10: The evolution of electron density at different propagation distance z in borosilicate glass with input pulse energy $E_{in} = 1\,\mu\mathrm{J}$.

At input pulse energy of $E_{in} = 1\,\mu\mathrm{J}$, the spatial and temporal distribution of

electron density at different propagation distance z is shown in Figure 6.10. At this energy level the maximum electron density is reached at around the focus $z = 75\,\mu\text{m}$ as shown in the picture.

To visualize the on axis electron behavior, we plot the on axis electron density along the propagation axis z in Figure 6.11.

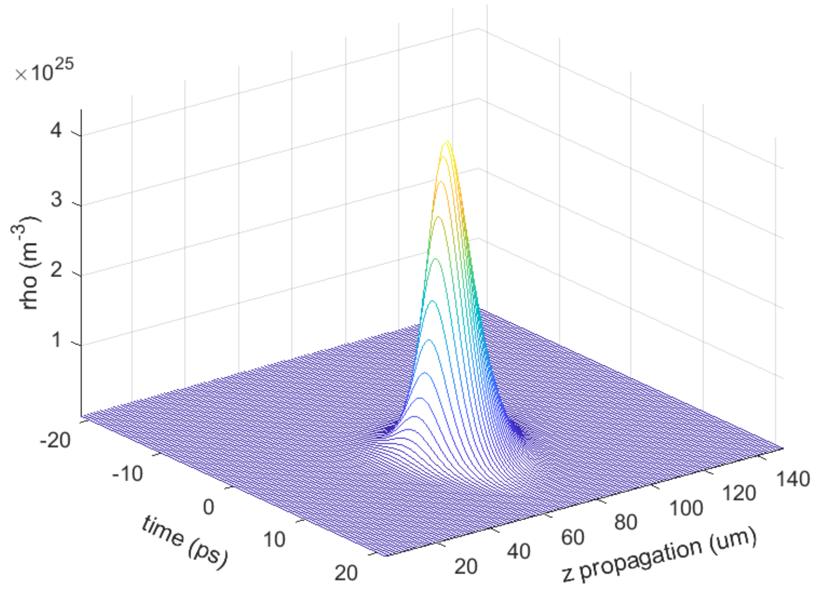


Figure 6.11: The on axis evolution of electron density at different propagation distance z in borosilicate glass with pulse energy $E_{in} = 1\,\mu\text{J}$.

As shown in Figure 6.11 the peak of the electron density is at around the focus $z = 75\,\mu\text{m}$. And the majority of the electrons are excited within 10 ps or so.

At input pulse energy of $E_{in} = 3\,\mu\text{J}$, the spatial and temporal distribution of electron density at different propagation distance z is shown in Figure 6.12. The

electron density reached $10^{25}\,\mathrm{m}^{-3}$ level at a much earlier position around $z = 37\,\mathrm{\mu m}$ and extends all the way to around $z = 87.25\,\mathrm{\mu m}$ driven by the nonlinear effects.

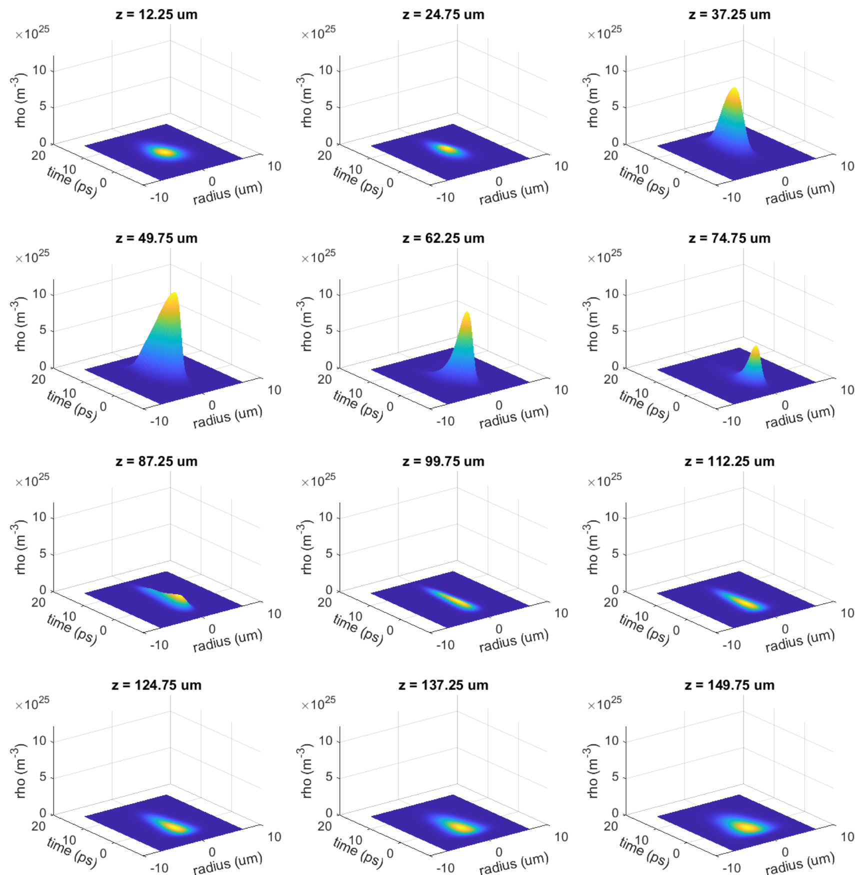


Figure 6.12: The evolution of electron density at different propagation distance z in borosilicate glass with input pulse energy $E_{in} = 3\,\mathrm{\mu J}$

To visualize the on axis electron behavior, we plot the on axis temporal profile of electron density along the propagation axis z in Figure 6.13.

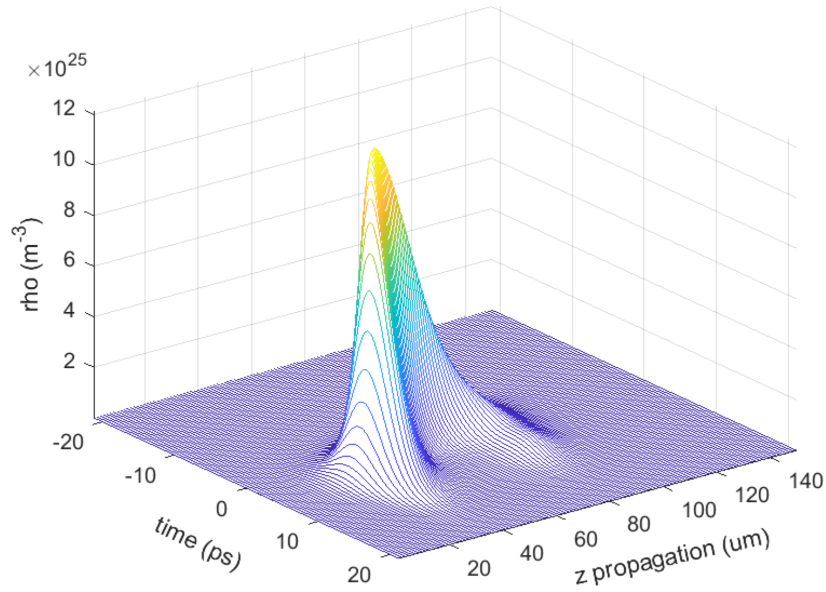


Figure 6.13: The on axis evolution of electron density at different propagation distance z in borosilicate glass with input pulse energy $E_{in} = 3\,\mu\text{J}$

In Figure 6.13, the peak of electron density is reached at around $z = 50\,\mu\text{m}$ ahead of the geometric focus. In the temporal domain, the peak of electron density shifted towards the front of the pulse while propagating. This effect can be understood as a result of the pulse intensity shifting towards the front portion as shown in Figure 6.6.

At input pulse energy of $E_{in} = 5\,\mu\text{J}$, the spatial and temporal distribution of electron density at different propagation distance z is shown in Figure 6.14. At this higher energy level, the electron density reaches level of $10^{25}\,\text{m}^{-3}$ even earlier at

around $z = 25\,\mu\mathrm{m}$ and extends even further.

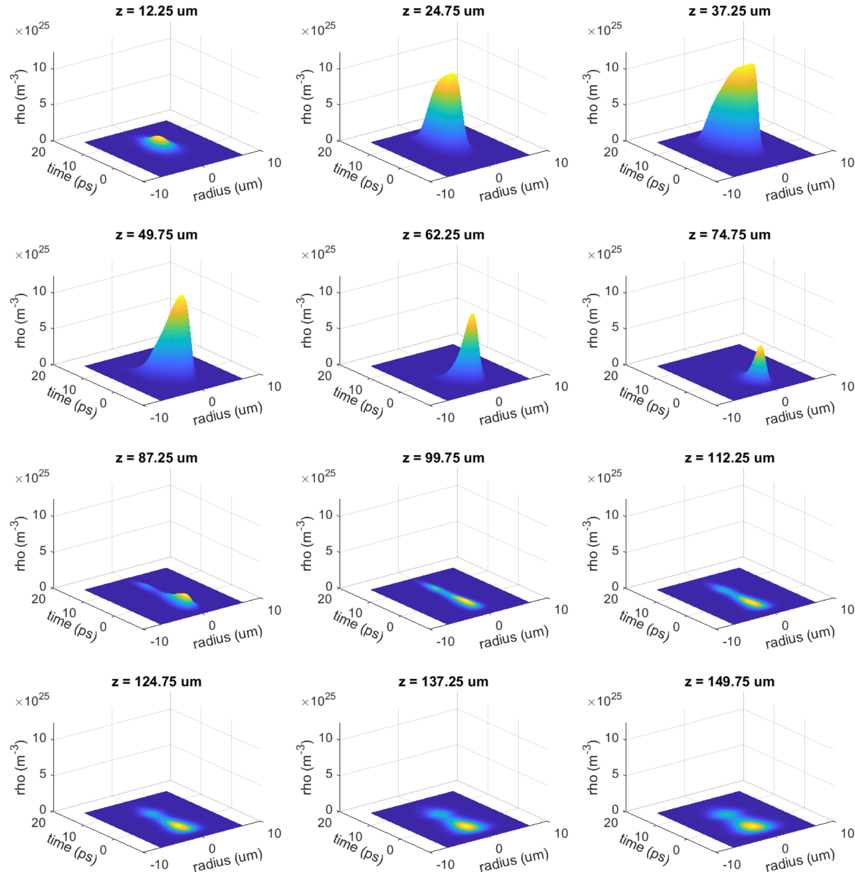


Figure 6.14: The evolution of electron density at different propagation distance z in borosilicate glass with input pulse energy $E_{in} = 5\,\mu\mathrm{J}$

To visualize the on axis electron behavior, we plot the on axis temporal profile of electron density along the propagation axis z in Figure 6.15.

As shown in Figure 6.15, the higher pulse energy drives the electron density to

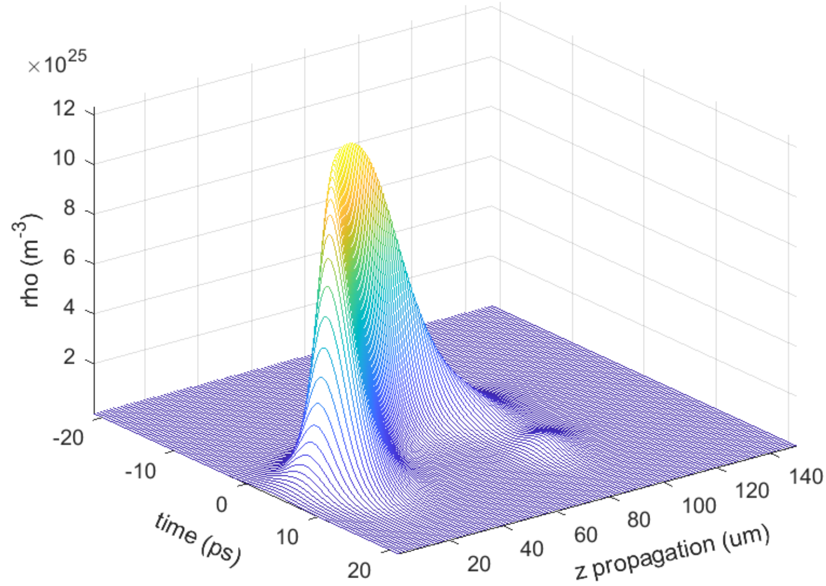


Figure 6.15: The on axis evolution of electron density at different propagation distance z in borosilicate glass with input pulse energy $E_{in} = 5\,\mu J$

extend a longer distance in the z direction and shifts toward the front portion of the pulse while propagating.

### 6.1.3 Matching modification track with electron contour

The simulation results of beam propagation and electron density at input pulse energies of $E_{in} = 1\,\mu J$, $E_{in} = 3\,\mu J$, and $E_{in} = 5\,\mu J$ are shown in Figure 6.16(a), Figure 6.16(b), Figure 6.16(c) respectively. The laser pulse is launched from the left hand side to the right hand side and the geometric focus is marked around the vertical dashed line in the picture. At an input pulse energy of $1\,\mu J$, the material

modification is barely visible and it happens around the geometric focal position. At input pulse energy of 3 µJ, the modification track becomes obvious with smooth inner dark core and outer boundary. The inner dark core matchs very well with electron density distribution at level of $\rho_{max} = 10^{20}\,\mathrm{cm}^{-3}$ indicated by the dashed contour shown in Figure 6.16(b). The position of the modification track shifted towards the incoming laser beam and the beam started experiencing self-focusing at this energy level. Further increasing the input pulse energy to 5 µJ generates a longer modification track with hollow beaded structure in the center along the propagation axis. The shape and length of the inner modification track are matched very well with electron density distribution at a level of $\rho_{max} = 10^{20}\,\mathrm{cm}^{-3}$ with features like the leading hollow bead structure matching the beginning portion of the electron contour and the thin tail of the modification track matching the tail of the electron contour shown in Figure 6.16(c). The peak power of the pulse with an input pulse energy of 5 µJ is $P_{peak} = 0.5\,\mathrm{MW}$, which is about 7 times less than critical power $P_{cr} = 3.5\,\mathrm{MW}$ for self-focusing in borosilicate glass. However, the beam still experienced self-focusing and plasma de-focusing as shown in the simulation results in Figure 6.16(c), which indicates that the Kerr self focusing term in equation 5.17 should not be neglected. Our simulation and experimental data are best fitted when the multiphoton ionization cross section $\sigma_4 = 4 \times 10^{-41}\,(\mathrm{cm}^2/\mathrm{W})^4$ and the avalanche ionization coefficient $\eta = \sigma/U_i = 1.63\,\mathrm{cm}^2/\mathrm{J}$.

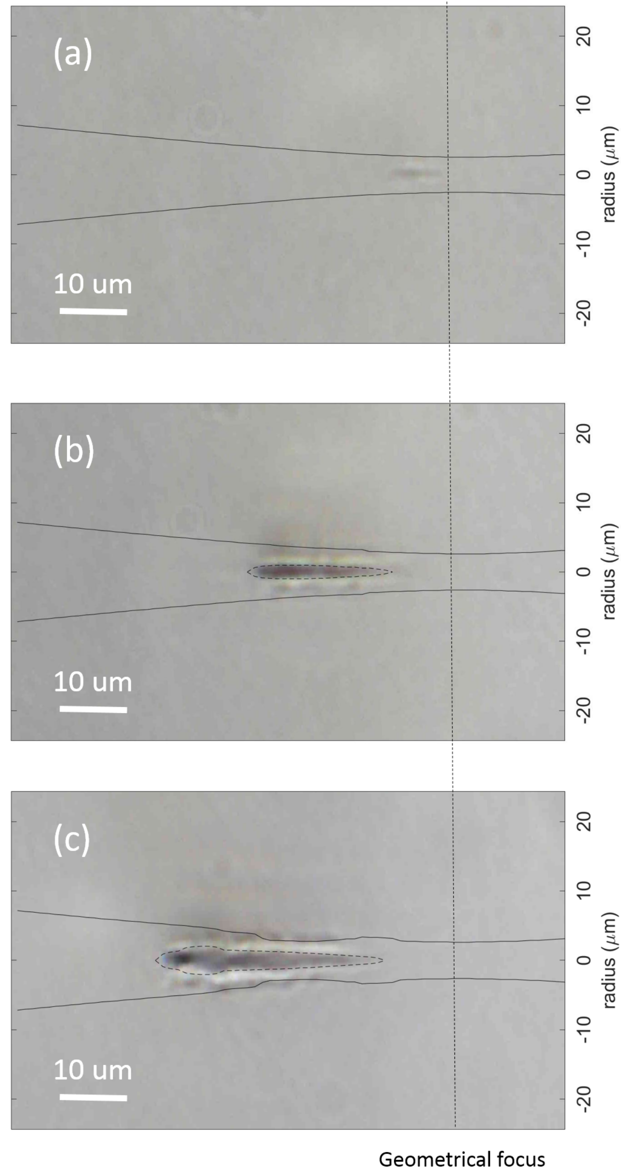


Figure 6.16: Simulation results of beam propagation and electron density overlaid on the experimental results. The input pulse energy are (a) 1 µJ, (b) 3 µJ, (c) 5 µJ. The solid line indicates the beam radius at $1/e^2$ intensity level. The dashed contour indicates the max electron density at a level of $\rho_{max} = 10^{20}\,\mathrm{cm}^{-3}$, and the vertical dash line indicates the position of the geometric focus.

### 6.1.4 Role of MPI and avalanche ionization

The relative role of electron contribution from multiphoton ionization and avalanche ionization are shown in Figure 6.17.

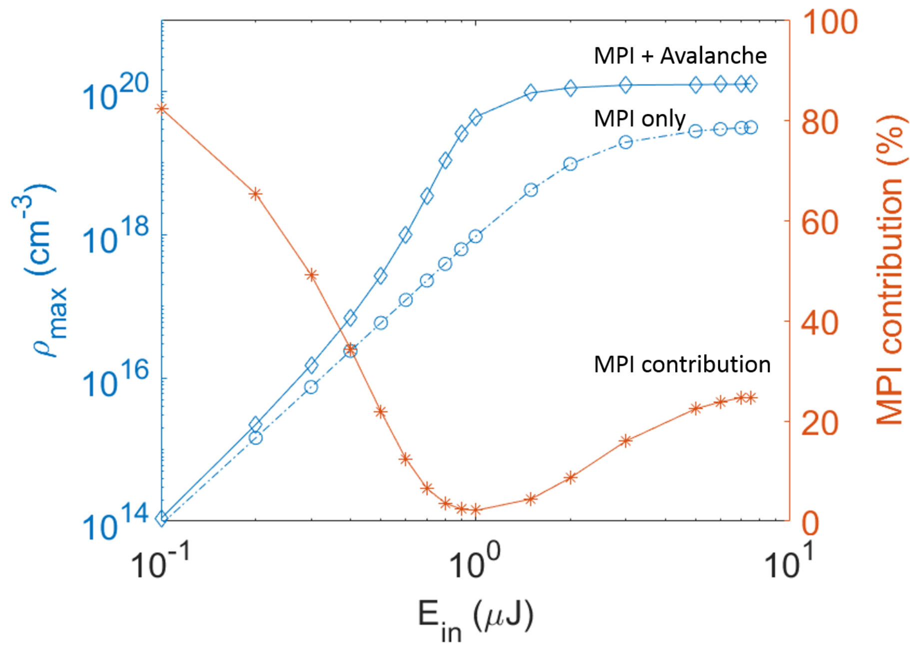


Figure 6.17: Simulation results of electron density vs input pulse energy in borosilicate glass. The maximum electron density is indicated by the left hand side y axis. The diamond solid line shows electron generation from multiphoton ionization and avalanche ionization. The circle dashed line shows electron generation from multiphoton ionization only. The percentage of electron contribution from multiphoton ionization is indicated by the right hand side y axis, and plotted as starred solid line in the graph. MPI: multiphoton ionization

The maximum electron density clamps at around $10^{20}\,\mathrm{cm}^{-3}$ when the input pulse energy approaches 2 µJ, similar electron clamping density has been found in other studies as well[51, 9]. At this energy level and above, the modification track has a

distinct dark inner core as shown in Figure 4.2(b), 4.2(c), 4.2(d), corresponding to input pulse energy of 2 µJ, 3 µJ ,5 µJ respectively. At low energy level $E_{in} < 0.2\,\mu J$, multiphoton ionization is the major channel for electron generation with more than 60% of the electrons being generated by the multiphoton ionization process. When increasing the pulse energy, the electron contribution from multiphoton ionization decreases while the contribution from avalanche ionization increases. At energy levels of about $E_{in} = 1\,\mu J$, the role of avalanche ionization becomes dominant with more than 98% of electron contribution, while multiphoton ionization provides about 2% of the electrons. At energy level $E_{in} > 1\,\mu J$, the percentage of electron generation from multiphoton ionization increases but the avalanche ionization still remains the major effect with more than 75% of electron contribution.

## 6.2 Fused silica

Fused silica is another important material that has wide applications in lasers, fibers, and lenses. It is one of the basic building blocks in modern industry. Because of its strategic importance, it has been actively studied in the optics and laser communities and ultrashort pulse interaction with fused silica is still an active research topic.

### 6.2.1 Pulse behavior

In this section we present the pulse propagation behavior in a bulk of fused silica glass for different input pulse energies.

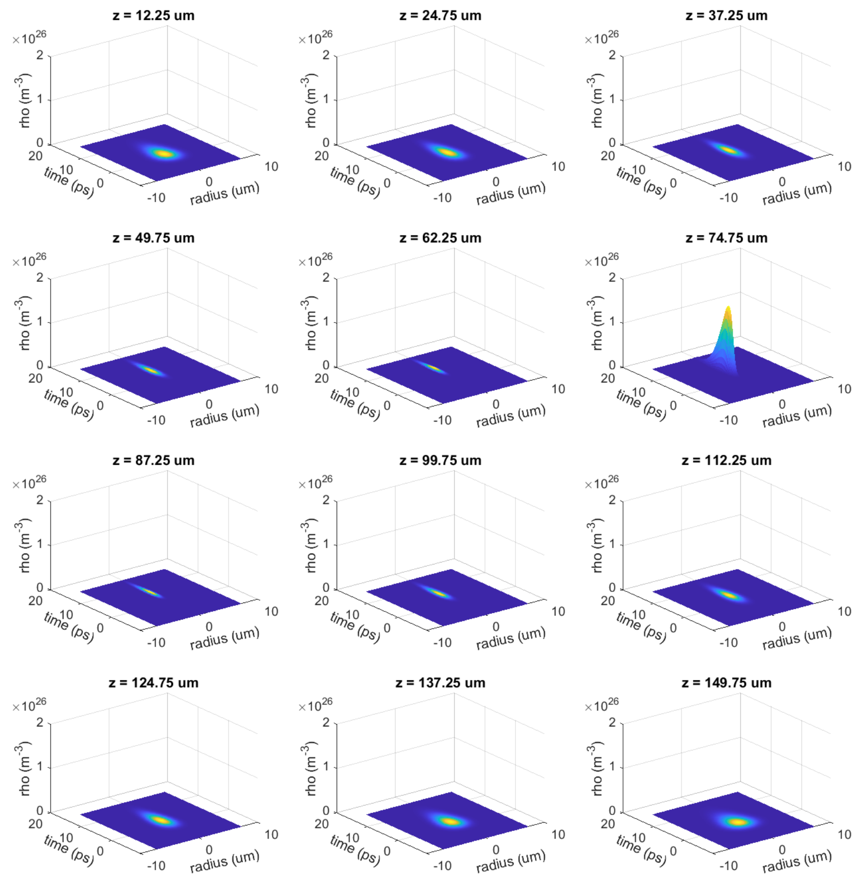


Figure 6.18: The evolution of pulse intensity profile at different propagation distance z in fused silica with input pulse energy $E_{in} = 1.5\,\mu\text{J}$.

At a low pulse energy level $E_{in} = 1.5\,\mu\text{J}$, the pulse propagates smoothly without

nonlinear disturbance as shown in Figure 6.18. The maximum intensity is reached at around the focus at this energy level.

To visualize the spatial and temporal behavior of the pulse, we plot the spatial and temporal pulse evolution along the propagation axis z in Figure 6.19 and Figure 6.20.

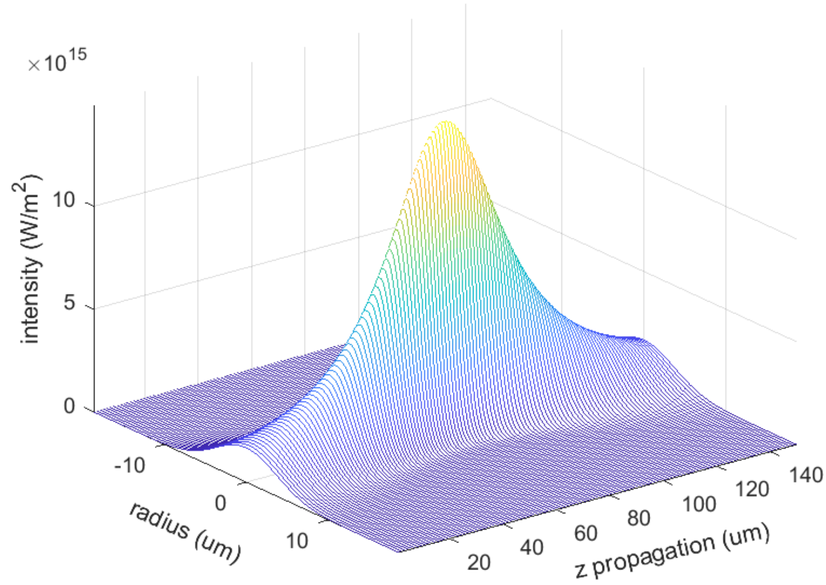


Figure 6.19: The spatial distribution of intensity along propagation axis z in fused silica with pulse energy of $E_{in} = 1.5\,\mu\text{J}$.

In Figure 6.19, the pulse is focused through the focal position without significant nonlinear disturbance and the maximum intensity is reached at around the focal position $z = 75\,\mu\text{m}$.

In Figure 6.20, the temporal pulse shape shortened around the focus indicating

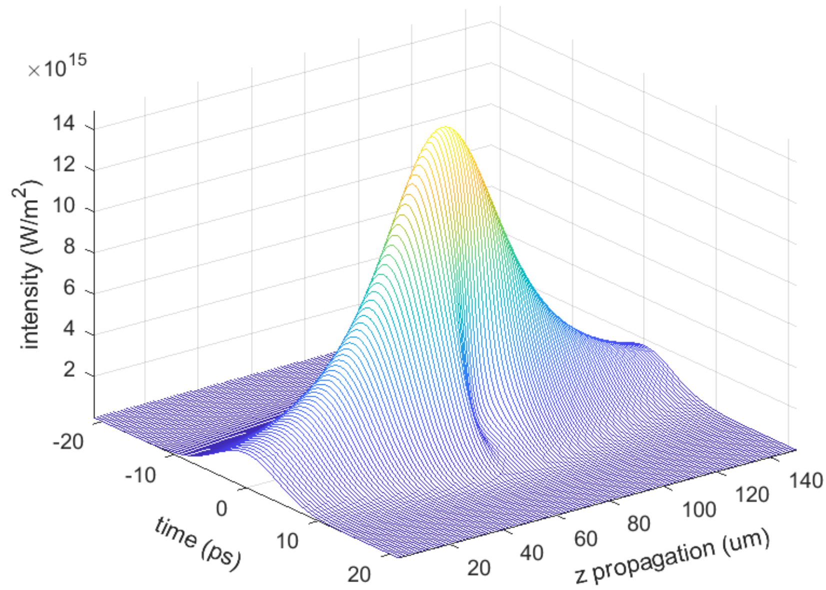


Figure 6.20: The on axis temporal distribution of intensity along propagation axis z in fused silica with pulse energy of $E_{in} = 1.5\,\mu\text{J}$.

the pulse started experiencing nonlinear effects such as self phase modulations at this location.

At an input pulse energy of $E_{in} = 3\,\mu\text{J}$, the pulse intensity evolution at different propagation distance z are shown in Figure 6.21. At this energy level, the pulse breaks up at around $z = 50\,\mu\text{m}$ driven by self focusing and self phase modulations. And the pulse intensity is redistributed at the exit.

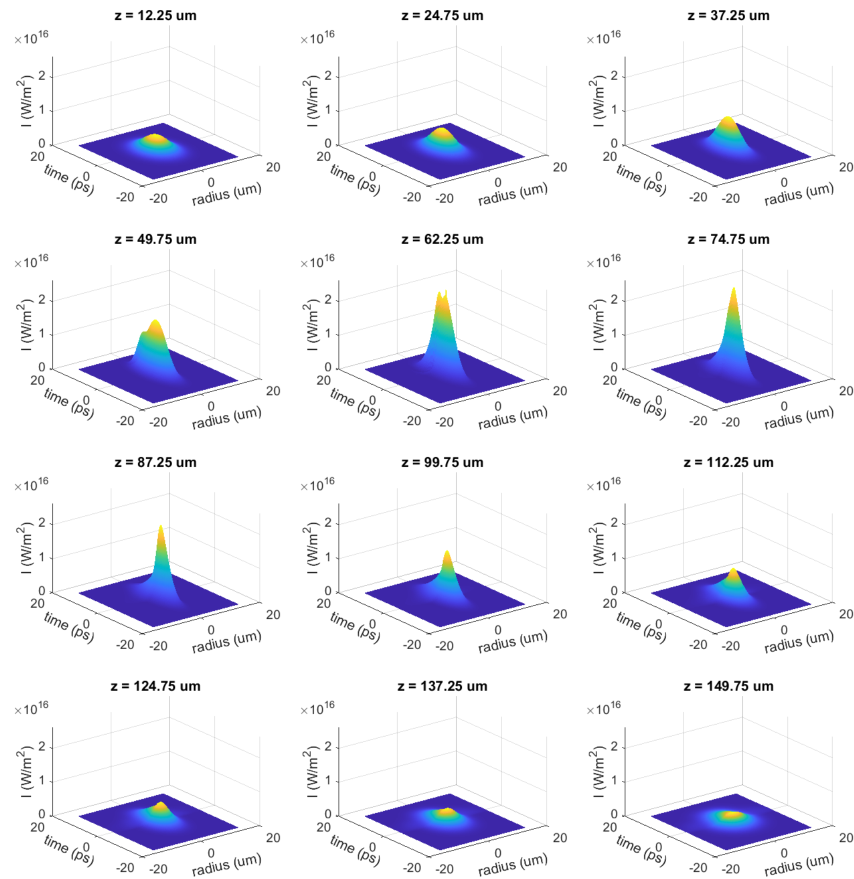


Figure 6.21: The evolution of pulse intensity profile at different propagation distance z in fused silica with input pulse energy $E_{in} = 3\,\mu\mathrm{J}$.

To visualize the spatial and temporal behavior of the pulse, we plot the spatial and temporal pulse evolution along the propagation axis z in Figure 6.22 and Figure 6.23.

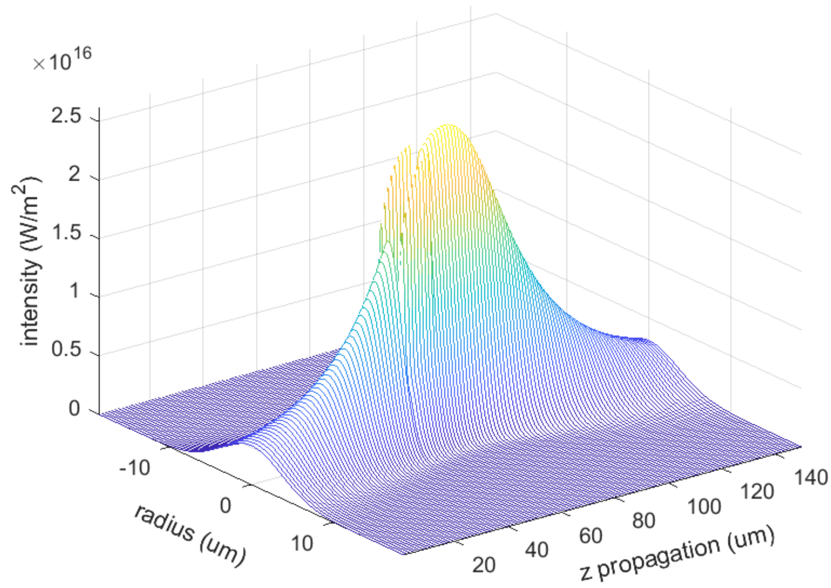


Figure 6.22: The spatial distribution of intensity along propagation axis z in fused silica with pulse energy of $E_{in} = 3\,\mu\text{J}$.

In Figure 6.22 and Figure 6.23, the pulse break up starts at around $z = 50\,\mu\text{m}$ both spatially and temporally and it extends to around $z = 80\,\mu\text{m}$ driven by nonlinear effects that the pulse experienced.

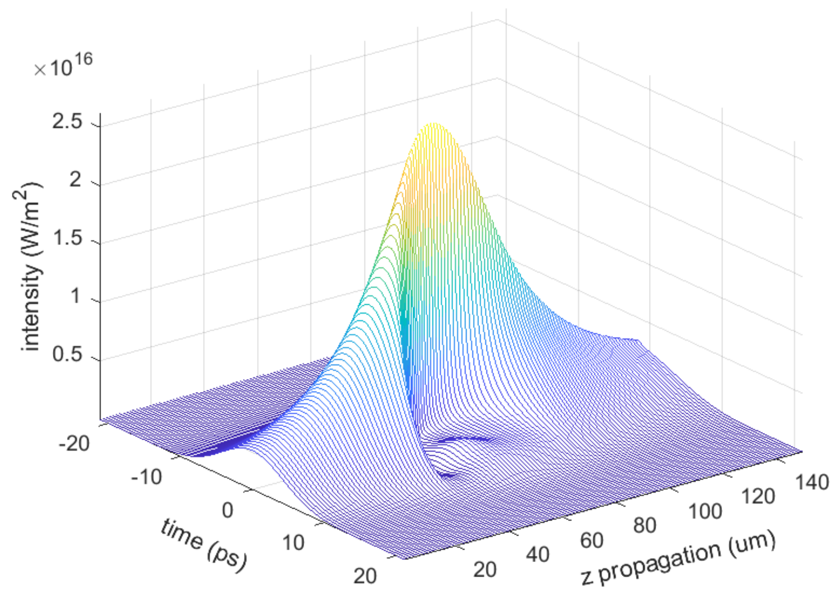


Figure 6.23: The on axis temporal distribution of intensity along propagation axis z in fused silica with pulse energy of $E_{in} = 3\,\mu\mathrm{J}$.

### 6.2.2 Electron dynamics

In this section, we present the electron dynamics excited by the ultrashort pulses at different input pulse energies in fused silica.

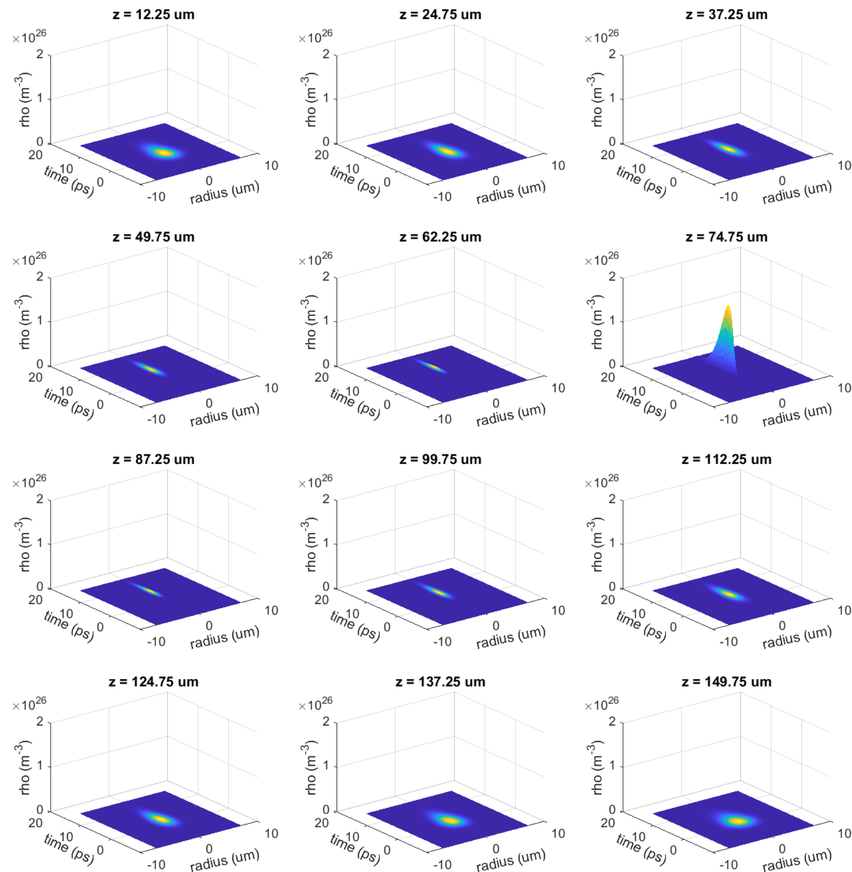


Figure 6.24: The evolution of electron density at different propagation distance z in fused silica with input pulse energy $E_{in} = 1.5\,\mu\text{J}$.

At input pulse energy of $E_{in} = 1.5\,\mu\text{J}$, the spatial and temporal distributions of

electron density at different propagation distances, z, are shown in Figure 6.24. At this energy level the maximum electron density is reached at around $z = 75\,\mu\text{m}$ as shown in the picture.

To visualize the on axis electron behavior, we plot the on axis electron density along the propagation axis z in Figure 6.25.

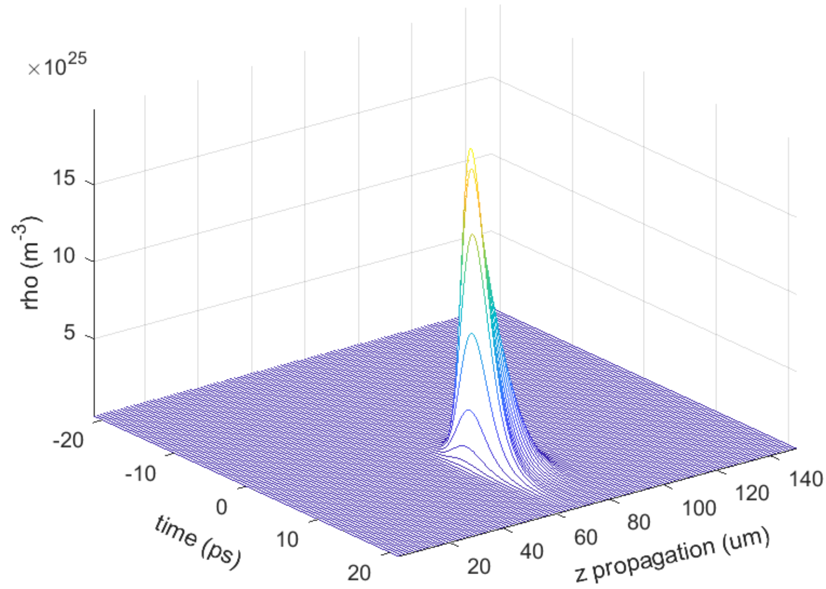


Figure 6.25: The on axis evolution of electron density at different propagation distance z in fused silica with input pulse energy $E_{in} = 1.5\,\mu\text{J}$.

As shown in Figure 6.25 the peak of the electron density is reached at around the focus $z = 75\,\mu\text{m}$. And the majority of the electrons are excited within 10 ps or so.

At a higher input pulse energy of $E_{in} = 3\,\mu\text{J}$, the spatial and temporal distributions of electron density at different propagation distances, z, are shown in Figure 6.26. The electron density reached $10^{26}\,\text{m}^{-3}$ level at a much earlier position around $z = 50\,\mu\text{m}$ and extends all the way to around $z = 87.25\,\mu\text{m}$ driven by the nonlinear effects.

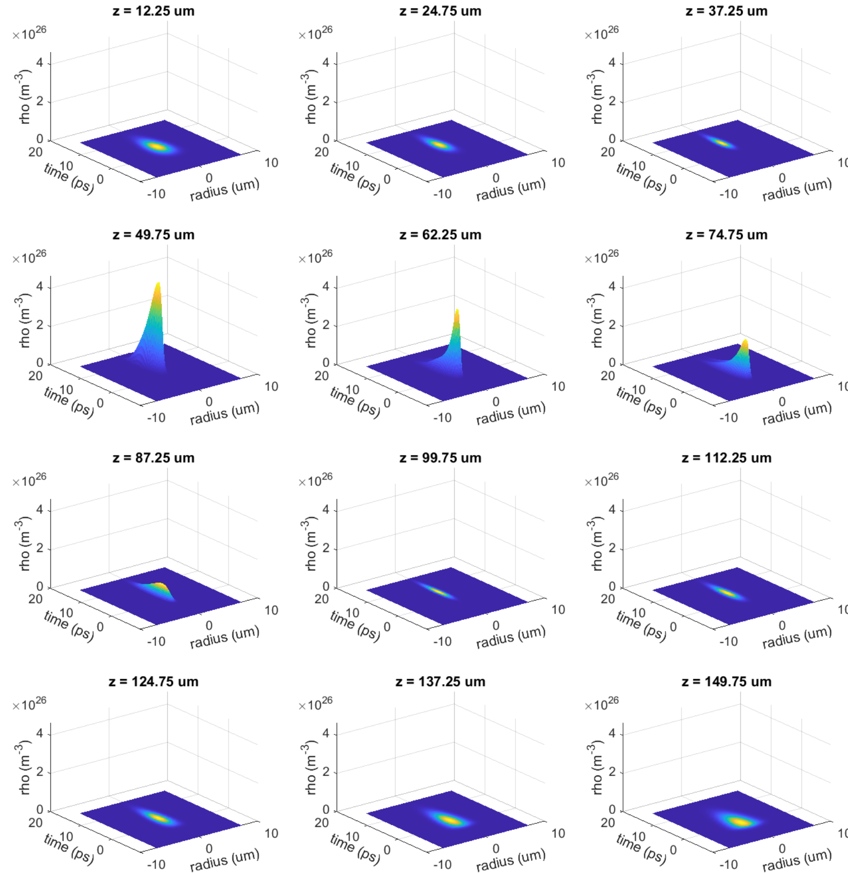


Figure 6.26: The evolution of electron density at different propagation distance z in fused silica with input pulse energy $E_{in} = 3\,\mu\text{J}$.

To visualize the on axis electron behavior, we plot the on axis temporal profile of electron density along the propagation axis z in Figure 6.27.

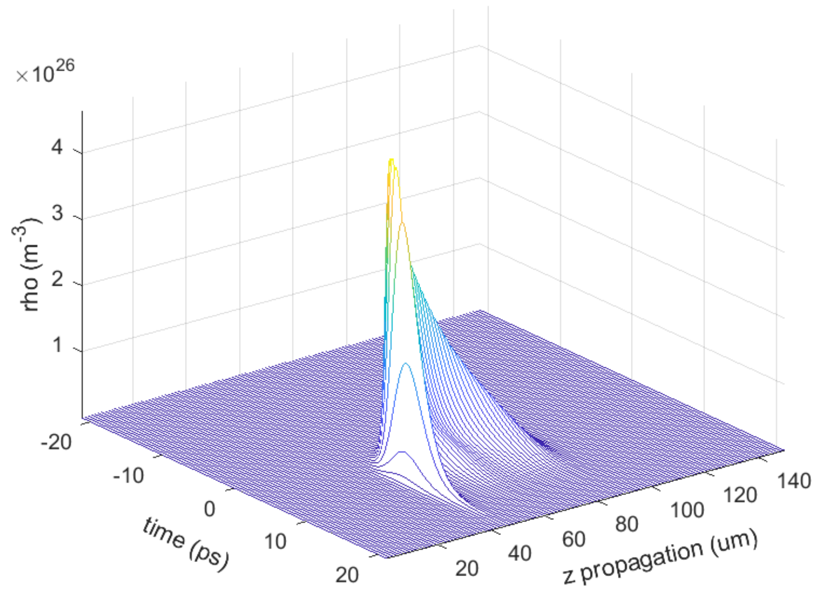


Figure 6.27: The on axis evolution of electron density at different propagation distance z in fused silica with input pulse energy $E_{in} = 3\,\mu\text{J}$.

In Figure 6.27, the peak of electron density is reached at around $z = 50\,\mu\text{m}$ ahead of the geometric focus. In the temporal domain, the peak of electron density shifted towards the front of the pulse while propagating. This effect can be understood as a result of the pulse intensity shifting towards the front portion as shown in Figure 6.23.

### 6.2.3 Matching modification track with electron contour

To compare the simulation results with experiments, we plot the pulse propagation and electron density at input pulse energy of $E_{in} = 1.5\,\mu\text{J}$, $E_{in} = 2.5\,\mu\text{J}$,and $E_{in} = 3\,\mu\text{J}$ in Figure 6.28(a), Figure 6.28(b), and Figure 6.28(c) respectively. The laser pulse is launched from the left hand side to the right hand side and the geometric focus is marked around the vertical dashed line in the picture. At input pulse energy of $1.5\,\mu\text{J}$, the material modification is just visible and it happens around the geometric focal position. At input pulse energy of $2.5\,\mu\text{J}$, the modification track becomes obvious with inner dark core and outer shallow modified region. The inner dark core matches very well with electron density distribution at level of $\rho_{max} = 10^{20}\,\text{cm}^{-3}$ indicated by the dashed contour shown in Figure 6.28(b). The position of the modification track shifted towards the incoming laser beam and the beam started experiencing self-focusing at this energy level. Further increasing the input pulse energy to $3\,\mu\text{J}$ generates a longer modification track with a crack-like feature at the front of the modified region. The general shape and length of the inner modified region are matched very well with electron density distribution at level of $\rho_{max} = 10^{20}\,\text{cm}^{-3}$. Our simulation and experimental data are best fitted when the multiphoton ionization cross section $\sigma_8 = 5 \times 10^{-96}\,(\text{cm}^2/\text{W})^8$ and the avalanche ionization coefficient $\eta = \sigma/U_i = 2.6\,\text{cm}^2/\text{J}$.

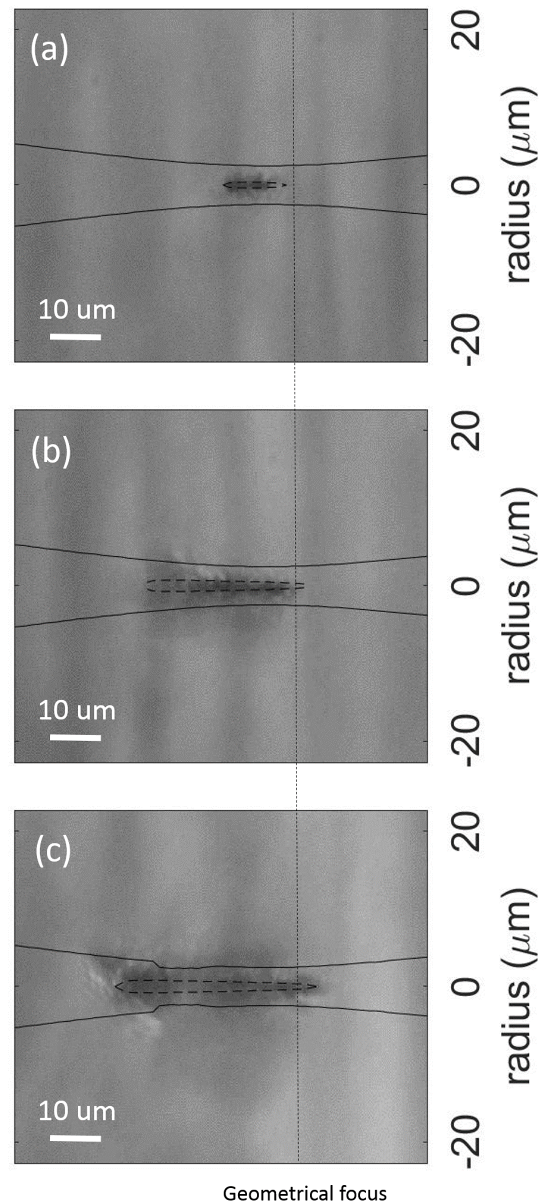


Figure 6.28: Simulation results of beam propagation and electron density overlaid on the experimental results in fused silica. The input pulse energies are (a) 1.5 µJ, (b) 2.5 µJ, (c) 3 µJ. The solid line indicates the beam radius at $1/e^2$ intensify level. The dashed contour indicates the max electron density at level of $\rho_{max} = 10^{20}\,\mathrm{cm}^{-3}$, and the vertical dash line indicates the position of the geometric focus.

### 6.2.4 Role of MPI and avalanche ionization

The relative roles of electron contribution from multiphoton ionization and avalanche ionization are shown in Figure 6.29. The maximum electron density clamps at around $10^{20}\,\mathrm{cm}^{-3}$ when input pulse energy approach 1.2 µJ, similar electron clamping density has been found in other studies as well[51, 9]. At this energy level and above, the modification track has a distinct dark inner core as shown in Figure 4.3(b), Figure 4.3(c), Figure 4.3(d), corresponding to input pulse energies of 2 µJ, 2.5 µJ, 3 µJ respectively. At low energy levels $E_{in} < 0.2\,\mu\mathrm{J}$, multiphoton ionization is the major channel for electron generation with more than 50% of the electrons being generated by the multiphoton ionization process. When increasing the pulse energy, the electron contribution from multiphoton ionization decreases while the contribution from avalanche ionization increases. At energy level of about $E_{in} = 1\,\mu\mathrm{J}$, the role of avalanche ionization becomes dominant with more than 99% of electron contribution, while multiphoton ionization provides about 1% of the electrons. At energy level $E_{in} > 1\,\mu\mathrm{J}$, the percentage of electron generation from multiphoton ionization decreases even further and avalanche effect become the major effect of electron contributions.

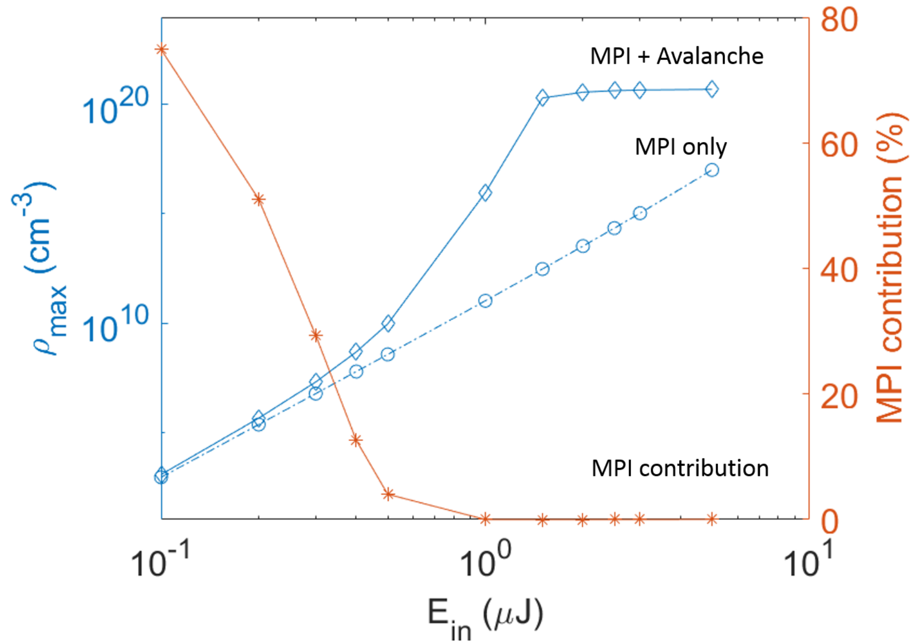


Figure 6.29: Simulation results of electron density vs input pulse energy in fused silica. The maximum electron density is indicated by the left hand side y axis. The diamond solid line shows electron generation from multiphoton ionization and avalanche ionization. The circle dashed line shows electron generation from multiphoton ionization only. The percentage of electron contribution from multiphoton ionization is indicated by the right hand side y axis, and plotted as starred solid line in the graph.

## 6.3 Fused silica interacting with femtosecond pulse

In this section, we extend our simulation from picosecond pulse to femtosecond pulse. Specifically, we simulate an industry available femtosecond laser pulse with pulse duration of 500 fs at wavelength of 1064 nm in fused silica.

### 6.3.1 Pulse behavior

Under the same settings, we simulate a femtosecond pulse with $E_{in} = 1\,\mu J$. The pulse dynamics at different propagation distance z is shown in Figure 6.30. Due to the high peak power compared to picosecond pulses, the beam breaks up around $z = 50\,\mu m$ and also the maximum intensity is reached at this location ahead of the geometric focus.

To visualize the spatial and temporal behavior of the pulse, we plot the spatial and temporal pulse evolution along the propagation axis z in Figure 6.31 and Figure 6.32.

In Figure 6.31 and 6.32, we clearly see the pulse breaks up at around $z = 50\,\mu m$ spatially and temporally. And the intensity of the pulse shifted toward the front of the pulse while propagating. This is due to the much higher peak power of the femtosecond laser pulse, at $E_{in} = 1\,\mu J$, the peak power for a 500 fs pulse is $P_{peak} = 2\,MW$, while the peak power for a 10 ps pulse is only 0.1 MW.

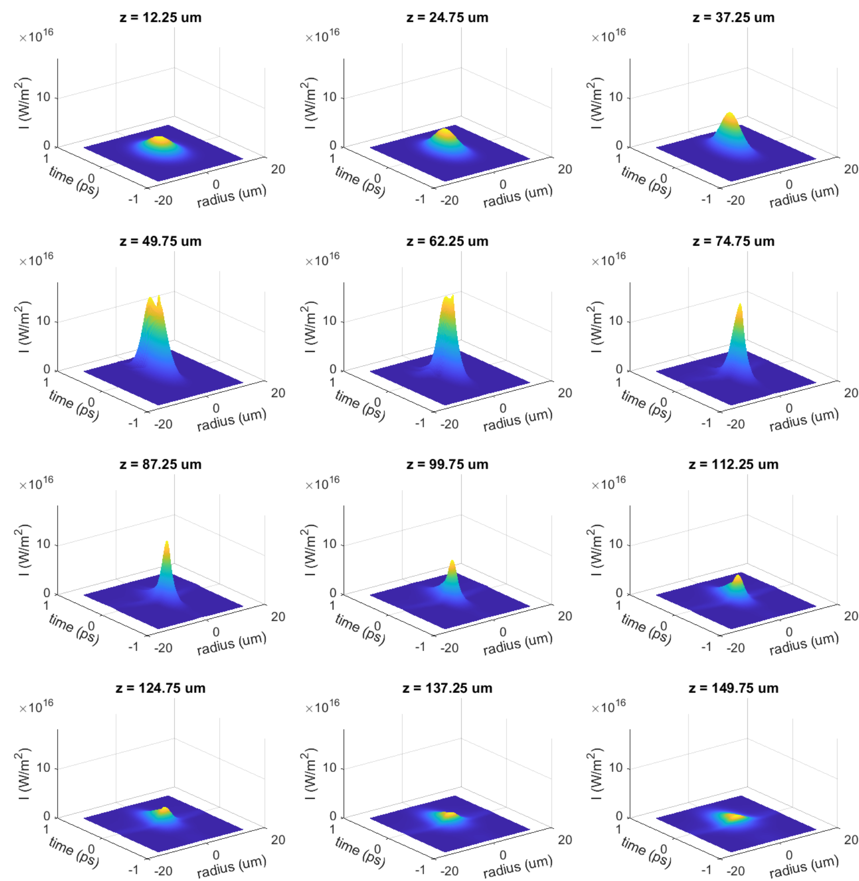


Figure 6.30: The evolution of pulse intensity profile at different propagation distance z in fused silica with input pulse energy $E_{in} = 1\,\mu\text{J}$ and pulse duration 500 fs.

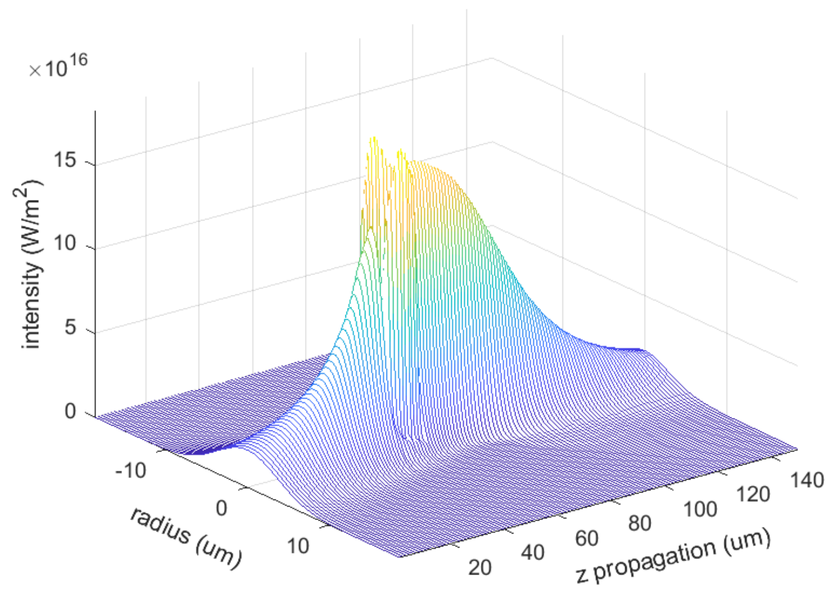


Figure 6.31: The spatial distribution of intensity along propagation axis z in fused silica with pulse energy of $E_{in} = 1\,\mu\text{J}$ and pulse duration $500\,\text{fs}$.

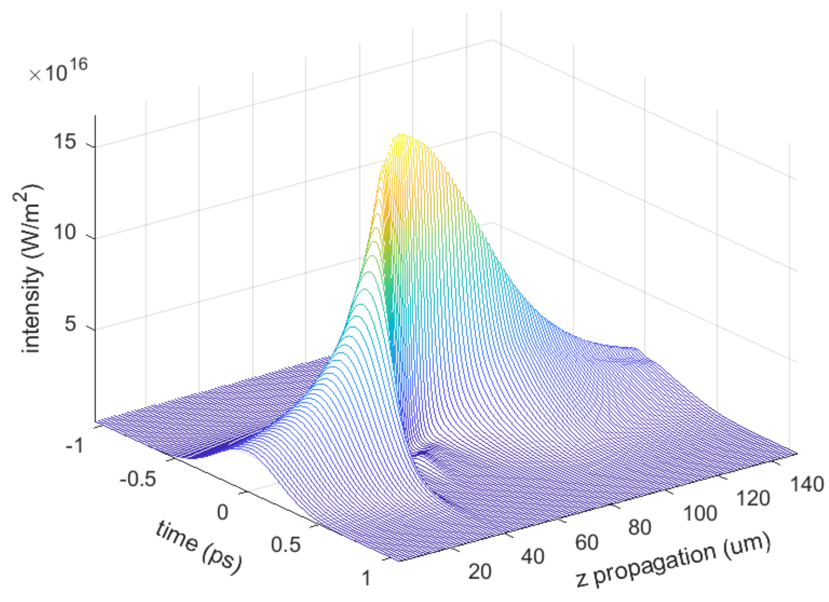


Figure 6.32: The on axis temporal distribution of intensity along propagation axis z in fused silica with pulse energy of $E_{in} = 1\,\mu\text{J}$ and pulse duration $500\,\text{fs}$.

### 6.3.2 Electron dynamics

Under the excitation of the femtosecond pulse at $E_{in} = 1\,\mu\text{J}$, the electrons of the material swiftly excited as shown in Figure 6.33.

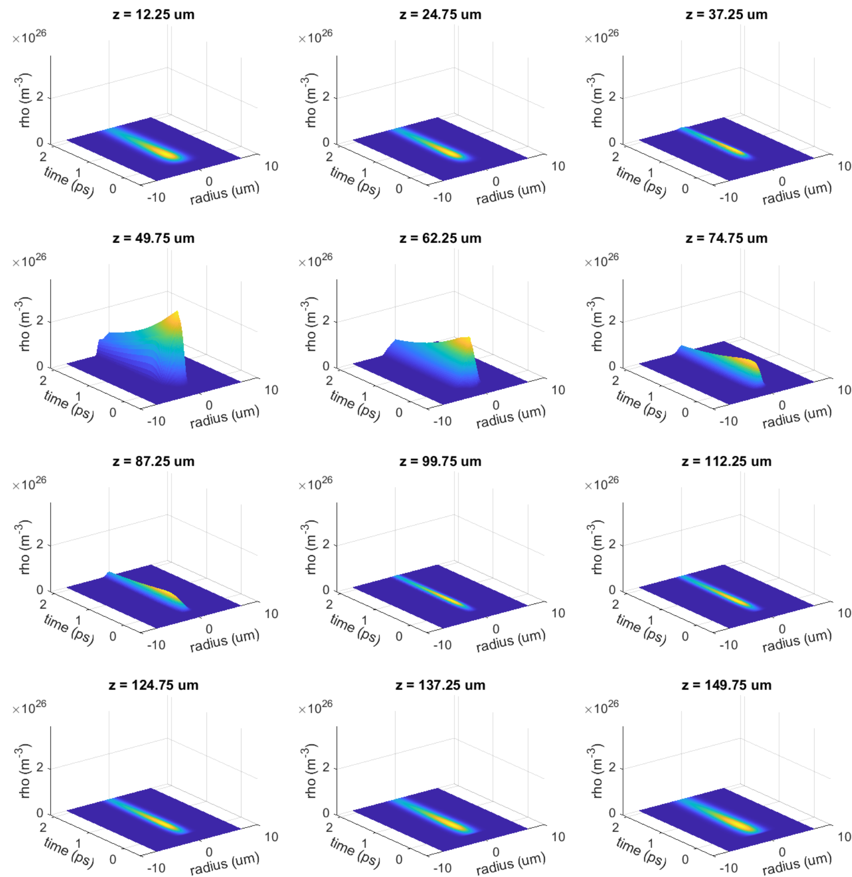


Figure 6.33: The evolution of electron density at different propagation distance z in fused silica with input pulse energy $E_{in} = 1\,\mu\text{J}$ and pulse duration 500 fs.

The maximum electron density is reached at around $z = 50\,\mu\text{m}$ where the pulse

intensity is the max. More interestingly, under the femtosecond pulse excitation, the electrons are living longer than the pulse duration. In another word, the electrons are still there after the pulse is gone. This leads to the complete decouple of energy deposition and electron energy relaxation to the lattice.

To visualize the on axis electron behavior, we plot the on axis electron density along the propagation axis z in Figure 6.34.

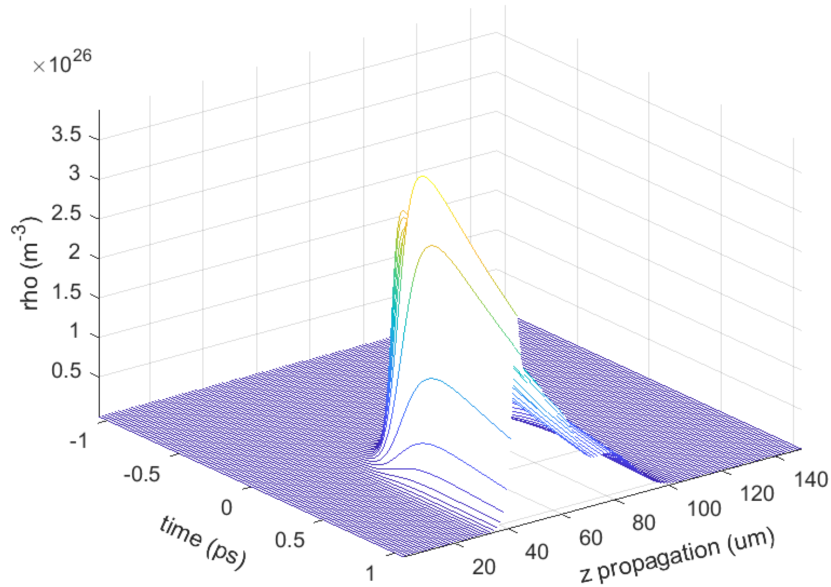


Figure 6.34: The on axis evolution of electron density at different propagation distance z in fused silica with input pulse energy $E_{in} = 1\,\mu J$ and pulse duration 500 fs.

As shown in Figure 6.34 the peak of the electron density is at around $z = 50\,\mu m$. And the electrons live up to a few ps longer after the pulse is gone. In the femtosecond case, the electron density reaches the maximum swiftly as shown in

Figure 6.34 and the peak shifts toward the pulse front while propagating.

### 6.3.3 Role of MPI and avalanche ionization

The relative role of electron contribution from multiphoton ionization and avalanche ionization in the femtosecond pulse case are numerically studied as shown in Figure 6.35. The maximum electron density clamps at around $10^{20}\,\mathrm{cm}^{-3}$ when input pulse energy approach 0.4 µJ, similar electron density clamping has been found in other studies as well[51, 9]. When pulse energy is less than 0.2 µJ, the electron contribution from multiphoton ionization decreases when increasing the pulse energy. At around $E_{in} = 0.2\,\mu\mathrm{J}$, multiphoton ionization reaches a minimum contribution of around 2%. Further increasing the pulse energy will lead to an increased contribution from multiphoton ionizaiton to around 20% at pulse energy of 1 µJ. For all the energy levels we studied numerically, the avalanche ionization plays an important role.

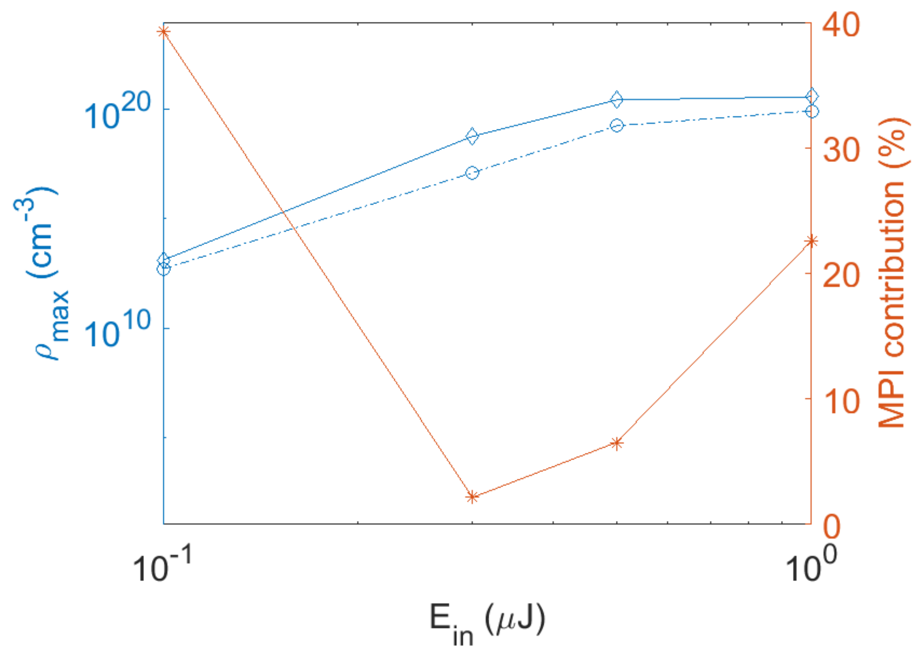


Figure 6.35: Simulation results of electron density vs input pulse energy in fused silica under femtosecond pulse irradiation. The maximum electron density is indicated by the left hand side y axis. The diamond solid line shows electron generation from multiphoton ionization and avalanche ionization. The circle dashed line shows electron generation from multiphoton ionization only. The percentage of electron contribution from multiphoton ionization is indicated by the right hand side y axis, and plotted as starred solid line in the graph.

## 6.4 Conclusions

In this chapter, we numerically studied ultrashort pulse behaviors and plasma dynamics in two common yet important materials (borosilicate glass and fused silica) at a pulse duration of 10 ps. We also investigated how shorter pulses, particularly a 500 fs pulse, interact with the bulk of fused silica.

The pulse behavior is highly energy dependent and material dependent. The electron dynamics, specifically the peak of the electron density follows the peak of the pulse in our simulation. We found that electron density level of $\rho = 10^{-20}\,\mathrm{cm}^{-3}$ matches the shape and size of the modification track in our experiments very well.

In the 500 fs case, the electron life time of a few picoseconds is much longer than the pulse duration indicating the complete decoupling of energy deposition and energy relaxation compared with the picosecond pulse. However, in the case of shorter pulse duration, the peak power of the pulse is much higher which drives more pronounced nonlinear effects that in return distort the pulse in space and time while propagating inside the material. The unwanted nonlinear effects will prevent effective energy deposition in the bulk or to the back side of the material[52, 53]. Thus, it is critical to understand the pulse behavior and electron dynamics to precisely control energy deposition in applications such as ultrashort laser welding, drilling, and cutting.

# CHAPTER 7

# Applications of ultrashort lasers

In this chapter, we will briefly talk about ultrashort pulsed laser applications in laser welding, waveguide writing, and glass cutting, among a variety of exciting applications that would be hard to cover exhaustively in this thesis.

## 7.1 Laser welding

Welding is of particular interest in modern assembly of sensors, microelectronics, and microfluidics devices. Various methods including adhesive bonding, fusion bonding, soldering and frit have been used in joining similar or dissimilar materials. These processes require either additional filling material or high temperature in the joining process. Joining with additional material either has out gassing concerns in the device or long term reliability issues. Joining with high temperature bonding on the other hand puts stringent requirements on the device itself that going through the baking process.

Ultrashort laser welding becomes very interesting as a contactless and localized heating method in joining both similar and dissimilar materials. For example, Watanabe et al. used a femtosecond laser to join dissimilar materials such as borosil-

icate glass and fused silica. A bonding strength of 15.3 MPa was achieved[54]. However, the requirement for optical contact and high pressure press in the laser welding process makes the welding a delicate process. Later on, Chen et al. demonstrated laser welding of glass with a large gap of around 10 µm by rapid scan of a loosely focused picosecond laser pulse [23]. With less requirement on the contact surface and no external force, this technique may open up more practical applications.

In order for laser welding to work, the materials that are joined together typically need to be transparent at the laser wavelength for the laser pulse to deliver energy to the interface and excite nonlinear absorption and material melting. Ceramics are of great interest in the electronics packaging industry due to their chemical and thermal resistance while still RF signal accessible. However, bonding ceramics is very challenging using convectional method, which typically involves high temperature. Very recently, Penilla et al, demonstrated bonding transparent ceramics using both femtosecond and picosecond laser pulses. Bonding shear strength of 40 Mpa and 10 Mpa have been achieved using picosecond laser pulse and femtosecond laser pulse, respectively[5]. Applications that require biocompatible, chemical and thermal resistant ceramic packaging with RF accessibility become possible.

## 7.2 Waveguide writting

Directly writing waveguides using an ultrashort laser is another important application where a laser can etch an optical interconnect in glass enabling optical lab on a chip. The nature of confined modification around the focal volume gives ultrashort laser the flexibility to perform even 3D waveguide. Typically, pulse energy to alter index is as low as nanojoules.

Tuning pulse energy, repetition rate, scanning speed and the focusing geometry, waveguides fabricated by ultrashort lasers can achieve transmission loss of 0.1 dB/mm[55, 56, 57, 58] and fiber spatial profiles close to those in fused silica [59].

## 7.3 Glass cutting

Another important application of ultrashort lasers is glass cutting. Conventional glass cutting is achieved through a scribe and break process. A diamond wheel is used in the process to introduce a surface crack and then a mechanical breaking process that physically punches the glass to propagate the initial surface cracks to separate the glass follows. Due to the nature of the process, only straight cuts can be generated. In order to make round corners or other shapes, follow up grinding steps need to be introduced. In addition, when the glass becomes thinner and thinner this process can be problematic.

Non-contact laser processing thus becomes very attractive through either introducing surface damage on the glass similar to the scribe process or introducing internal modifications that can propagate across the entire thickness. The introduction of Bessel beams for material processing enables glass cutting at a scalable level in high volume production[60, 61]. Instead of doing multiple z scans, Bessel beams have the ability to generate uniform elongated modification across the entire glass cross section[62] in one shot, which significantly shortened the process time. With a burst of pulses, micro cracks in materials like glass, chemical strengthen glass, and sapphire can be easily generated creating a preferential separation line[8]. Either mechanical or thermal processes can be used afterwards to separate the pieces. Laser glass cutting is not limited to straight cutting, which enables much more freedom to generate shapes like curve, circle, and spine line using a laser only process[63].

# CHAPTER 8

## Conclusions and outlook

In conclusion, we presented common phenomena in ultrashort pulse interaction with transparent materials. We demonstrated the generation of modification tracks in the bulk of borosilicate glass, fused silica and sapphire by a single shot of IR picosecond laser pulse. Specifically, we generated extended modification tracks with aspect ratio of 1:10 under our focusing geometry. The positions of the modification track shift away from the geometric focus towards the incoming laser beam driven by the plasma expansions and nonlinear effects such as self-focusing. The shape of the modification track shows distinct features at different energy levels. We observed smooth modification channels at low input pulse energy levels, while beaded hollow structures were found at higher input pulse energy levels in borosilicate glass. The morphology of ultrashort pulse modified regions in each material are very different.

To understand the initial electron generation, we modeled the pulse propagation and electron generation in borosilicate glass and fused silica numerically. Our simulation results show the size and shape of the inner dark modification track in the experiments match very well with electron density of $\rho_{max} = 10^{20}\,\mathrm{cm}^{-3}$ in our simulation. The dynamics of electron generation at different energy levels have been

investigated. We found multiphoton ionization is the major channel for electron generation at low pulse energy level. The role of multiphoton ionization becomes smaller and the role of avalanche ionization becomes bigger as we increase the pulse energy. The percentage of electron contribution from avalanche ionization reaches a maximum of 98% at pulse energy of 1 µJ in our simulation for borosilicate glass. Further increasing the pulse energy to above 1 µJ leads to a bigger role of the multiphoton ionization but the avalanche ionization still remains a significant contributor. For fused silica, avalanche ionization becomes dominant at pulse energy of 1 µJ and above.

We also numerically investigated the pulse behavior and electron dynamics for a femtosecond pulse interacting with fused silica. In the femtosecond pulse case, nonlinear effects become much more pronounced at lower pulse energies compared to the picosecond pulse and lead to much more severe beam distortion. The unwanted nonlinear effects that distort the beam will prevent effective energy deposition in the bulk or to the back side of the material. Thus, it is critical to understand the pulse behavior and electron dynamics to precisely control energy deposition. The pulse duration needs to be carefully selected to take advantage of the nonlinear effects.

Our study sheds light on the fundamental mechanism of electron generation that eventually leads to material modification in the bulk of borosilicate glass. The results might help to precisely control electron generation and pulse selection dur-

ing ultrashort pulse laser process of transparent materials in applications such as micro-welding, wave-guide writing, microfluidics and glass cutting. Further investigation on pulse behaviors and electron dynamics related to multiple pulses would be interesting.

# APPENDIX A

## Pulse propagation code

```
%Crank-Nicoson spectral extended scheme nonlinear
clear all;
close all;
%basic quantity
c = 299792458; %m/s
%Ein = 1e-6; %J input pulse energy
tp_FWHM = 10*10^-12; %pulse duration s 10ps
tp = tp_FWHM/sqrt(2*log(2));
lambda0 = 1064*10^-9; %wavelength
%labmda to um
[k0_lambda0,k1_lambda0,k2_lambda0] = k_fs(lambda0*1e6);
% index of refraction
n0 = n_fs(lambda0*1e6);
k0 = n0*2*pi/lambda0;
omega0 = k0*c/n0;
```

```
mu0=4.e-7*pi; % H/m vacuum permeability
epsilon0=1/c^2/mu0; % F/m vacuum permitivity
hbar=1.05457266e-34; %plank constant
rho_nt = 2.1e28; % neutral atom density (m^-3)
q_e=1.602176462e-19; m_e=9.10938356e-31;
tao_c = 2.33e-14; %electron collision time in glass
tao_r = 150*10e-15; %electron recombination time
rho_c = epsilon0*m_e*omega0^2/q_e^2;
%nonlinear index
n2 = 3.45e-20; %fused silica m^2/W
U = 9; %ev bandgap for fused silica
Ui = U*q_e;
K = floor(Ui/(hbar*omega0)); %multiphoton number
Kmpi = K + 1; %MPI photon number
for sigmak = [0.1 10]*10^-128
%multiphoton absorption
betak = Kmpi*hbar*omega0*sigmak*rho_nt;
%at omega0 inverse Bremsstrahlung coeff
sigma_omega0 = omega0*omega0*tao_c*(1 +
```

```
j*omega0*tao_c)/(n0*c*rho_c*(1 + omega0^2*tao_c^2));
invBremss = real(sigma_omega0);

%change avalanche rate to fit exp
for sigmaal = [3.25]*invBremss

Coeff_EtoI = 0.5*epsilon0*c*n0;
Coeff_kerr = epsilon0*2*n0*n2;
Coeff_mpi = epsilon0*c*n0*betak;
Coeff_plasma = epsilon0*c*n0*invBremss;

%beam parameters
D0 = 10*10^-3; %input beam width at lens m
ff = 100*10^-3; % lens focal length
d = 75*10^-6; % distance away from the linear focus
zR = k0*D0^2/2;
wf = 2.5e-6; %D0*ff/sqrt(ff^2 + zR^2); % beam waist
zf = k0*wf^2/2;
w0 = wf*sqrt(1 + d^2/zf^2); %initial beam width
```

```
f = d + zf^2/d; %initial curvature
% planar geometry v = 0, cylindrical geometry v = 1;
v = 1; % not used here
%r grids
rmax = 10*w0; %radial box size
Nr = 2^10; %grid points
dr = rmax/(Nr+1);
jj = 0:1:Nr+1; Njj = length(jj);
r = dr*jj;

%t grids
T = 10*tp;% time box size;
Nt = 2^10; %grid points
dt = T/Nt;
t = dt*((0:Nt-1)-Nt/2);

%omega grids
Nomega = Nt;
domega = 2*pi/(Nomega*dt);
```

```
omegal = zeros(1,Nomega);
for l = 0:Nomega/2-1
omegal(l+1) = omega0 + l*domega;
end
for l = Nomega/2:Nomega-1
omegal(l+1) = omega0 - pi/dt + l*domega;
end
% z distance, step
zmax = 150e-6; %propagation distance
Nz = 600; %total steps
dz = zmax/Nz;
z = dz*(0:Nz);
[rr,tt] = meshgrid(r,t);

% Kl Dl, dl, deltal, pl, ul
delta = dz/(4*k0*dr^2);
vg = 1/k1_lambda0;% m/s
kappa_omega = k0_lambda0 + (omegal - omega0)/vg;
lambdal = 2*pi*c./omegal; % m
```

```
Kl = k0*ones(1,Nomega);
%Kl = k0 + (omegal - omega0)/vg;
%Kl = n_fs(lambdal*1e6).*(omegal)/c;
Dl = 0.5*k2_lambda0*(omegal - omega0).^2;
%Dl = Kl - kappa_omega;
dl = dz*Dl/2; jdl = 1j*dl;
deltal = delta*k0./Kl; jdeltal = 1j*deltal;
pl = 1j*dz*omegal.^2./(2*Kl*epsilon0*c^2);
pl = transpose(pl);
plj = repmat(pl,1,length(r));
ul = -dz*omegal./(2*Kl*epsilon0*c^2);
ul  =transpose(ul);
ulj = repmat(ul,1,length(r));


% defenition of initial field
% intial beam definition
for Ein = [1.5 3]*10^-6 %input pulse energy
Pin = Ein/tp/sqrt(pi/2);
%E0 = sqrt(2*Pin/pi/w0^2);
```

```
I0 = 2*Pin/pi/w0^2;
E0 = sqrt(I0/Coeff_EtoI);
C = 0; %chirp
Einitial = E0*exp(-rr.^2/w0^2 - 1j*k0*rr.^2/(2*f)
- (1 + 1j*C)*tt.^2/tp^2);
Intensity0 = Coeff_EtoI*abs(Einitial(:,:).^2);
En0 = Einitial; %previous step
En1 = Einitial; %current step
Ew = fft(Einitial,[],1);

%propagation
M = 5; %every M steps perform expensive diagnostics
Kmax = Nz/M;
El_n2 = []; En2 = []; %next step
Etot = [transpose(En1)];
tpulse = zeros(1,floor(length(z)/M));
radius = zeros(1,floor(length(z)/M));
rhomax = zeros(1,floor(length(z)/M));
Intensity_on_axis_max = zeros(1,floor(length(z)/M));
```

```
wpi_z   = zeros(1,floor(length(z)/M));
r_rho  = zeros(1,floor(length(z)/M));
r_rho1 = zeros(1,floor(length(z)/M));
r_rho2 = zeros(1,floor(length(z)/M));


rho_onaxis = [];
pulse_t = [];
pulse_r = [];
for kk = 1: Kmax
    for mm = 1:M
        tic
        nn = (kk-1)*M + mm; %step number
        %nonlinear part
        %electron density
        rho = 0; % inital condition evey step
        for ti = 1:Nt-1
            I = Coeff_EtoI*abs(En1(ti,:)).^2;
            I1 = Coeff_EtoI*abs(En1(ti+1,:)).^2;
            Ih = (I + I1)/2;
```

```
    Ik = I.^Kmpi;
    Ik1 = I1.^Kmpi;
    Ikh = (Ik + Ik1)/2;
    rho = edensity(dt,rho_nt,rho,Ik,Ikh,Ik1,
    sigmak,sigmaal,I,Ih,I1,Ui,tao_r);
    rho_rt(ti,:) = transpose(rho);

end
ti = Nt;
I = Coeff_EtoI*abs(En1(ti,:)).^2;
I1 = 0;
Ih = (I + I1)/2;
Ik = I.^Kmpi;
Ik1 = I1.^Kmpi;
Ikh = (Ik + Ik1)/2;
rho = edensity(dt,rho_nt,rho,Ik,Ikh,Ik1,
sigmak,sigmaal,I,Ih,I1,Ui,tao_r);
rho_rt(ti,:) = transpose(rho);
```

```
%P and J term
Intensity1 = Coeff_EtoI*abs(En1).^2;
Wpi = sigmak*rho_nt*Intensity1.^Kmpi;
P_n1 = Coeff_kerr*Intensity1.*En1;% kerr term
J_PI = Coeff_mpi*Intensity1.^(Kmpi-1).*En1;
%MPA term, plasma absorption and defocusing
J_plasma = Coeff_plasma*(1 + 1j*omega0*tao_c)*rho_rt.*En1;
J_n1 = J_PI + J_plasma;


El_n1 = zeros(Nt,length(r));
Jl_n1 = zeros(Nt,length(r));
Pl_n1 = zeros(Nt,length(r));


for ii = 1:length(r)
El_n1(:,ii) = fft(squeeze(En1(:,ii)));
Pl_n1(:,ii) = fft(squeeze(P_n1(:,ii)));
Jl_n1(:,ii) = fft(squeeze(J_n1(:,ii)));
end
```

```
%calculate nolinear term Nl_n-1 and NL_n-2 term
Nl_n1 = plj.*Pl_n1 + ulj.*Jl_n1; %freq domain
if nn ==1
Nl_n0 = Nl_n1; % Nl_n0 is the step before Nl_n1
end

%loop on frequency
for l = 1:Nomega
    %calculate Lplusl Lminusl
    [Lplus, Lminus] = Lmatrix(Njj,jj,v,jdl(l),jdeltal(l));
    El_nl_l = transpose(squeeze(El_n1(l,:)));
    Nl_n1_l = transpose(squeeze(Nl_n1(l,:)));
    Nl_n0_l = transpose(squeeze(Nl_n0(l,:)));
    V1 = Lplus*El_nl_l;
    S1 = V1 + (3*Nl_n1_l - Nl_n0_l)/2;
    El_n2_l = Lminus\S1;
    El_n2(l,:) = transpose(El_n2_l);
end
Nl_n0 = Nl_n1;
```

```
        %FT back to time domain
        En2 = zeros(Nt,length(r));
        for ii = 1:length(r)
        En2(:,ii) = ifft(squeeze(El_n2(:,ii)));
        end
        En0 = En1;
        En1 = En2;
        En2 = []; El_n2 = []; % clear next step E
        toc
    end
    %every M step exam conditions
    zz(kk) = z(nn);
    Intensity = Coeff_EtoI*abs(En1(:,:).^2);
    [maxInt indexInt] = max(Intensity(:));
    [indxt indxr]=ind2sub(size(Intensity),indexInt);
    %1/e2
    radius(kk) = dr*sum(Intensity(indxt,:) > maxInt/exp(2));
    tpulse(kk) = dt*sum(Intensity(:,indxr) > maxInt/exp(2));
```

```
[maxrho indexrho] = max(rho_rt(:));
[indxt_rho indxr_rho]=ind2sub(size(rho_rt),indexrho);
rhomax(kk)= maxrho;
%find the elctron density at 10^27 1/m^3
position = find(rho_rt(indxt_rho,:) > 10^27, 1, 'last' );
if position
    r_rho(kk) = dr*position;
else
    r_rho(kk) = 0;
end
% find the elctron density at 10^26 1/m^3
position1 = find(rho_rt(indxt_rho,:) > 10^26, 1, 'last' );
if position1
    r_rho1(kk) = dr*position1;
else
    r_rho1(kk) = 0;
end
% find the elctron density at 10^25 1/m^3
position2 = find(rho_rt(indxt_rho,:) > 10^25, 1, 'last' );
```

```
        if position2
            r_rho2(kk) = dr*position2;
        else
            r_rho2(kk) = 0;
        end
        Intensity_on_axis_max(kk) = max(Intensity(:,1));
        wpi_z(kk) = max(max(Wpi));
        %onaxis rho
        rho_onaxis = [rho_onaxis rho_rt(:,1)];
        %onaxis pulse shape time domain
        pulse_t = [pulse_t Intensity(:,1)];
        %peak of Intensity shape space domain
        pulse_r = [pulse_r Intensity(indxt,:)'];
    end
    pulse_r2 = [flip(pulse_r,1);pulse_r]; % mirror pulse

    [maxrho indexrho] = max(rho_onaxis(:));
    [indxt indxz]=ind2sub(size(rho_onaxis),indexrho);
    rhomaxvst = rho_onaxis(:,indxz);
```

```
figure(1);
plot(zz,r_rho);
xlabel('z propagation (m)');
ylabel('radius at edensity 10^(27) m^(-3) ');
title('electron density contour vs z');
hold on;
figure(2);
plot(zz,radius);
xlabel('z propagation (m)');
ylabel('radius @1/e2 (m)');
title('radius vs z');
hold on;
figure(3);
plot(zz,tpulse);
xlabel('z propagation (m)');
ylabel('pulse duration (s)');
title('pulse duration vs z');
hold on;
```

```
figure(4);
semilogy(zz,rhomax*10^-6);
xlabel('z propagation (m)');
ylabel('max rho (cm^-3)');
title('max rho vs z');
hold on; %cm-3
figure(5);
semilogy(zz,Intensity_on_axis_max*10^-4);
xlabel('z propagation (m)');
ylabel('on axis Intensity (W/cm2)');
title('on axis Intensity vs z');
hold on; %cm-2
figure(6);
semilogy(zz,wpi_z);
xlabel('z propagation (m)');
ylabel('WPI rate');
title('WPI rate vs z');
hold on;
```

```
figure(7);
plot(t,rhomaxvst);
xlabel('time (s)');
ylabel('rho (m^(-3))');
title('max on axis electron density');
hold on;
filename = strcat('Ein',num2str(Ein),'_sigmak',
num2str(sigmak),'_al',num2str(sigmaal),'.mat');
save(filename,'Ein','sigmak','sigmaal','r','t',
'zz','Intensity0','radius','tpulse','rhomax',
'rhomaxvst','Intensity_on_axis_max','wpi_z',
'r_rho','r_rho1','r_rho2','rho_onaxis',
'pulse_t','pulse_r2');

filename2 = strcat('_sigmak',num2str(sigmak),
'_al',num2str(sigmaal));
saveas(figure(1),['edensity' filename2 '.bmp']);
saveas(figure(2),['radius' filename2 '.bmp']);
saveas(figure(3),['pulseduration' filename2 '.bmp']);
```

```
saveas(figure(4),['maxrhovsz' filename2 '.bmp']);
saveas(figure(5),['Intensityonaxis' filename2 '.bmp']);
saveas(figure(6),['MPIrate' filename2 '.bmp']);
saveas(figure(7),['maxrhovstime' filename2 '.bmp']);
end
end
end
end
function n = n_fs(x)
% lambda (i.e. x) in micron
        n = sqrt(1 + 0.6961663.*x.^2./(x.^2-0.0684043^2) +
        0.4079426.*x.^2./(x.^2-0.1162414^2) +
        0.8974794.*x.^2./(x.^2-9.896161^2));


end
%dispersion relation for fused silica
function [k0,k1,k2] = k_fs(x)
% lambda (i.e. x) in micron
        n = sqrt(1 + 0.6961663.*x.^2./(x.^2-0.0684043^2) +
```

```
0.4079426.*x.^2./(x.^2-0.1162414^2) +
0.8974794.*x.^2./(x.^2-9.896161^2));

dndl=(-((1.79496.*x.^3)./(-97.934+x.^2).^2)+
(1.79496.*x)./(-97.934+x.^2)-(0.815885.*x.^3)./
(-0.0135121+x.^2).^2+(0.815885.*x)./(-0.0135121+
x.^2)-(1.39233.*x.^3)./(-0.00467915+x.^2).^2+
(1.39233.*x)./(-0.00467915+x.^2))./(2.*sqrt(1+
(0.897479.*x.^2)./(-97.934+x.^2)+(0.407943.*x.^2)./
(-0.0135121+x.^2)+(0.696166.*x.^2)./(-0.00467915+
x.^2))); %micron^{-1}

c0=299792458; %m/s
k0=2.*pi.*n./x.*1e6; %m
k1=n./c0-x./c0.*dndl; %s/m

d2ndl2=-(-((1.79496.*x.^3)./(-97.934+x.^2).^2)+
(1.79496.*x)./(-97.934+x.^2)-(0.815885.*x.^3)./
(-0.0135121+x.^2).^2+(0.815885.*x)./(-0.0135121+
```

```
x.^2)-(1.39233.*x.^3)./(-0.00467915+x.^2).^2+
(1.39233.*x)./(-0.00467915+x.^2)).^2./(4.*(1+
(0.897479.*x.^2)./(-97.934+x.^2)+(0.407943.*x.^2)./
(-0.0135121+x.^2)+(0.696166.*x.^2)./(-0.00467915+
x.^2)).^(3/2))+((7.17984.*x.^4)./(-97.934+x.^2).^3-
(8.97479.*x.^2)./(-97.934+x.^2).^2+1.79496./(
-97.934+x.^2)+(3.26354.*x.^4)./(-0.0135121+x.^2).^3
-(4.07943.*x.^2)./(-0.0135121+x.^2).^2+0.815885./(
-0.0135121+x.^2)+(5.56933.*x.^4)./(-0.00467915+
x.^2).^3-(6.96166.*x.^2)./(-0.00467915+x.^2).^2+
1.39233./(-0.00467915+x.^2))./(2.*sqrt(1+
(0.897479.*x.^2)./(-97.934+x.^2)+(0.407943.*x.^2)./
(-0.0135121+x.^2)+(0.696166.*x.^2)./(-0.00467915+x.
^2)));

k2=x.*1e-6./c0.*x.^2./(2*pi*c0).*d2ndl2; %s^2/m

end
function [Lplus, Lminus]=Lmatrix(Njj,jj,v,jdl_l,jdeltal)
```

```
%main matrix

Lplus_diag(1:Njj) = (1 + jdl_l - 2*jdeltal);
Lminus_diag(1:Njj) = (1 - jdl_l + 2*jdeltal);

diagup = jdeltal*(1 + 0.5*v./jj);
diagup(1) =1;
diaglow = jdeltal*(1 - 0.5*v./jj);
diaglow(1)=1;

Lplus = sparse(1:Njj,1:Njj,Lplus_diag,Njj,Njj)
+ sparse(1:Njj-1,2:Njj,diagup(1:Njj-1),Njj,Njj)
+ sparse(2:Njj,1:Njj-1,diaglow(2:Njj),Njj,Njj);

Lminus = sparse(1:Njj,1:Njj,Lminus_diag,Njj,Njj)
+sparse(1:Njj-1,2:Njj,-diagup(1:Njj-1),Njj,Njj)
+sparse(2:Njj,1:Njj-1,-diaglow(2:Njj),Njj,Njj;

%bondary conditions
```

```
        %first order accurate
        d0plus = 0; d1plus = 0;
        %second order accurate
        %d0plus = 1 - 4*j*delta;
        d1plus = 4*j*delta;
        Lplus(1,1)=d0plus; Lplus(1,2)=d1plus;
        Lplus(Njj,Njj)=0; Lplus(Njj,Njj-1)=0;

        %first order accurate
        d0minus = 1; d1minus = -v;
        %second order accurate
        %d0minus = 1 + 4*j*delta;
        d1minus = -4*j*delta;

        Lminus(1,1)=d0minus; Lminus(1,2)=d1minus;
        Lminus(Njj,Njj)=1; Lminus(Njj,Njj-1)=0;

end
function drhodt = rate_equation(rho_nt,rho,Ik,sigmak,
```

```
sigmabrem,I,Ui,tao_r)
drhodt = (sigmak*Ik*rho_nt + sigmabrem*I.*rho/Ui).*(1
- rho/rho_nt) - rho/tao_r;
end
function rho_new = edensity(dt,rho_nt,rho_old,Ik,Ikh,Ik1,sigmak,
sigmabrem,I,Ih,I1,Ui,tao_r)
k1 = dt*rate_equation(rho_nt,rho_old,Ik,sigmak,
sigmabrem,I,Ui,tao_r);
rho2 = rho_old + k1/2;
k2 = dt*rate_equation(rho_nt,rho2,Ikh,sigmak,
sigmabrem,Ih,Ui,tao_r);
rho3 = rho_old + k2/2;
k3 = dt*rate_equation(rho_nt,rho3,Ikh,sigmak,
sigmabrem,Ih,Ui,tao_r);
rho4 = rho_old + k3;
k4 = dt*rate_equation(rho_nt,rho4,Ik1,sigmak,
sigmabrem,I1,Ui,tao_r);
rho_new = rho_old + (k1 + 2*k2 + 2*k3 + k4)/6;
end
```

# APPENDIX B

## Pulse intensity lookup table

| Pulse energy(µJ) | Fluence(J/cm$^2$) | Intensity (W/cm$^2$) |
|---|---|---|
| 1 | 5.10 | $5.1 \times 10^{11}$ |
| 1.5 | 7.64 | $7.64 \times 10^{11}$ |
| 2 | 10.19 | $1.02 \times 10^{12}$ |
| 2.5 | 12.74 | $1.27 \times 10^{12}$ |
| 3 | 15.29 | $1.53 \times 10^{12}$ |
| 5 | 25.48 | $2.55 \times 10^{12}$ |

Table B.1: Intensity lookup table for pulse duration 10 ps.

| Pulse energy(µJ) | Fluence(J/cm$^2$) | Intensity (W/cm$^2$) |
|---|---|---|
| 1 | 5.10 | $1.02 \times 10^{13}$ |
| 2 | 10.19 | $2.04 \times 10^{13}$ |
| 3 | 15.29 | $3.06 \times 10^{13}$ |

Table B.2: Intensity lookup table for pulse duration 500 fs.

# REFERENCES

[1] U. Keller, D. A. B. Miller, G. D. Boyd, T. H. Chiu, J. F. Ferguson, and M. T. Asom. Solid-state low-loss intracavity saturable absorber for nd:ylf lasers: an antiresonant semiconductor fabry–perot saturable absorber. *Opt. Lett.*, 17(7): 505–507, Apr 1992.

[2] D. E. Spence, P. N. Kean, and W. Sibbett. 60-fsec pulse generation from a self-mode-locked ti:sapphire laser. *Opt. Lett.*, 16(1):42–44, Jan 1991.

[3] I. D. Jung, F. X. Kärtner, N. Matuschek, D. H. Sutter, F. Morier-Genoud, G. Zhang, U. Keller, V. Scheuer, M. Tilsch, and T. Tschudi. Self-starting 6.5-fs pulses from a ti:sapphire laser. *Opt. Lett.*, 22(13):1009–1011, Jul 1997.

[4] Donna Strickland and Gerard Mourou. Compression of amplified chirped optical pulses. *Optics Communications*, 55(6):447–449, 1985. ISSN 0030-4018.

[5] E. H. Penilla, L. F. Devia-Cruz, A. T. Wieg, P. Martinez-Torres, N. Cuando-Espitia, P. Sellappan, Y. Kodera, G. Aguilar, and J. E. Garay. Ultrafast laser welding of ceramics. *Science*, 365(6455):803–808, 2019.

[6] Luke B. Fletcher, Jon J. Witcher, Neil Troy, Signo T. Reis, Richard K. Brow, and Denise M. Krol. Direct femtosecond laser waveguide writing inside zinc phosphate glass. *Opt. Express*, 19(9):7929–7936, Apr 2011.

[7] Roberto Osellame, Stefano Taccheo, Marco Marangoni, Roberta Ramponi, Paolo Laporta, Dario Polli, Sandro De Silvestri, and Giulio Cerullo. Femtosecond writing of active optical waveguides with astigmatically shaped beams. *J. Opt. Soc. Am. B*, 20(7):1559–1567, Jul 2003.

[8] K. Mishchik, R. Beuton, O. Dematteo Caulier, S. Skupin, B. Chimier, G. Duchateau, B. Chassagne, R. Kling, C. Hönninger, E. Mottay, and J. Lopez. Improved laser glass cutting by spatio-temporal control of energy deposition using bursts of femtosecond pulses. *Opt. Express*, 25(26):33271–33282, Dec 2017.

[9] L. Sudrie, A. Couairon, M. Franco, B. Lamouroux, B. Prade, S. Tzortzakis, and A. Mysyrowicz. Femtosecond laser-induced damage and filamentary propagation in fused silica. *Phys. Rev. Lett.*, 89:186601, Oct 2002.

[10] Eugene G. Gamaly, Saulius Juodkazis, Koichi Nishimura, Hiroaki Misawa, Barry Luther-Davies, Ludovic Hallo, Philippe Nicolai, and Vladimir T. Tikhonchuk. Laser-matter interaction in the bulk of a transparent solid: Confined microexplosion and void formation. *Phys. Rev. B*, 73:214101, Jun 2006.

[11] Mingying Sun, Urs Eppelt, Wolfgang Schulz, and Jianqiang Zhu. Role of thermal ionization in internal modification of bulk borosilicate glass with picosecond laser pulses at high repetition rates. *Opt. Mater. Express*, 3(10):1716–1726, Oct 2013.

[12] E. N. Glezer and E. Mazur. Ultrafast-laser driven micro-explosions in transparent materials. *Appl. Phys. Lett.*, 71(7):882–884, 1997.

[13] Arturas Vailionis, Eugene G. Gamaly, Vygantas Mizeikis, Wenge Yang, Andrei V. Rode, and Saulius Juodkazis. Evidence of superdense aluminium synthesized by ultrafast microexplosion. *Nat. Comm.*, 2:445, 08 2011.

[14] Lena Bressel, Dominique de Ligny, Eugene G. Gamaly, Andrei V. Rode, and Saulius Juodkazis. Observation of o2 inside voids formed in geo2 glass by tightly-focused fs-laser pulses. *Opt. Mater. Express*, 1(6):1150–1158, Oct 2011.

[15] Saulius Juodkazis, Hiroaki Misawa, Tomohiro Hashimoto, Eugene G. Gamaly, and Barry Luther-Davies. Laser-induced microexplosion confined in a bulk of silica: Formation of nanovoids. *Appl. Phys. Lett.*, 88(20):201909, 2006.

[16] Rafael R. Gattass and Eric Mazur. Femtosecond laser micromachining in transparent materials. *Nature*, 2:219–225, 2008.

[17] M. D. Perry, B. C. Stuart, P. S. Banks, M. D. Feit, V. Yanovsky, and A. M. Rubenchik. Ultrashort-pulse laser machining of dielectric materials. *Journal of Applied Physics*, 85(9):6803–6810, 1999.

[18] B. N. Chichkov, C. Momma, S.and von Alvensleben F. Nolte, and A. Tünnermann. Femtosecond, picosecond and nanosecond laser ablation of solids. *Applied Physics A*, 63:109–115, 1996.

[19] Masaaki Sakakura, Masahiro Shimizu, Yasuhiko Shimotsuma, Kiyotaka Miura, and Kazuyuki Hirao. Temperature distribution and modification mechanism inside glass with heat accumulation during 250khz irradiation of femtosecond laser pulses. *Applied Physics Letters*, 93(23):231112, 2008.

[20] Shane M. Eaton, Haibin Zhang, Mi Li Ng, Jianzhao Li, Wei-Jen Chen, Stephen Ho, and Peter R. Herman. Transition from thermal diffusion to heat accumulation in high repetition rate femtosecond laser writing of buried optical waveguides. *Opt. Express*, 16(13):9443–9458, Jun 2008.

[21] Isamu Miyamoto, Kristian Cvecek, and Michael Schmidt. Evaluation of nonlinear absorptivity in internal modification of bulk glass by ultrashort laser pulses. *Opt. Express*, 19(11):10714–10727, May 2011.

[22] Isamu Miyamoto, Kristian Cvecek, Yasuhiro Okamoto, Michael Schmidt, and Henry Helvajian. Characteristics of laser absorption and welding in foturan glass by ultrashort laser pulses. *Opt. Express*, 19(23):22961–22973, Nov 2011.

[23] Hang Chen, Leimin Deng, Jun Duan, and Xiaoyan Zeng. Picosecond laser welding of glasses with a large gap by a rapid oscillating scan. *Opt. Lett.*, 44 (10):2570–2573, May 2019.

[24] Jianyong Chen, Richard M. Carter, Robert R. Thomson, and Duncan P. Hand. Avoiding the requirement for pre-existing optical contact during picosecond laser glass-to-glass welding. *Opt. Express*, 23(14):18645–18657, Jul 2015.

[25] Kristian Cvecek, Rainer Odato, Sarah Dehmel, Isamu Miyamoto, and Michael Schmidt. Gap bridging in joining of glass using ultra short laser pulses. *Opt. Express*, 23(5):5681–5693, Mar 2015.

[26] Isamu Miyamoto, Kristian Cvecek, and Michael Schmidt. Crack-free conditions in welding of glass by ultrashort laser pulse. *Opt. Express*, 21(12):14291–14302, Jun 2013.

[27] T. H. MAIMAN. Stimulated optical radiation in ruby. *Nature*, 187:493–494, 1960.

[28] T. H. Maiman. Stimulated optical emission in fluorescent solids. i. theoretical considerations. *Phys. Rev.*, 123:1145–1150, Aug 1961.

[29] T. H. Maiman, R. H. Hoskins, I. J. D'Haenens, C. K. Asawa, and V. Evtuhov. Stimulated optical emission in fluorescent solids. ii. spectroscopy and stimulated emission in ruby. *Phys. Rev.*, 123:1151–1157, Aug 1961.

[30] Ursula Keller. Recent developments in compact ultrafast lasers. *Nature*, 424: 831–838, 2003.

[31] U. Keller, G. W. 'tHooft, W. H. Knox, and J. E. Cunningham. Femtosecond pulses from a continuously self-starting passively mode-locked ti:sapphire laser. *Opt. Lett.*, 16(13):1022–1024, Jul 1991.

[32] François Salin, Jeff Squier, and Michel Piché. Mode locking of ti:al2o3 lasers and self-focusing: a gaussian approximation. *Opt. Lett.*, 16(21):1674–1676, Nov 1991.

[33] Lumentum. Picoblade 2 picosecond micromachining laser. URL `https://resource.lumentum.com/s3fs-public/technical-library-items/picoblade2-ds-cl-ae.pdf`.

[34] Xuesheng Liu, Wenzeng Jia, Yiheng Song, Song Yang, Shu Liu, Youqiang Liu, Anru Yan, and Zhiyong Wang. High energy, high brightness picosecond master oscillator power amplifier with output power 65.5 w. *Opt. Express*, 28(6):8016–8026, Mar 2020.

[35] Nobel Prize. The nobel prize in physics 2018. URL `https://www.nobelprize.org/prizes/physics/2018/summary/`.

[36] M. Perry. Multilayer dielectric gratings: increasing the power of light. *Sci.Technol. Rev.*, pages 24–33, Sep 1995.

[37] John David Jackson. *Classical Electrodynamics*. Wiley; 3rd edition, 1998.

[38] Femtosecond filamentation in transparent media. *Physics Reports*, 441(2):47–189, 2007.

[39] Robert W. Boyd. *Nonlinear Optics*. Elsevier; 3rd edition, 2008.

[40] J.H. Marburger. Self-focusing: Theory. *Progress in Quantum Electronics*, 4: 35–110, 1975. ISSN 0079-6727.

[41] L. V. Keldysh. Ionization in the field of a strong electromagnetic wave. *Sov. Phys. JETP*, 20:1307, May 1965.

[42] Eli Yablonovitch and N. Bloembergen. Avalanche ionization and the limiting diameter of filaments induced by light pulses in transparent media. *Phys. Rev. Lett.*, 29:907–910, Oct 1972.

[43] B. C. Stuart, M. D. Feit, S. Herman, A. M. Rubenchik, B. W. Shore, and M. D. Perry. Nanosecond-to-femtosecond laser-induced breakdown in dielectrics. *Phys. Rev. B*, 53:1749–1761, Jan 1996.

[44] A. Couairon, E. Brambilla, T. Corti, D. Majus, O. de J. Ramírez-Góngora, and M. Kolesik. Practitioner's guide to laser pulse propagation models and simulation. *The European Physical Journal Special Topics*, 199:5–76, 2011.

[45] Weibo Cheng and Pavel Polynkin. Micromachining of borosilicate glass surfaces using femtosecond higher-order bessel beams. *J. Opt. Soc. Am. B*, 31(11):C48–C52, Nov 2014.

[46] S. Juodkazis, K. Nishimura, S. Tanaka, H. Misawa, E. G. Gamaly, B. Luther-Davies, L. Hallo, P. Nicolai, and V. T. Tikhonchuk. Laser-induced microexplosion confined in the bulk of a sapphire crystal: Evidence of multimegabar pressures. *Phys. Rev. Lett.*, 96:166101, Apr 2006.

[47] M. Mlejnek, E. M. Wright, and J. V. Moloney. Dynamic spatial replenishment of femtosecond pulses propagating in air. *Opt. Lett.*, 23(5):382–384, Mar 1998.

[48] M. Kolesik, E. M. Wright, and J. V. Moloney. Dynamic nonlinear x waves for femtosecond pulse propagation in water. *Phys. Rev. Lett.*, 92:253901, Jun 2004.

[49] P. Audebert, Ph. Daguzan, A. Dos Santos, J. C. Gauthier, J. P. Geindre, S. Guizard, G. Hamoniaux, K. Krastev, P. Martin, G. Petite, and A. Antonetti. Space-time observation of an electron gas in $sio_2$. *Phys. Rev. Lett.*, 73:1990–1993, Oct 1994.

[50] J. Crank and P. Nicolson. A practical method for numerical evaluation of solutions of partial differential equations of the heat-conduction type. *Mathematical Proceedings of the Cambridge Philosophical Society*, 43(1):50–67, 1947.

[51] S. Tzortzakis, L. Sudrie, M. Franco, B. Prade, A. Mysyrowicz, A. Couairon, and L. Bergé. Self-guided propagation of ultrashort ir laser pulses in fused silica. *Phys. Rev. Lett.*, 87:213902, Nov 2001.

[52] Weibo Cheng and Pavel Polynkin. Micromachining of borosilicate glass surfaces using femtosecond higher-order bessel beams. *J. Opt. Soc. Am. B*, 31(11):C48–C52, Nov 2014.

[53] Weibo Cheng, Xiao-Long Liu, and Pavel Polynkin. Simultaneously spatially and temporally focused femtosecond vortex beams for laser micromachining. *J. Opt. Soc. Am. B*, 35(10):B16–B19, Oct 2018.

[54] Wataru Watanabe, Satoshi Onda, Takayuki Tamaki, Kazuyoshi Itoh, and Junji Nishii. Space-selective laser joining of dissimilar transparent materials using femtosecond laser pulses. *Applied Physics Letters*, 89(2):021106, 2006.

[55] Catalin Florea and Kim A. Winick. Fabrication and characterization of photonicdevices directly written in glass usingfemtosecond laser pulses. *J. Lightwave Technol.*, 21(1):246, Jan 2003.

[56] R. Osellame, N. Chiodo, V. Maselli, A. Yin, M. Zavelani-Rossi, G. Cerullo, P. Laporta, L. Aiello, S. De Nicola, P. Ferraro, A. Finizio, and G. Pierattini. Optical properties of waveguides written by a 26 mhz stretched cavity ti:sapphire femtosecond oscillator. *Opt. Express*, 13(2):612–620, Jan 2005.

[57] Shane M. Eaton, Haibin Zhang, Peter R. Herman, Fumiyo Yoshino, Lawrence Shah, James Bovatsek, and Alan Y. Arai. Heat accumulation effects in femtosecond laser-written waveguides with variable repetition rate. *Opt. Express*, 13(12):4708–4716, Jun 2005.

[58] Haibin Zhang, Shane M. Eaton, and Peter R. Herman. Low-loss type ii waveguide writing in fused silica with single picosecond laser pulses. *Opt. Express*, 14(11):4826–4834, May 2006.

[59] Matthias Will, Stefan Nolte, Boris N. Chichkov, and Andreas Tünnermann. Optical properties of waveguides fabricated in fused silica by femtosecond laser pulses. *Appl. Opt.*, 41(21):4360–4364, Jul 2002.

[60] Juozas Dudutis, Paulius GeČys, and Gediminas RaČiukaitis. Non-ideal axicon-generated bessel beam application for intra-volume glass modification. *Opt. Express*, 24(25):28433–28443, Dec 2016.

[61] M. Duocastella and C.B. Arnold. Bessel and annular beams for materials processing. *Laser & Photonics Reviews*, 6(5):607–621, 2012.

[62] John Lopez, Konstantin Mishchik, Bruno Chassagne, Clémentine Javaux-Leger, Clemens Hönninger, Eric Mottay, and Rainer Kling. Glass cutting using ultrashort pulsed bessel beams. *International Congress on Applications of Lasers & Electro-Optics*, 2015(1):60–69, 2015.

[63] Corning. Corning laser technologies. URL `https://www.corning.com/media/worldwide/csm/documents/CLT_PISheet_3142014.pdf`.